OPTICAL DETECTION AND STRUCTURAL ANALYSIS OF DNA VIA DIRECT SURFACE-ENHANCED RAMAN SCATTERING

Patricia Gisbert Quilis

UNIVERSITAT ROVIRA I VIRGILI
OPTICAL DETECTION AND STRUCTURAL ANALYSIS OF DNA VIA DIRECT SURFACE-ENHANCED RAMAN SCATTERING
Patricia Gisbert Quilis

UNIVERSITAT
ROVIRA i VIRGILI

DOCTORAL THESIS Optical detection and structural analysis of DNA via direct surface-enhanced Raman scattering Patricia Gisbert Quilis 2018

UNIVERSITAT
ROVIRA i VIRGILI

OPTICAL DETECTION AND STRUCTURAL ANALYSIS OF DNA VIA DIRECT SURFACE-ENHANCED RAMAN SCATTERING

Patricia Gisbert Quilis

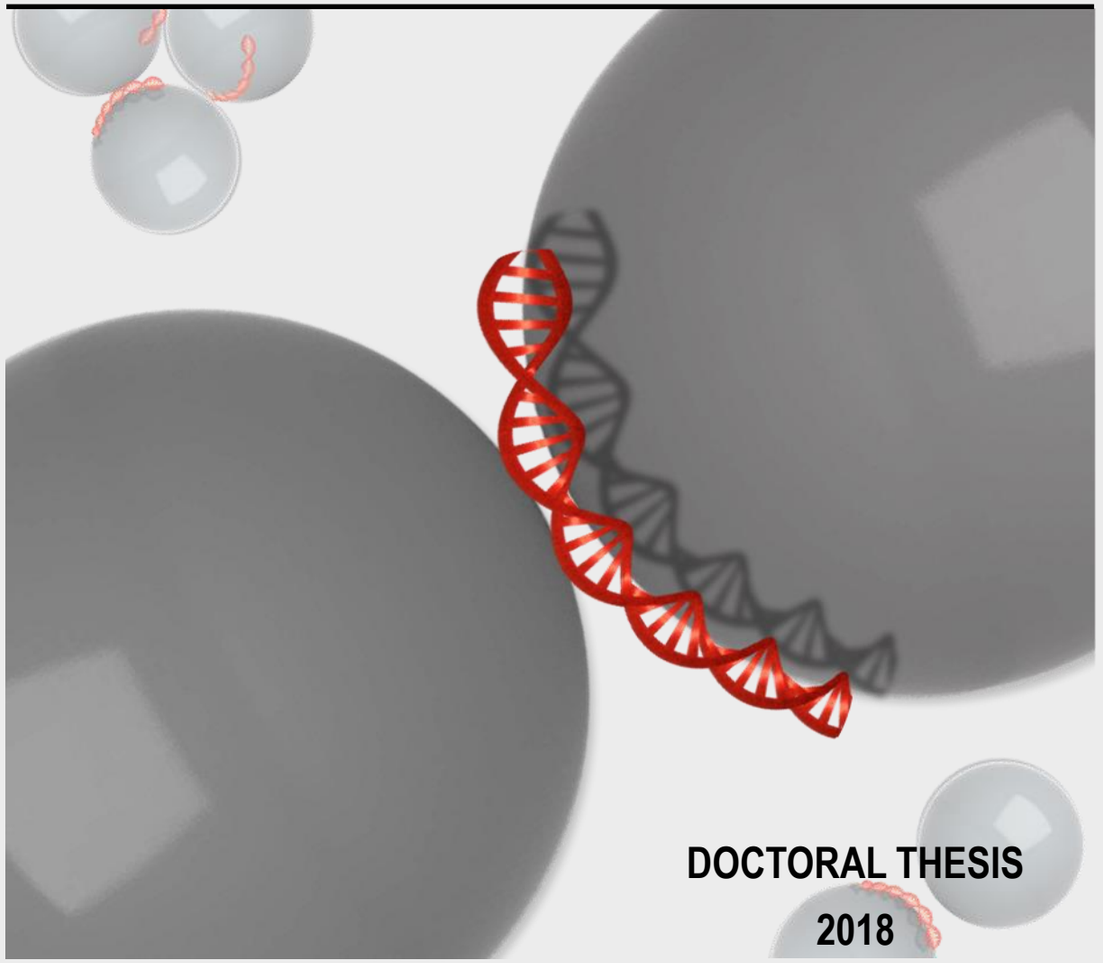

DOCTORAL THESIS
2018

UNIVERSITAT ROVIRA I VIRGILI
OPTICAL DETECTION AND STRUCTURAL ANALYSIS OF DNA VIA DIRECT SURFACE-ENHANCED RAMAN SCATTERING
Patricia Gisbert Quilis

UNIVERSITAT ROVIRA I VIRGILI
OPTICAL DETECTION AND STRUCTURAL ANALYSIS OF DNA VIA DIRECT SURFACE-ENHANCED RAMAN SCATTERING
Patricia Gisbert Quilis

Patricia Gisbert Quilis

OPTICAL DETECTION AND STRUCTURAL ANALYSIS OF DNA VIA DIRECT SURFACE-ENHANCED RAMAN SCATTERING

DOCTORAL THESIS

Industrial Doctorate Mention

Supervised by Prof. Ramón A. Álvarez Puebla

Dr. Luca Guerrini

FACULTY OF CHEMISTRY

DEPARTMENT OF PHYSICAL AND INORGANIC CHEMISTRY

Tarragona, 2018

UNIVERSITAT ROVIRA i VIRGILI

medcom advance

UNIVERSITAT ROVIRA I VIRGILI
OPTICAL DETECTION AND STRUCTURAL ANALYSIS OF DNA VIA DIRECT SURFACE-ENHANCED RAMAN SCATTERING
Patricia Gisbert Quilis

UNIVERSITAT ROVIRA I VIRGILI
OPTICAL DETECTION AND STRUCTURAL ANALYSIS OF DNA VIA DIRECT SURFACE-ENHANCED RAMAN SCATTERING
Patricia Gisbert Quilis

UNIVERSITAT ROVIRA I VIRGILI
OPTICAL DETECTION AND STRUCTURAL ANALYSIS OF DNA VIA DIRECT SURFACE-ENHANCED RAMAN SCATTERING
Patricia Gisbert Quilis

UNIVERSITAT ROVIRA i VIRGILI

Departament de Química Física i Inorgànica

Prof. Ramón A. Álvarez Puebla, ICREA Research Professor at Universitat Rovira i Virgili (URV) and Dr. Luca Guerrini, Ramón y Cajal Research Associate at URV,

CERTIFY

that the study entitled "OPTICAL DETECTION AND STRUCTURAL ANALYSIS OF DNA VIA DIRECT SURFACE-ENHANCED RAMAN SCATTERING" presented by Patricia Gisbert Quilis for the award of the degree of Doctor, has been carried out under our supervision at the Department of Physical and Inorganic Chemistry.

Tarragona, January 2018

Doctoral thesis supervisor

Prof. Ramón A. Álvarez Puebla

Doctoral thesis supervisor

Dr. Luca Guerrini

UNIVERSITAT ROVIRA I VIRGILI
OPTICAL DETECTION AND STRUCTURAL ANALYSIS OF DNA VIA DIRECT SURFACE-ENHANCED RAMAN SCATTERING
Patricia Gisbert Quilis

Aquesta tesi s'ha realitzat amb el suport de la Secretaria d'Universitats i Recerca del Departament d'Empresa i Coneixement de la Generalitat de Catalunya.

Generalitat de Catalunya
Departament d'Empresa i Coneixement
Secretaria d'Universitats i Recerca

UNIVERSITAT ROVIRA I VIRGILI
OPTICAL DETECTION AND STRUCTURAL ANALYSIS OF DNA VIA DIRECT SURFACE-ENHANCED RAMAN SCATTERING
Patricia Gisbert Quilis

"*Nothing in life is to be feared, it is only to be understood. Now is the time to understand more, so that we may fear less*"

Marie Curie

UNIVERSITAT ROVIRA I VIRGILI
OPTICAL DETECTION AND STRUCTURAL ANALYSIS OF DNA VIA DIRECT SURFACE-ENHANCED RAMAN SCATTERING
Patricia Gisbert Quilis

CONTENTS

LIST OF ABBREVIATIONS

A	Adenine
AgCit NPs	Negatively charged citrate capped nanoparticles
AgHX NPs	Negatively charged hydroxylamine silver nanoparticles
AgSp NPs	Positively charged spermine coated silver nanoparticles
C	Cytosine
CCD	Charge-coupled device
CE	Chemical
CG	Coarse-grained
CTAB	Cetyl trimethylammonium bromide
ctDNA	Genomic calf-thymus DNA
DLS	Dynamic light scattering
dsDNA	Double-stranded DNA
EF	Enhancement factor
EM	Electromagnetic
ERK	Extracellular signal-regulated kinase
FDTD	Finite difference time domain
G	Guanine
GAPs	GTPase activating proteins
GDP	Guanosine-5'-diphosphate
GEFs	Guanine nucleotide exchange factors
GTP	Guanosine-5'-triphosphate
HOMO	Highest occupied molecular orbital
H-Ras	Harvey retrovirus associated-DNA sequence
K-Ras	Kirsten retrovirus associated-DNA sequence
LSPR	Localized surface plasmon resonance
LUMO	Lowest occupied molecular orbital

LV	Latent variable
MAP	Mitogen-activated protein kinase cascade
MD	Molecular dynamics
MEK	MAPK/ERK kinase
NA	Nucleic acid
N-Ras	Neuroblastoma retrovirus associated-DNA sequence
nt	Nucleotide
PBS	Phosphate buffer saline
PCA	Principal component analysis
PCR	Polymerase chain reaction
PDB	Protein data bank
PEI	Polyethylenimine
PLL	Poly-L-Lysine
PLS-DA	Partial least square discriminant analysis
Raf1	Rapidly accelerated fibrosarcoma 1 kinase
RDBs	Ras-binding proteins
SERS	Surface-enhanced Raman scattering
SERRS	Surface-enhanced resonance Raman scattering
$SpCl_4$	Spermine tetrahydrochloride
SPR	Surface plasmon resonance
SSCP	Single strand conformational polymorphism
ssDNA	Single-stranded DNA
T	Thymine
TBE	Tris/Borate/EDTA
TEM	Transmission electron microscopy
TEMED	Tetramethylethylenediamine
tRNA	Transfer RNA
U	Uracil

UNIVERSITAT ROVIRA I VIRGILI
OPTICAL DETECTION AND STRUCTURAL ANALYSIS OF DNA VIA DIRECT SURFACE-ENHANCED RAMAN SCATTERING
Patricia Gisbert Quilis

UNIVERSITAT ROVIRA I VIRGILI
OPTICAL DETECTION AND STRUCTURAL ANALYSIS OF DNA VIA DIRECT SURFACE-ENHANCED RAMAN SCATTERING
Patricia Gisbert Quilis

THESIS SCOPE

Recognition of alterations in DNA sequences is of outmost importance for diagnosis and prognosis of genetic diseases. However, DNA is usually found at low concentrations and requires the use of extremly sensitive and accurate analytical techniques capable of detecting known and unknown modifications. Such sensitivity and specificity is not always fulfilled by traditional detection methods, which often involve pre-amplification steps, complicated procedures or the use of fluorescent reporters.

In recent years, surface-enhanced Raman scattering (SERS) spectroscopy has developed into a mature and reliable spectroscopic technique for the analysis and identification of nucleic acids. SERS combines the specificity and experimental versatility of Raman spectroscopy with an increased sensitivity, as a result of the unique optical signal amplification properties of plasmonic nanomaterials.

Despite the potential of SERS for ultrasensitive detection of analytes, even down to single molecule detection, its implementation to DNA analysis has been mainly restricted to indirect SERS strategies. These strategies mainly involve DNA hybridization events and the use of extrinsic Raman labels, to report the presence of the target DNA sequence. However, indirect approaches dismiss the structural information intrinsically contained in the Raman spectrum of DNA. On the other hand, while direct SERS approaches offer higher potential in terms of specificity as they can provide such vibrational information, they have traditionally experienced key issues associated with low sensitivity and/or limited reproducibility. In recent years, great efforts have been devoted to circumvent these limitations.

On this basis, the **general objective** of this dissertation is the application of **label-free direct surface-enhanced Raman scattering of DNA sequences** for genetic screening applications and structural analysis of DNA/nanoparticles conglomerates. To this end, a novel method based on the use positively charged spermine-coated silver nanoparticles (AgSp NPs) as plasmonic materials is exploited. Cationic AgSp NPs are used as efficient SERS substrates to

electrostatically entrap negatively-charged DNAs at the interparticle junctions, yielding highly SERS-active and long-term stable clusters in suspension. In this way, intense and highly reproducible SERS signal from DNA is obtained down to the nanogram regime.

The dissertation is organized according to the following **specific objectives**: **I)** synthesis, characterization and implementation of AgSp NPs to the direct SERS analysis of DNA; **II)** detection and conformational classification of point mutations in a relatively long sequence of the *K-Ras* gene; and **III)** direct structural analysis of native DNA/RNAs upon electrostatic interactions with AgSp NPs.

Accordingly, the dissertation will comprise four chapters:

Chapter 1 provides the basic theoretical background to understand diseases triggered by punctual alterations (mutations) in specific genes, such as the case of cancer. In addition, the advantages and limitations of conventional methods for detection of point mutations in DNA sequences is reviewed. In the second part of this chapter, the integration of SERS as a sensing tool for the exploration of nucleic acids is presented, as well as the theoretical basis to understand the technique.

In **Chapter 2**, the implementation of AgSp NPs as the sensing platform for SERS analysis of nucleic acids is discussed. Firstly, the plasmonic substrate is fully characterized by several techniques, such as UV-visible absorption, transmission electron microscopy, and dynamic light scattering. Subsequently, representative single and double stranded DNA sequences are selected as model analytes to assess the performance of AgSp NPs in the direct SERS study of nucleic acids and determine the corresponding optimal working conditions. This chapter also includes the vibrational assignment of the SERS spectral features of DNAs, based from previous literature reports.

Chapter 3 highlights the clinical potential of the direct SERS method for discrimination of DNA point mutations. In particular, point mutations in Ras oncogenes are routinely screened for diagnostics and treatment of tumors (especially in colorectal cancer). Therefore, the determination of this punctual mutations in a sensitive, fast and inexpensive manner is essential for diagnosis

and prognosis. Herein, direct SERS coupled with chemometrics is used as a tool for the study of the specific conformations that single-point mutations impose on a relatively large fragment of the *K-Ras* gene (141 nucleobases).

Finally, in **Chapter 4** the underlying mechanisms of interaction between DNA (as well as for RNA) with AgSp NPs in this direct SERS method are investigated in depth. Here, plasmon-based spectroscopies and theoretical simulations are combined to directly investigate the role of the cooperative binding of cationic nanoparticles with different surface charges on the structural integrity of a large variety of nucleic acids.

Chapter 1

Theoretical background

UNIVERSITAT ROVIRA I VIRGILI
OPTICAL DETECTION AND STRUCTURAL ANALYSIS OF DNA VIA DIRECT SURFACE-ENHANCED RAMAN SCATTERING
Patricia Gisbert Quilis

UNIVERSITAT ROVIRA I VIRGILI
OPTICAL DETECTION AND STRUCTURAL ANALYSIS OF DNA VIA DIRECT SURFACE-ENHANCED RAMAN SCATTERING
Patricia Gisbert Quilis

1.1. Preface

The deoxyribonucleic acid (DNA) is the most important custodian of life, archived in all living cells. Within the two major types of cells (eukaryotes – present in animals and plants – and prokaryotes – comprising bacteria –), the genetic information is orderly stored in strands of DNA, in the form of a double helix. In humans, nearly every cell of the body contains the same DNA. Most of this DNA is stored in the cell nucleus adopting the tangled form of chromatin, which condenses in the shape of chromosomes during the cell division, although a small portion is also found in individual mitochondria. As computers where the information is quantified in 1s and 0s, the hereditary information found in DNA consists of a readout-only chemical code, represented by 4 main letters of the alphabet: A (adenine), C (cytosine), G (guanine), and T (thymine). The order in which these bases are allocated in the DNA structure determines the foundation for the building and maintenance of any organism. Despite the tremendous importance of DNA, its structure – and consequently the underlying mechanisms of storage and transmission of genetic information – was not discovered until the 1950's, by James Watson, Francis Crick, and R. Franklin.[1,2] This discovery supposed a breakthrough in the field of genetics. Currently, scientists have reached to understand how DNA can be damaged and how genetic mutations may lead to harmful diseases, such as cancer.

Cancers have been tightly associated with genetic disorders, as a result of the disruption of the normal cell cycle during cell growth and proliferation. Worldwide, it is estimated that about 100 to 350 of every 100,000 people will die of cancer per year.[3] In humans, many genes (sections of DNA) strictly control and regulate this cellular process (from the development to the whole adult lifetime), in order to balance the stimuli signals of growth, growth-inhibiting, and self-destruction that cells are exposed to. Therefore, the understanding of the genetic roots involved in the process of cancer may help to develop new therapies and enable the improvement of conventional detection techniques for diagnosis and prognosis of the disease.

In this chapter, the basic concepts for understanding the genetic roots of cancer will be described from the macroscopic view of the cell cycle to the genetic

scale. As a main goal, we have intended to build a sensing strategy by means of surface-enhanced Raman scattering for the ultra-sensitive and selective detection of point mutations involved in cancer. In addition, the impact of the nanomaterials employed on the DNA structure has been extensively studied, which gives further insight of the physicochemical processes at the interface between nucleic acids and nanomaterials.

1.2. The structure of DNA and its biological relevance

The structure of DNA can be described in three different levels of complexity. The primary structure comprises the subunits that configure DNA, while the secondary structure encompasses a regular conformation made of these subunits. Finally, the tertiary structure of DNA can be understood as a more complex construction, taking into account steric constraints, folding and stacking interactions.

1.2.1 Primary structure of DNA

The primary structure of DNA is composed of repetitive subunits named nucleotides (**Figure 1.1 and 1.2**). Each nucleotide is made of a phosphate group, a sugar group (deoxyribose) and a nucleobase (A, C, T or G) – sometimes they are referred as just bases. The term nucleotide should not be confused with the term nucleoside, which refers to the entity formed by only the sugar and the base, without the presence of the phosphate group.

Nucleotides are attached together through phosphodiester covalent linkages between the sugar and the phosphate groups, forming what is known as the phosphate backbone of DNA. This backbone is hydrophilic since the hydroxyl groups in the pentose sugar can interact via hydrogen bonding with the water molecules in the surrounding environment.[4] The phosphate-sugar linkages have the same orientation and confer to the DNA chain, or strand, a specific directionality with distinctive 5’ and 3’ ends (**Figure 1.1 and Figure 1.2**). This terminology is derived from the deoxyribose orientation and indicates the carbon atom of the sugar where the next phosphate will be bound.

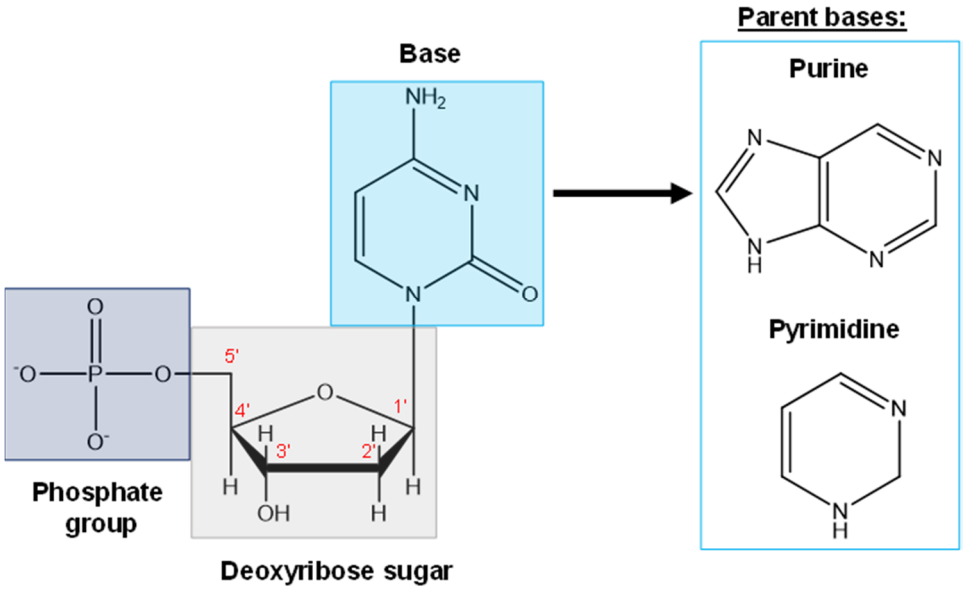

Figure 1. 1. Scheme of a nucleotide structure containing a cytosine molecule as example of base. The classification of the two existing parent bases is also shown. The numbers in the figure represent the nomenclature of the pentose sugar adopted by convention.

In the cells, the importance of this directionality (or polarity) is reflected in many aspects, for example, the synthesis of new DNA strands. This synthesis begins from an already existing strand and is carried out by DNA polymerase, which can only synthesize a new strand by incorporating nucleotides to the hydroxyl 3' end of the sugar. On the other hand, this directionality is also present in how the information contained in DNA is interpreted and copied in the cells for the subsequent encoding into proteins.

The pKa of the phosphate groups contained in the covalent backbone of DNA have a near zero value, which means that at relevant biological pH (5-9) they are completely ionized and bear a negative charge. This is the reason why DNA is an acidic molecule. In the cells, the phosphate negative charges are commonly screened by electrostatic interactions with proteins such as histones, positively charged metal ions, and polyamines.[4] Structurally, it is important to note that a new nucleotide that will be incorporated into the terminus of a growing DNA strand, contains 3 phosphate groups that will undergo a condensation reaction with the corresponding cleavage of 2 phosphate groups. So, each of the nucleotides in a DNA strand contains only one phosphate group. As a scheme, the phosphate in the 5' end can be represented by a filled blue square, while 3'

hydroxyl moiety in the sugar can be depicted as an empty space in the sugar block (**Figure 1.2**). When these two units are repetitively linked in the same orientation, they form a DNA strand.

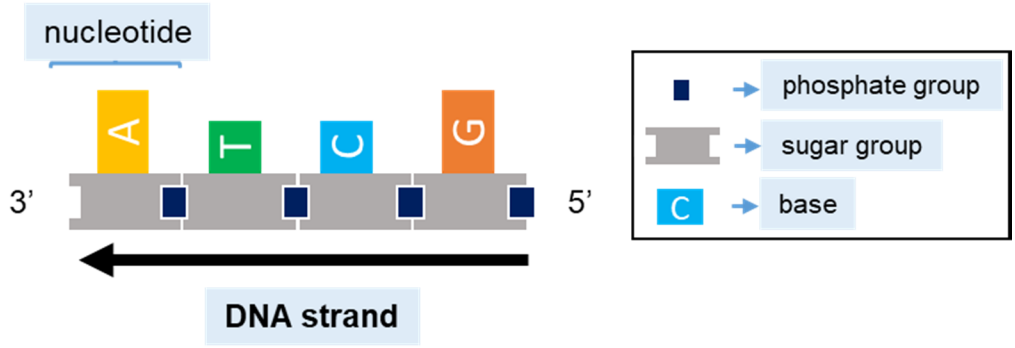

Figure 1. 2. Schematic representation of a single DNA strand formed by repetitive subunits of nucleotides.[5]

1.2.2 Secondary structure of DNA

The nucleobases are derivatives of heterocyclic organic compounds called purines and pyrimidines (**Figure 1.1 and 1.3**). Adenine and guanine are purines, which contain 2 aromatic rings and 4 nitrogen groups; while cytosine and thymine are pyrimidines and are only formed by one aromatic ring with 2 nitrogen atoms.

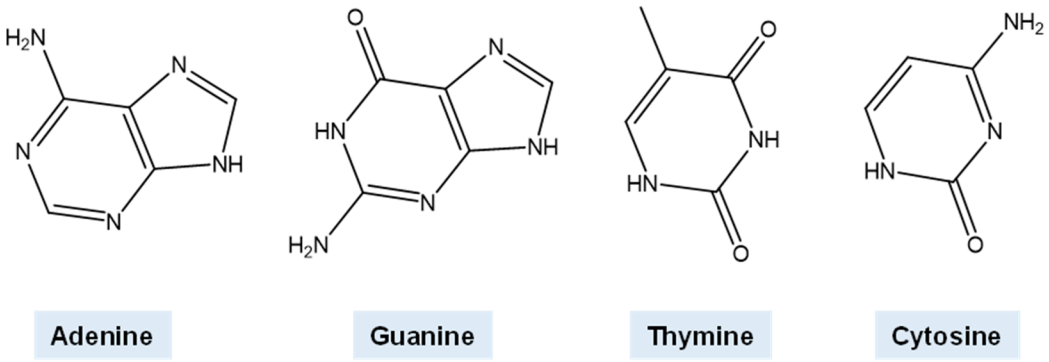

Figure 1. 3. Purine (A, G) and pyrimidine (T, C) molecular structures of the four canonical nucleobases.

Purines and pyrimidines are weakly basic molecules, which are in general, sparsely soluble at pH ca. 7 as compared with their corresponding nucleosides due to the hydrophilic nature of the ribose ring. At physiological pH, the nucleosides are neutral species.[6]

The interaction and properties of these canonical nucleobases placed in antiparallel strands forms a secondary motif, which is responsible for the final structure adopted by DNA. As shown in **Figure 1.4**, the secondary conformation of DNA derives partially from the chemical arrangement of the nucleobases, since the efficient base-pairing through hydrogen bonding, is only possible between A and T (2 H-bonds) or C and G (3 H-bonds). This complementary interaction directs the nucleobases to the most favorable packing at the inner part of the helix and the phosphate-sugar groups to the outer part. Such disposition, favors the protection of the nucleobases from environmental damage or modifications.[7]

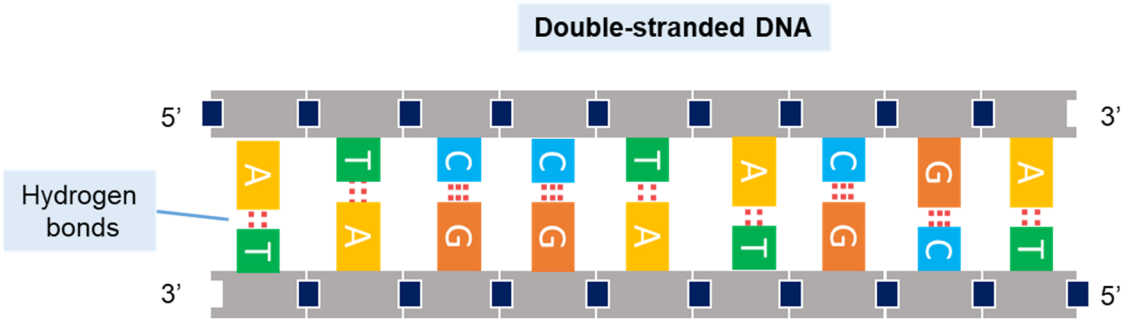

Figure 1. 4. Schematic outline of the secondary structure of double stranded DNA, composed of two antiparallel strands.[5]

In particular, the hydrogen bonding aligns the DNA strands at regular intervals. In this way, the sugar-phosphate backbone of the strands has a constant width along DNA.

1.2.3 Tertiary structure of DNA

Biologically, the double helix is the most dominant 3D structure in cells. This double helix is not the only result of base pairing, but nucleobase stacking plays the major role in its stability.[8] The aromatic configuration of the nucleobases confer to the heterocyclic bonds a partial double-bond character and enables electron delocalization. As a result, the nucleobases are almost planar structures which help to stabilize the DNA double helix through base-stacking hydrophobic interactions. These stacking stabilizing forces encompassed with van der Waals and dipole-dipole interactions help to minimize the contact between the bases and the direct contact of the bases with water molecules of the environment. To efficiently maximize the two modes of interaction (i.e., H-bonding and mainly

base-stacking) the nucleobases connected to the phosphate backbone slightly twist with each other giving rise to a double helix (**Figure 1.5**).

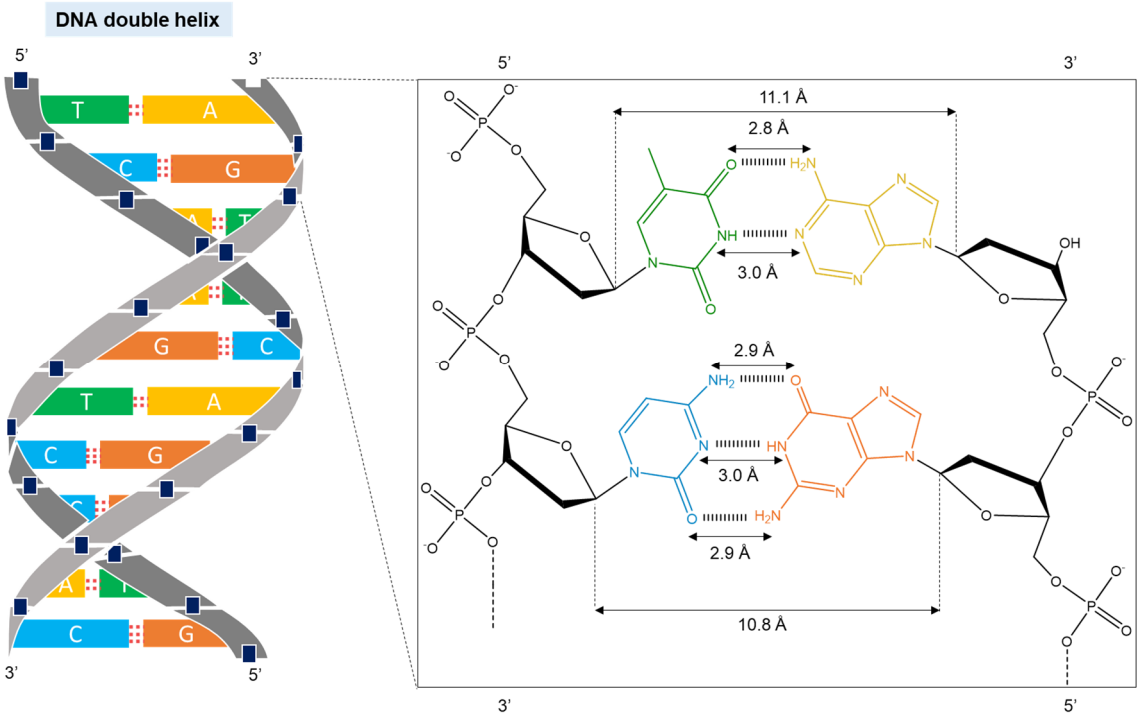

Figure 1. 5. Three-dimensional structure and composition of a B-DNA double helix.[5]

There are three main structural forms of double-stranded DNA (dsDNA): B-DNA, A-DNA, and Z-DNA (**Figure 1.6**). The structure (and consequently the function) of these DNA families can strongly depend on their base composition and surrounding environment (i.e. humidity).[9] A-DNA and B-DNA were early discovered by Rosalind E. Franklin and R.G Gosling in 1953 via X-Ray fiber diffraction.[2,10] Both forms are right-handed helixes, although in nature, most of the DNA contained in the cells resemble the B-DNA form, the helix described by Watson and Crick.[1]

In general, the A-DNA form is favored in dehydration conditions, when the number of water molecules is reduced. Thus, the sequence of stacked bases in the helix is no longer coplanar and the helix becomes distorted.[11] This deviation from the helix axis also causes structural changes from the outside of the intertwined strands, resulting in a narrow and deep major groove and a shallow and wide minor groove. Thus, this helix is wider than the B-DNA structure and contains 11 base-pairs (bp) per complete helical turn rather than the 10.5 bp of

B-DNA. Biologically, A-DNA form can be adopted in some functional cases, such as in the formation of DNA-protein complexes[12] or in the protection of the DNA integrity in bacteria, under extreme dehydration conditions.[13] On the other hand, it has been proved that in specific cases, some sequences can favor the formation of the A-DNA form, even at high humidity conditions (e.g. GAGGGA).[9]

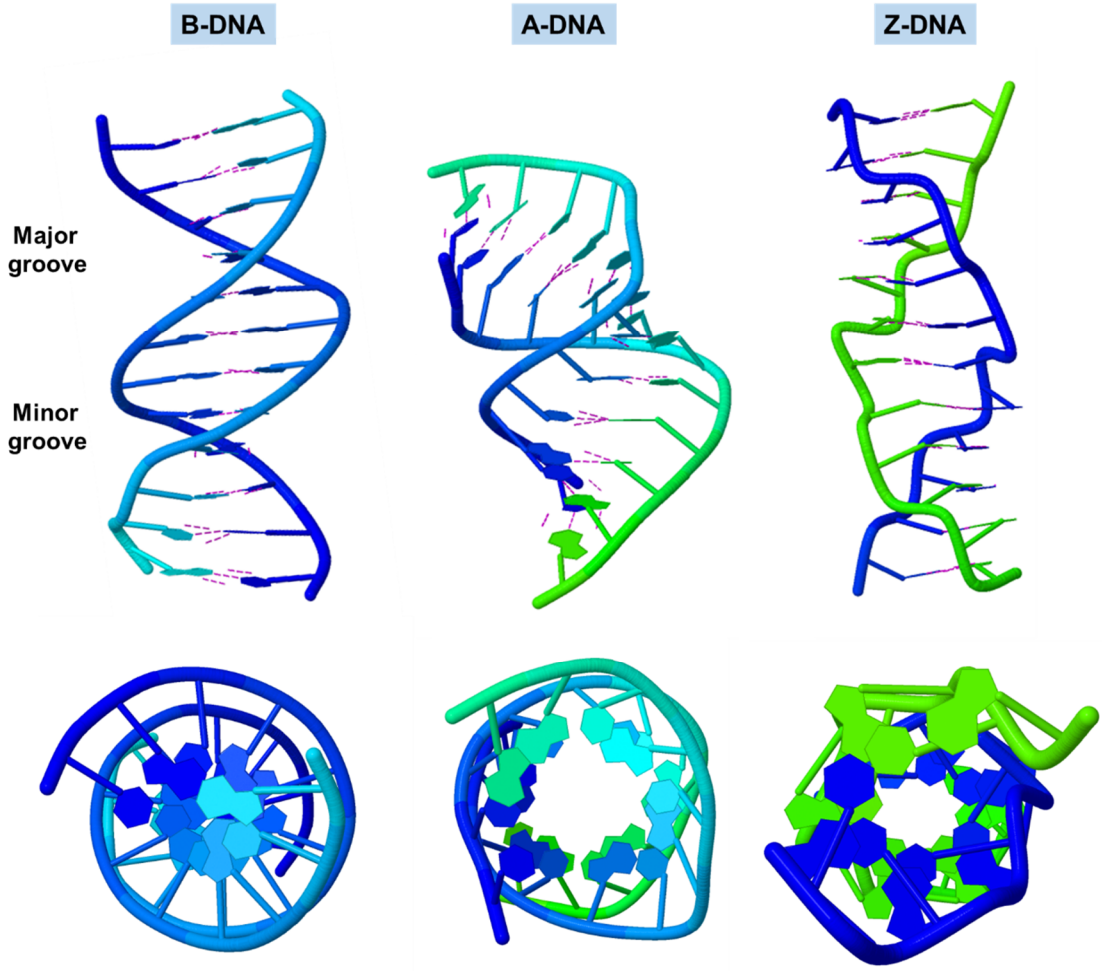

Figure 1. 6. Three-dimensional structure of the three families of DNA: B-DNA, A-DNA and Z-DNA respectively, viewed in different perspectives. Source: Protein data bank (PDB). PDB ID: 1BDNA, 5MVT and 4OCB respectively.

The B-DNA form, as previously mentioned, is the most stable form found in cells for a given random base composition. Unlike A-DNA, B-DNA is favored in normal physiological conditions and high hydration environments. Additionally, B-DNA (and Z-DNA) form contains a coplanar distribution of the bases. The outer helix backbone forms a wide major groove and a narrower minor groove with similar depths. As a result, part of the nucleobase surfaces within the grooves is

externally exposed and extra-genetic information can be accessible for other molecules such as DNA-binding proteins.

Z-DNA corresponds to the conformation that deviates more respect the B-DNA helix. The naming of this DNA arrangement comes from the elongated zigzag appearance of the helix.[14] In this case, a complete turn of the helix has 12 bp. While the major groove appears almost inexistent, the minor groove is deep and narrow. Sequences with high tendency to adopt the Z-DNA conformation are alternating pyrimidine-purines residues, especially the CpG or methylated CpG islands. This terminology refers to the two bases separated by only a phosphate group, being the cytosine (or methyl cytosine) at the 5' of the guanine. The occurrence of Z-DNA has been evidenced in short tracts of prokaryotic and eukaryotic cells and it has been speculated that it may have a role in gene expression or recombination.[15,16]

It is important to note, however, that the double helix structure of DNA is not solely found in nature as a double helix and DNA can exist in other forms. It is present for example as a single-stranded DNA (ssDNA) in some small viruses and circular (in mitochondria) or supercoiled in eukaryotic cells. This extensive variability of conformations is what makes DNA the perfect carrier of genetic information.[17]

1.2.4 Main structural differences of DNA respect RNA structure

The ribonucleic acid (RNA) is the second major variant of nucleic acid in cells. It is present in both prokaryotic and eukaryotic cells and it composes the only genetic material of some viruses. As DNA, RNA is made of a linear chain of nucleotides and is biologically involved in codification, regulation, and expression of genes. There are three structural features that make RNA different from DNA: the polymeric structure, the sugar group, and the base composition.

The nucleotide structure of RNA resembles the structure of DNA (**Figure 1.7**). The hydroxyl group in the 2' position of the sugar ring is one of the characteristics that makes RNA more reactive and not stable in alkali conditions as compared with DNA. Additionally, in terms of base composition RNA contains Uracil (U), A, C and G. U is at the place of T and base-pairs with A (2 H-bonds).

The main difference between U and T is the lack of the methyl group in the aromatic ring.

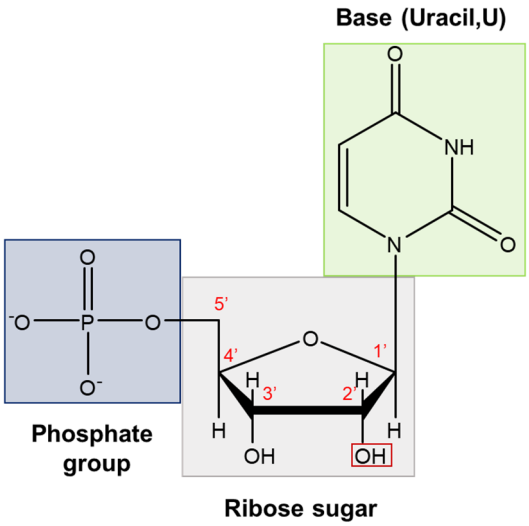

Figure 1. 7. Nucleotide structure of RNA, containing uracil as an example of nucleobase. The main difference in the sugar group respect DNA is the hydroxyl group in the 2' position, which is highlighted in red.

RNA is mainly found in a single-stranded form. It is a highly flexible molecule and it can fold through intramolecular base-pairing and take on different conformations (**Figure 1.8**).

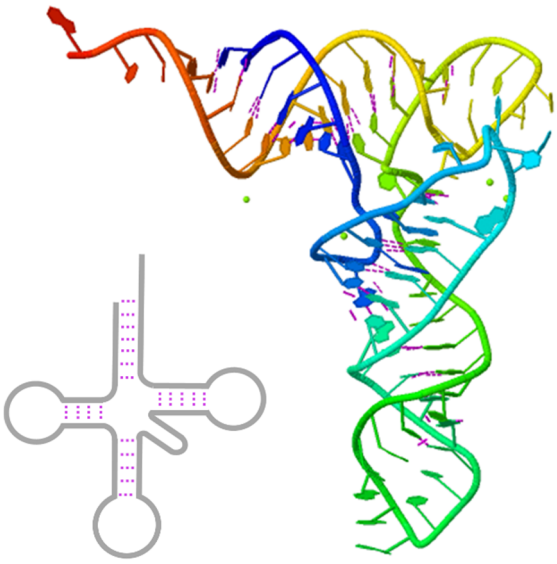

Figure 1. 8. Drawing of a secondary (left) and tertiary (right) RNA structure. Source: Protein Data Bank, PDB ID: 4tna.

Only when RNA molecules are disposed in a double helix structure, the A-form is the predominant conformation. In terms of functionality, RNA highly differs from DNA because one of its main function relies on the transmission of the genetic information contained in DNA from the cell nucleus, to the ribosomes to make proteins.

1.3. The cell cycle and heredity mechanisms contained in the DNA structure

The cell cycle refers to the series of events in which a preexisting cell duplicates its content and divides into two new daughter cells. This process is the essential mechanism of life, which determines how all living organisms reproduce and grow. In eukaryotes, the cell cycle is divided into four distinct phases: G_1 (gap 1), S (synthesis), G_2 (gap 2), and M (mitosis) as shown in **Figure 1.9**. The first three phases are known as the interphase, where the cells spend most of the time before entering into the mitotic phase. During the interface the cells grow and copy their DNA, while during the mitosis the cells divide their DNA and cytoplasm giving rise to two new cells. On the other hand, from the G_1 stage the cells may undergo into a resting phase known as G_0 if the conditions are not favorable to progress through the cell cycle.

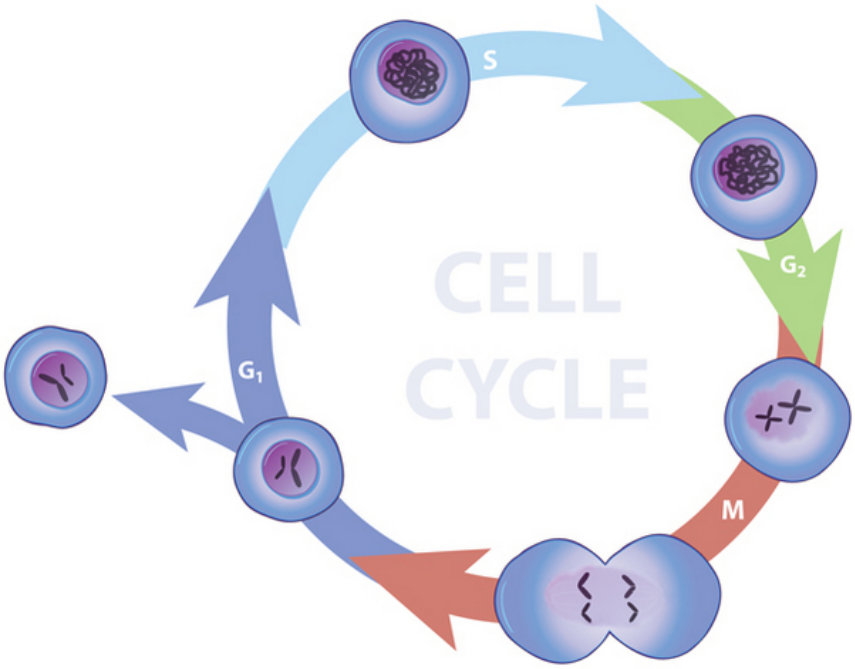

Figure 1. 9. Diagram of the cell cycle in eukaryotes. The four main stages of the cell are represented in the different colored arrows.[18]

The gap phases are important checkpoints, which ensure that the environment conditions are favorable for cells before entering into the S phase (G_1) or M phase (G_2). In this way, the cell-control system (regulatory network of proteins that control the cell cycle progression) ensure that all stages have been performed in the correct order and completed before the next phase. Most of these regulatory networks are continuously active while others are only activated if there is a malfunction at any stage of the cell cycle and as a result, the progression to the next phase is delayed. Cancer cells however, do not respond to inhibitory growth signals due to the presence of mutations in genes that guarantee the stability in normal cells. Consequently, the checkpoints and the orderly processes contained in the cell cycle are disrupted leading to an uncontrolled cell division and proliferation.

Therefore, the structural integrity of DNA is crucial for the normal progression of cells in this life cycle. It is important to know, then, the role of DNA in the different stages of the cell cycle. In the S phase, DNA serves as the foundation code for biological inheritance, because it is where cells duplicate their genetic information. At this stage, pre-existing DNA molecules are used as templates for the synthesis of new complementary strands. In this way, the genome of each cell is copied before transferring it on to its descendants. This process is known as DNA replication. On the other hand, DNA serves as the blueprint for most of the structural components of the cell, because it contains the exact instructions to make proteins. Specifically, the genes (sections that conform DNA) encode these instructions. In general, most of the functions in the cells are carried out by proteins. Enzymes are an example of proteins and are used as catalysts for many biochemical reactions in the cells.

1.3.1 DNA replication

By the time Watson and Crick discovered the structure of the DNA double helix in 1953, a theory of a semiconservative mechanism in which preexisting DNA strands serve as templates for new strands was presented. It was said to be semi-conservative by the fact that the new DNA molecules formed would contain one old-conserved strand and one new strand. However, two more possible models for the DNA replication were hypothesized at the same time: the

conservative and the dispersive mechanisms. In the conservative mechanism, a completely new DNA molecule would be synthesized from the existing parental one, whereas in the dispersive mechanism new DNA helixes would contain part of the fragments of the original DNA strands. Five years later, the semiconservative replication mechanism was experimentally supported by Meselson and Stahl[19] and it has remained true since then.

In the semiconservative model, the directionality of DNA determines how it will be replicated and several enzymes are involved in this process (**Figure 1.10**).

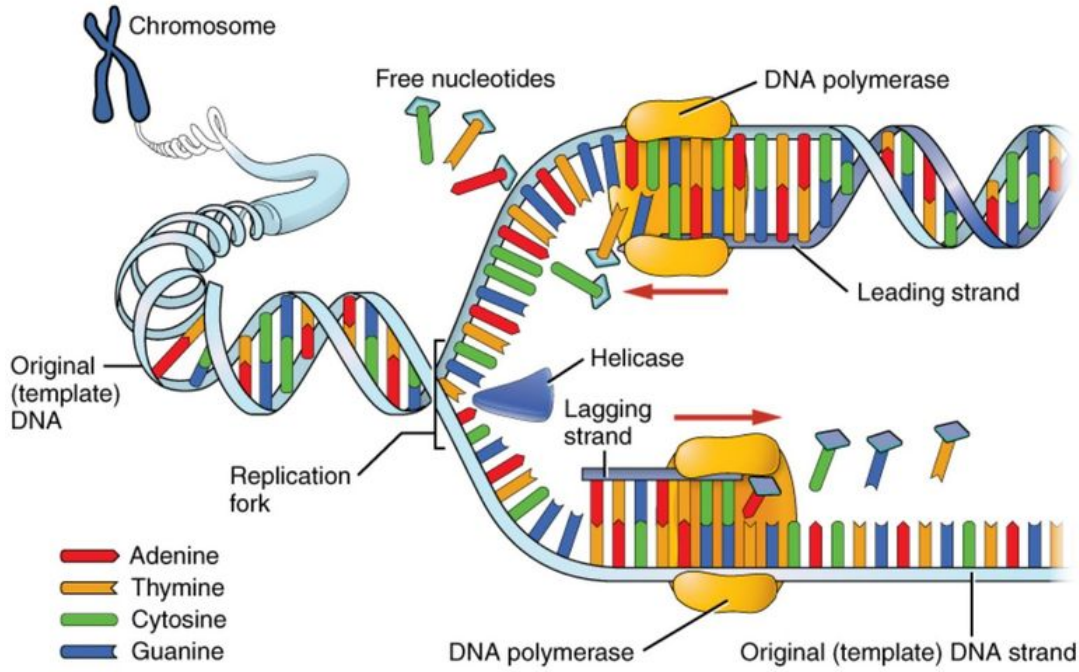

Figure 1. 10. Scheme of the DNA semiconservative replication model.[20]

In the first step, an enzyme called helicase unwinds the two antiparallel strands of the parental double helix, which results in a replication fork. In this fork, each single strand is held in place by single strand binding proteins. Then, the unzipped antiparallel strands serve as templates for the complementary synthesis of the new strands. The enzyme called primase starts the synthetic process by adding small pieces of RNA (called primer) to the strands. This is the starting point for the building of the new DNA strands. Subsequently, the enzyme DNA polymerase is able to bind to the primer and add bases one by one, only into the 5' to 3' direction. The DNA strand that runs in the 5' to 3' direction is made continuously and is named leading strand. The other strand has opposite

directionality and cannot be synthesized in the same way. The synthesis of this strand is achieved in a series of small portions known as Okazaki fragments, which also start with primer fragments. When the synthesis of DNA is completed, the enzyme exonuclease removes all the RNA fragments of both strands and another DNA polymerase fills these gaps. As the last step, DNA ligase closures the synthesized DNA molecules to form a continuous double helix.

1.3.2 Gene expression

The gene expression is a process by which the genetic information contained in DNA is transferred to RNA in order produce functional proteins (**Figure 1.11**). It was proposed by Francis Crick in 1958 and constitutes the central dogma in molecular biology. In general, it is considered to be a two-step process, where DNA is first transcribed into messenger RNA (mRNA) in the cell nucleus and then is translated outside the nucleus in the cytoplasmic ribosomes. There, mRNA is used as a template to build a polypeptide chain (composed of amino acids), which finally folds and bends in a complex tertiary structure giving rise to the protein. Both transcription and translation mechanisms comprise three main stages: initiation, elongation, and termination.

The transcription process starts with the recognition of the enzyme RNA polymerase, to a specific sequence of a gene called promoter. Promoters are A=T rich regions. Then, RNA polymerase unwinds the DNA helix and uses the strand running in the 3’ to 5’ direction as a template (the template strand) to add nucleotides in the 5’ to 3’ direction and produce the pre-mRNA. At the end of the gene, specific codons (triplets of bases) indicate the termination of the transcription and the synthesized pre-mRNA is released. Before it leaves the cell nucleus, the pre-mRNA is subjected to several modifications in the 5’ and 3’ ends and several regions are spliced out. In the splicing process, the noncoding regions transcribed from DNA (also known as introns) are removed and the coding regions (exons) are linked together. At this point, the mature mRNA is able to leave the cell nucleus.

In the cytoplasm, the translation process starts when a ribosome binds an mRNA molecule. At this stage, another type of RNA molecule, the transfer RNA

(tRNA), is in charge to transport and attach (with the assistance of other enzymes) the correct amino acid to the emergent polypeptide chain. The tRNA molecule has two recognition sites, one (anticodon) that complementary matches a codon in the mRNA and the other side recognizes the corresponding free amino acid in the cytoplasm. In this way, tRNA can read the information of the codons contained in mRNA and incorporate the proper amino acid to the polypeptide. The process ends when the last tRNA molecule reaches the termination codon of mRNA and the polypeptide chain is released folding into a protein 3D structure. In total, there are 20 types of amino acids and 64 different combinations are possible for codons. Thus, the same amino acid can be encoded by several codons.

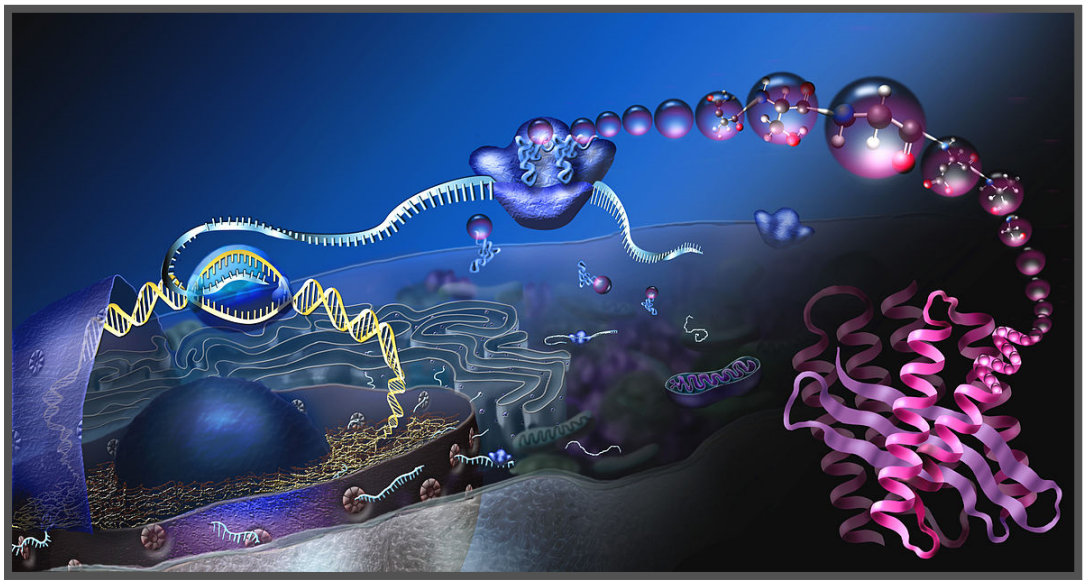

Figure 1. 11. Scheme of gene expression mechanism as a two-step process within an eukaryotic cell.[21]

In the past years, some aspects of the central dogma have been redefined, since new findings have suggested additional mechanisms. This is the case for example of the reverse transcription, where a DNA molecule is transcribed from an RNA molecule as it occurs in retroviruses such as the HIV. Or for example, the case of non-coding RNA, which can be transcribed from DNA, but not translated into proteins.

1.4. DNA point mutations

Permanent alterations in the DNA sequence of any organism are called mutations. Mutations may be beneficial, enabling evolution as a result of genetic variability, neutral or cause abnormal gene expression. Spontaneous changes, mistakes during DNA replication or environmental induced damages (i.e., radiation or chemicals) are considered to be the main triggers of the mutation occurrence. The human genome for example, contains over 3 billion of base-pairs which have to be accurately replicated before the cell division. In this process, mistakes occur, although at rates as low as 1 base-pair in every 10^{10} base-pairs.[22]

Mutations may happen in germ cells (cells that give rise to the gametes in sexually reproducing organisms) and somatic cells (the rest of cells). While mutations in somatic cells affect only individual organisms, mutations in germ-line cells may affect the succeeding generations and consequently affect both type of cells. The specific mutations in cells that occur in one or few base pairs of a gene are called point mutations. Point mutations located in coding regions of the genes or in sequences that regulate genes may lead to a substantial change on the phenotype – properties, morphology etc. – of an organism.[3]

1.4.1 Types of point mutations

There are two main groups of point mutations: base-substitutions and base deletions/insertions (**Figure 1.12**). Base-substitutions in DNA occur when a base (or a base-pair) is replaced by another base or pair of bases. This replacement may – or may not – cause a change in the mRNA transcript and consequently in the final protein structure. Within base-substitution mutations, two major groups can be assigned: transition and transversion mutations.[23] A transition mutation happens when a purine base is substituted by another purine or when a pyrimidine is replaced to another pyrimidine. On the contrary, when a purine base is changed by a pyrimidine and vice versa, the alteration is called transversion. Example of both types of base substitutions are illustrated in **Figure 1.12**. In the transition mutation example, the base-pair A–T (purine-pyrimidine) is replaced by G–C (purine-pyrimidine) while in the transversion mutation, the pair C–G

(pyrimidine-purine) is modified by G–C (purine-pyrimidine). In the frame of transition and transversion mutations, four groups (missense, neutral, nonsense and silent mutations) can be classified according to the effect on the final synthesized polypeptide chain. In the missense mutation, a nucleobase alteration in the DNA sequence causes a change in the mRNA codon which in turn results in the insertion of a different amino acid (in the example a glutamate amino acid is added instead of a lysine).

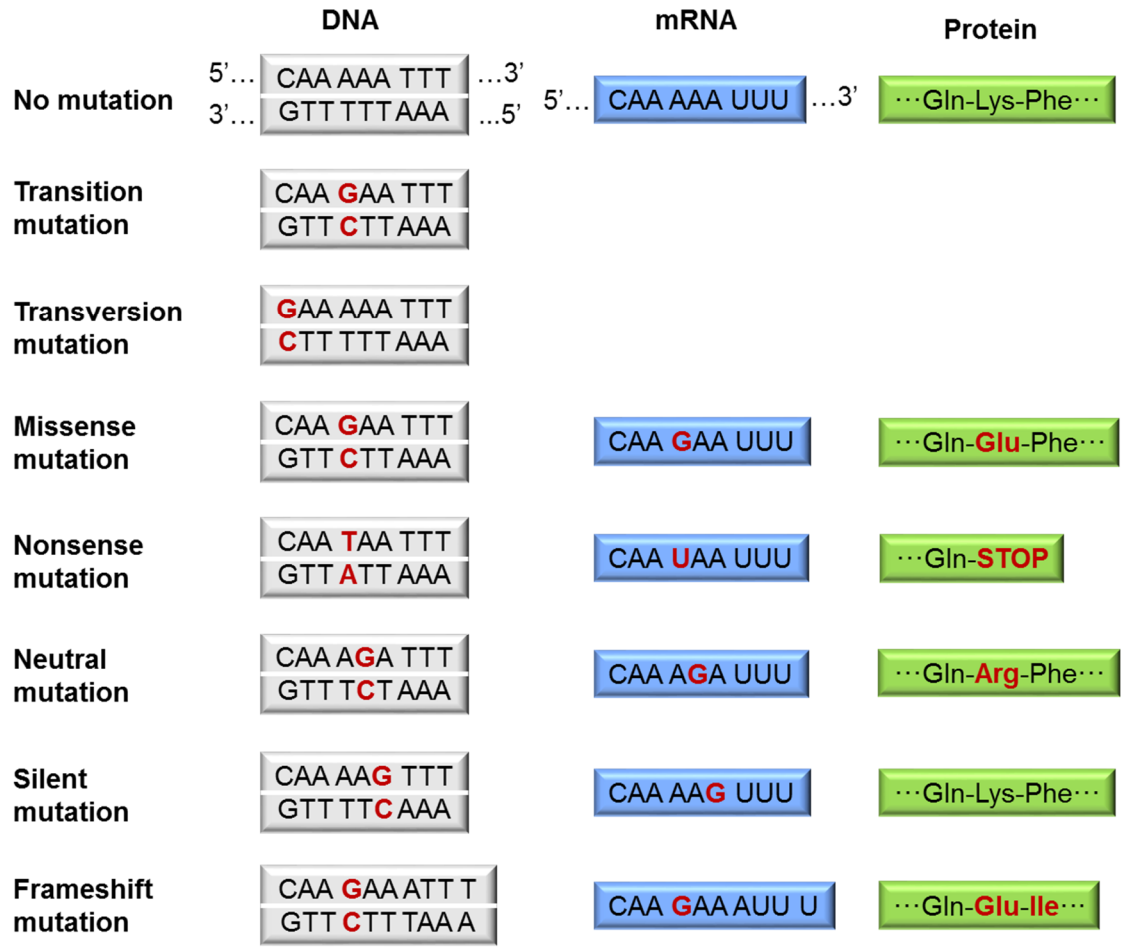

Figure 1. 12. Scheme of the different types of point mutations: base-pair substitutions and base-pair deletion/insertion mutations.

Nonsense mutations occur when a base substitution in DNA leads to a premature interruption (stop) during the translation process (e.g., UAA, UAG or UGA), so an incomplete polypeptide chain is formed. On the other hand, neutral mutations take place when the amino acid to be codified is changed by another with similar properties. In **Figure 1.12**, a change in the DNA base-pair A–T by G–C causes an alteration in the mRNA transcript which is translated to arginine

instead of lysine. Finally, silent mutations occur when there is a base alteration in DNA, although the transcribed mRNA encodes for the same amino acid and the protein results unaffected.

The second major group of point mutations corresponds to base deletion/insertion mutations. These mutations are also known as frameshift mutations and most of the times result in a nonfunctional protein. This kind of mutations may have different outcomes such as generation of a premature or late stop codon, which would result in shorter or longer proteins; or they could highly alter the sequence of the growing polypeptide chain. In the example, the insertion of a new base-pair, shifts the translation message since the mRNA translation is done per codons (per group of 3 bases). Then, the amino acids glutamate and isoleucine are translated instead of lysine and phenylalanine.

1.4.2 Main factors causing point mutations

In humans, the occurrence of spontaneous mutations is estimated to be between 10^{-4} and $4{\cdot}10^{-6}$ per gene per generation.[11] The most common spontaneous mutations are depurinations, deaminations, and tautomerisms. Depurination is the process of loss of a purine base in DNA, resulting in apurinic sites. This process is the consequence of the strength of the covalent bond between the purine and the sugar, which is more prone to breakage (hydrolysis) than the covalent pyrimidine-sugar bond. On the other hand, deamination is the elimination of an amino group from the nucleobase. Deamination of cytosine, for example, results in a uracil base (highly uncommon in DNA), or deamination of 5-methyl cytosine (one of most frequently epigenetic mutated base in mammalian DNA) yields a thymine base.[24] DNA nucleobases can also exist in two tautomeric forms; the keto-enol form or the amino-imino form. While the keto and amino forms are responsible for normal Watson-Crick base pairing, the enol or the imino form are rare forms of pairing and may produce a mutation during DNA replication.

Environmental induced point mutations are produced when an organism is exposed to exogenous agents such as radiation or mutagens (e.g., chemicals). Ionizing radiations may produce damages in DNA by causing the creation or the

removal of covalent bonds between the nucleobases (e.g., formation of thymine dimers). On the other hand, chemical mutagens may replace the canonical nucleobases, modify them or intercalate in between bases during DNA replication resulting in genetic mutations.

Consequently, point mutations may constitute a real threat to the DNA integrity and accumulation of such lesions may cause cellular disorders or even organism death if they are not properly repaired by enzymatic cellular mechanisms. However, these DNA repair mechanisms are not always 100% accurate and point mutations may stay or even arise during the DNA repair process.

1.5. Point mutations and cancer

Cancers are diseases associated to the uncontrolled division of eukaryotic cells. As briefly mentioned in the introductory part, several lines evidence that genetic roots are involved in the development of cancer.

Depending on the tissue, cell proliferation occurs at different rates and some do not proliferate unless injuries or wounds occur. For instance, epithelial cells are continuously replaced for tissue-renewal. Other cells, like heart muscle cells or neurons are more stable and may be functional for longer times or a lifetime. Point mutations in the genetic regulatory systems that control this cell division are prone to disrupt the normal proliferation cell rates and cause cancer. These mutations can broadly happen in three classes of genes: proto-oncogenes, tumor suppressor genes and genome maintenance genes (commonly referred as mutator genes). Proto-oncogenes are normal genes that are involved in the promotion of cell growth. Mutations in these proto-oncogenes transform them into *oncogenes* which may promote excessive cell growth or proliferation. On the contrary, tumor suppressor genes usually inhibit cell growth and mutations allocated in these genes can result in the stimulation of cell proliferation. Finally, mutator genes of any organism ensure the genomic integrity maintenance and control the replication accuracy. When these genes are inactivated by mutations, deregulation of the cell cycle may lead as well to cancer.

The accumulation of such mutations in these three classes of genes, frequently requires time and tumors may arise after years of accumulation, so cancers are frequently developed later in life. *Ras* oncogenes for instance, are the most frequently mutated genes in human tumors and according to the statistics, almost 30% of all tumors harbor *Ras* gene point mutations.[25]

1.6. *K-Ras* and *Ras* family of oncogenes

In humans, a group of *Ras* genes encode three closely related small proteins of ~21 KDa: H-Ras, N-Ras and K-Ras (in isoform K-Ras4a or K-Ras4b depending on the splicing process of the *K-Ras* gene).[26] These proteins are more than 90% similar in the G domain – the region of the first 168-169 amino acids, which fold in a globular domain, leaving available a guanine nucleotide (G)-binding pocket – and differ in the last 20 amino acids at the C-terminus.[27] Anchored at the interior of the cellular membrane, Ras proteins function as signal transducers between the surface cell receptors and the signal regulatory networks inside the cell. These regulatory pathways are activated or deactivated when Ras proteins cycle between "on" and "off" states, given by the conformational G-binding of guanosine triphosphate (GTP) or guanosine diphosphate (GDP) respectively. The active "on" and inactive "off" form of Ras proteins are represented in **Figure 1.13**.

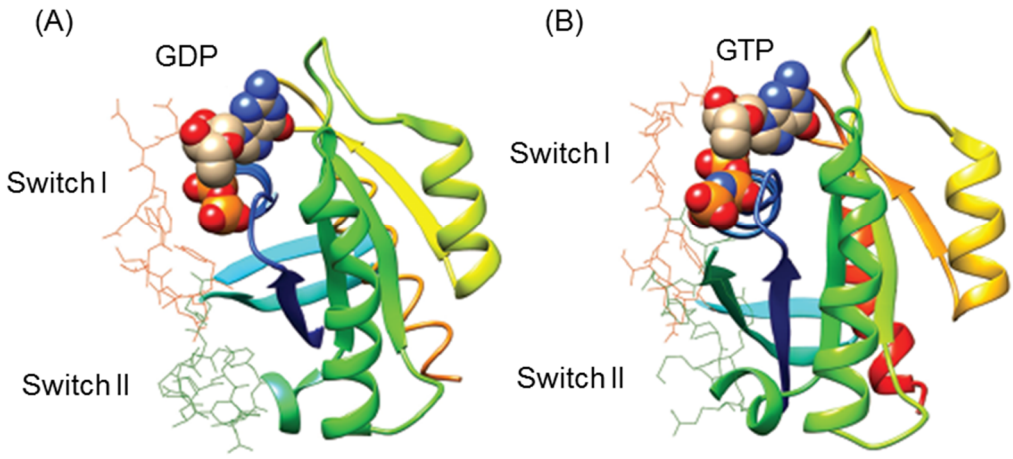

Figure 1. 13. Three dimensional structure of (A) inactive GDP-bound and (B) active GTP-bound form of Ras protein.[28,29] PDB ID:4Q21 and 5P21. GDP and GTP molecules are represented in spacefill shape and colored according to the elements (O in red, C in brown, P in orange, N in blue). Switch I and switch II domains are regions where different regulators and effectors interact with the proteins.[28]

Ras proteins are usually inactive (hydrolyzed in GDP-bound form) and become active in response to external stimuli, such as growth factors like EGF (epidermal growth factor). When active, in GTP-bound form, they promote the downstream cascade signals of protein phosphorylation. The GTP binding activity of Ras is controlled by several proteins. While the inactivation (hydrolysis of GTP to GDP) is regulated by GTPase activating proteins (GAPs), the activation from GDP to GTP form is controlled by guanine nucleotide exchange factors (GEFs). Structurally, the deactivation process takes place when GAP proteins interact in the switch I domain and the activation when GEFs interact in the switch II domain of Ras as shown in **Figure 1.13**.[30] This machinery is at the center of the regulation of fundamental cell processes such as proliferation, gene expression, apoptosis, survival, cell migration, and differentiation.[31] **Figure 1.14** highlights the main upstream signaling and effector pathways driven by the Ras proteins.

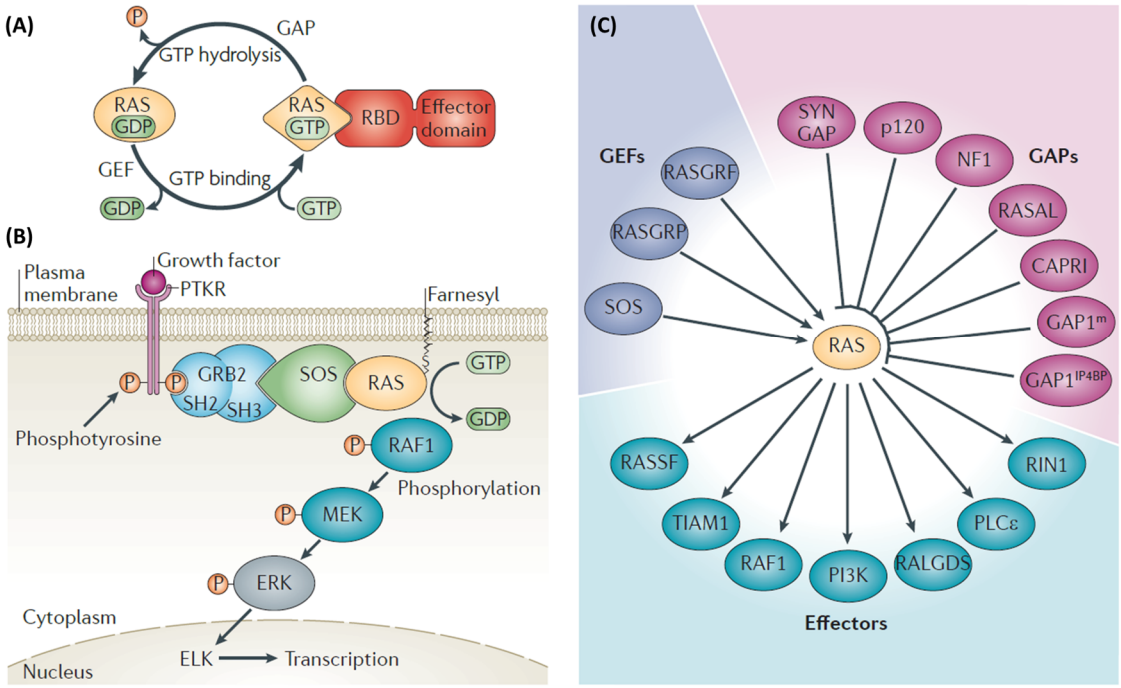

Figure 1. 14. Main Ras downstream signaling pathways related to the development of several cancers in the presence of genetic mutations. (A) Activation of GDP-Ras by GEF enables Ras to bind effectors in the Ras-binding domains (RDBs). GAP returns Ras to the inactive form (B) Ras-Raf1(Rapidly accelerated fibrosarcoma 1 kinase)-MEK(Mitogen-activated protein/extracellular signal-regulated kinase)-ERK(Extracellular signal-regulated kinase) downstream signaling cascade, commonly deregulated in cancer. (C) Reported GEF-activating and GAP-deactivating regulators of Ras and downstream effector pathways.[27] Reprinted with permission from Ref.27. Copyright 2012, Nature Publishing group.

Among others, the most characterized signaling effector cascade is the Raf1-MEK-ERK cascade. This cascade initiates when Ras-GTP activates the kinase activity of Raf1, the first protein in the cascade. At this stage, a cytoplasm-based phosphorylation of proteins (the mitogen-activated protein kinase cascade, MAP) is stimulated and ultimately leads to ERK phosphorylation. When ERK moves to the cell nucleus, several transcription factors activate, initiating the transcription of some division-promoter genes. The eventual activation of such growth factors, may lead to the progression in cell cycle.

Therefore, Ras proteins are vital in controlling many signaling pathways inside the cell. However, if oncogenic point mutations take place in the genes codifying Ras, the final protein may result insensitive to the GAP-mediated hydrolysis to GDP (its self-limiting form) and remain continuously activated even in the absence of external stimuli. This continuous delivery of the Ras message may result in different outcomes such as aberrant control of the cell cycle, increased proliferation ability, reduced response in the apoptosis, increase the invasive properties of the cells (change in mobility and cellular adhesion) and ultimately lead to the development of cancer.[26] It has been proved that these oncogenic point mutations in the three human Ras isoforms (*K-Ras*, *N-Ras*, and *H-Ras*) are tumor-specific.[32] Of these three, *K-Ras* is of particular interest because is the most frequently mutated oncogene which derives in pancreatic (~70-90% incidence), colorectal (~50%) and non-small-cell lung cancer (~25-50%).[33] Its codifying sequence it is well-known, as well as the “hot-spot” codons where point mutations usually occur. The most common mutations are prevalent at positions 12, 13 and 61 and most of them are missense point mutations.[34,35] Although, mutations in other codons have been also described in literature.[30,36] The occurrence frequency of these mutations in human cancers is shown in **Figure 1.15**.

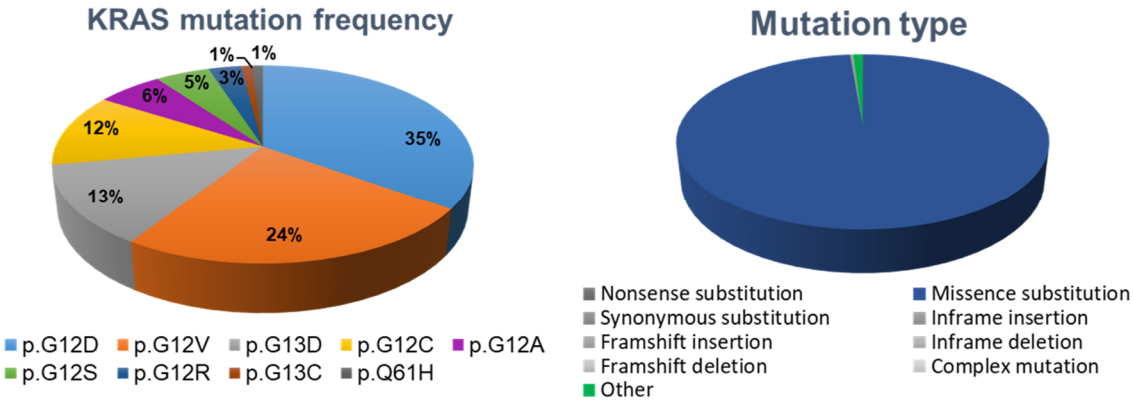

Figure 1. 15. Diagram of the most frequently mutated residues in the human *K-Ras* gene and types of point mutations found in the gene.[25,36] Data obtained from the Catalogue of Somatic Mutations in Cancer (COSMIC) database.

The prognosis in each of these cancers highly differs on the type of mutations harbored in the *K-Ras* gene. For example, $KRas^{G12V}$ mutations in colorectal and lung carcinomas have worse prognosis than $KRas^{G12D}$ mutations.[26] In other words, the type of mutation may define the aggressiveness characteristics of harbored cancer.

1.7. Conventional and emerging methods for detection of point mutations

A wide variety of analytical tools for the detection of known and unknown point mutations have been developed. The choice of the technique highly depends on different variables such as infrastructure availability, costs, number of necessary tests and time required for the analysis. Among others, the most common methods used in molecular diagnosis span from electrophoretic, enzymatic, solid phase-based methods, denaturing high performance liquid chromatography, real-time polymerase chain reaction (PCR), and next generation sequencing technologies (NGS). The first four methods often require a pre-amplification step of DNA by PCR prior the implementation of the technique.[37] A brief description of the molecular diagnostic methods is summarized below.

- Electrophoretic-based methods. Single strand-conformational polymorphism (SSCP) is one of the most spread electrophoretic methods, widely used in molecular biology as a mutation scanning technology.[38-41] This technique is based on the different

electrophoretic mobility that wild-type and mutant ssDNA have in a non-denaturing gel, based on certain experimental conditions. Under these conditions, ssDNA fragments can fold into unique 3D conformational geometries molded by intramolecular interactions delineated by the specific nucleobase sequence.[39,40] Outstandingly, even single-base substitutions can produce changes in the secondary structure which can be detected by monitoring the diverse mobility of the ssDNA fragments on a non-denaturing electrophoresis gel.[39,40] The length of the ssDNA plays a key role in determining the single-base discrimination sensitivity of SSCP, with 100 to 600-nt being approximately the optimal size range.[41] In fact, while single base substitution has lesser chance to significantly perturb the overall folded state in exceedingly long ssDNA, too small fragments show reduced ability to form stable and reproducible high-order structures.[42] Similar principles are applied in heteroduplex analyses (HDA) and capillary electrophoresis using non-denaturing gels. Other techniques based on denaturing gels (gels where DNA extend linearly) such as denaturing gradient gel (DGGE) and temperature gradient gel (TGGE) electrophoresis have been developed. Although in this case, the structure of DNA is disrupted and extended linearly, so the difference in mobility is driven by the mass-to-charge (m/z) ratio and its linear length.

- Enzymatic-based techniques. Restriction fragment length polymorphism (RFLP) was one of the first methods developed for molecular diagnosis and it is based on the cleavage of DNA sequences with restriction enzymes. The resulting restriction fragments are separated by gel electrophoresis. Alternative enzymatic approaches such as oligonucleotide ligation assays (OLA) have been used. The mechanism mainly involves the prior hybridization of primers to the target DNA sequence and the use a short complementary oligonucleotides covalently linked with a fluorescent dye or radiolabelled tags. No ligation occurs by the enzyme ligase if the sequences are not full complementary. The ligated products can

be detected by enzyme-linked immunosorbent assay (ELISA), fluorimetric means or using a phosphorimager.

- Solid-phase based methods. The essence of these methods relies on the use of short labelled ssDNA fragments as hybridization probes for the target amplified DNA sequence. Allele specific oligonucleotide (ASO) approach is one of these techniques, where the short DNA fragment is previously label with radioactive, fluorescent or enzymatic means. This principle was extended later on to DNA oligonucleotide microarrays (also known as DNA chips). In microarrays however, the system is reversed and the single-stranded DNA probes are unlabeled and fixed on a support while the target single-stranded DNA is labelled with a fluorescent dye.
- Denaturing high performance liquid chromatography (DHPLC). The presence of a mutation in a PCR-amplified dsDNA fragment can be revealed by the different retention times of the homoduplex (normal dsDNA) and the heteroduplex (dsDNA containing the mutation) on a reverse phase HPLC under partial denaturing conditions.[43] The different melting points of the duplexes determines the different retention times. The eluted DNA duplexes are subsequently monitored by fluorescence or UV-visible absorption.
- Real time-PCR. This approach enables amplification and detection of the target DNA sequence in the exponential phase of the reaction by means of fluorogenic tags, based on Förster resonance energy transfer (FRET) and sensitive detection equipment. This technique is also known as TaqMan assay.
- Next-generation sequencing technologies. Before NGS, Sagner sequencing (dideoxy sequencing) was the first sequencing technique employed in the 1970's. Later on, an automated pyrosequencing method was developed and is the foundation of the NGS technologies. In the pyrosequencing method, the target DNA is denatured and the ssDNA running in the 3' to 5' direction is attached to micrometric beads and used as a template for the synthesis of the complementary strand. To do so, a mixture containing DNA polymerase, primer and other enzymes is added. When a new

nucleotide is introduced to the growing strand, a pyrophosphate molecule (containing two phosphate groups covalently linked) is released. This molecule is then converted to ATP and a final enzyme (luciferase) uses the produced energy in the formed ATP to emit light, which is then related to the nucleotide incorporation. This technique can be used to determine short sequences, although can be automated for high-throughput screening.[44] Three approaches exist for NGS technologies, the whole-genome shotgun sequencing (WGS), custom target sequencing microarrays (TSMs), and whole-exome sequencing (WES). WGS, for instance, is used to sequence the whole genome by breaking the genomic DNA into partially overlapping fragments. These fragments are copied, sequenced and assembled using computer algorithms.

All the described techniques present inherent advantages or disadvantages that need to be considered for the specific point mutation determination. Electrophoretic methods, for example, are relatively inexpensive due to the fact that the required equipment is routinely found in laboratories. However, they are highly empiric techniques, time-consuming, and there are sparse general guidelines for their use. SSCP, for instance, is highly dependent on temperature and the presence of point mutations may or may not be detected if the experimental conditions are not the adequate. Additionally, the results obtained may be difficult to interpret and the fragment size is a limitation in terms of sensitivity.[45] On the other hand, enzymatic-based techniques such as OLA are considered simple and relatively inexpensive techniques if the PCR costs are excluded. Like most ligation assays, the technique may fail if other mutations are present near the ligation site leading to indeterminate results.[46] Solid phase-based methods are techniques that have a high potential for automation and high-throughput screening. DNA chips are an example where many point mutations can be detected simultaneously. In this case, the hybridization dependence on the spotted DNA fragment length can be an issue as well as the efficiency of the dyes.[47] Not all dyes are suitable for biodiagnosis and limitations such as photobleaching and non-specific vibrational information (broad absorption and emission bands) hamper their full implementation.[48] In the case of DHPLC, it is a

technique that can be automated and no labels are required for the analysis. However, the temperature in the column has to be empirically optimized for each amplified DNA fragment in order to achieve the correct degree of denaturation.[49] Additionally, the nature of the mutations, as most of the other techniques, has to be determined by other methods such as sequencing.[45] Real time-PCR offers the advantage of simultaneous detection and quantification with high sensitivity.[50,51] Nevertheless, the major drawbacks rely on the fact that each point mutation requires a specifically designed expensive probe, the process for DNA detection is complex, and its implementation in multiplexing assays is highly challenging (detection of several target sequences in the same analysis).[52] On the other hand, next generation sequencing methods enable detection of point mutations with single base sensitivity in large samples. However, expensive equipment is required and the large amount of data generated is still an important issue to handle and more advances need to be done.[53]

Overcoming the intrinsic limitations of the conventional techniques for the detection of point mutations is still one of the major goals in science. Further research is needed for the exploitation of new strategies capable of combining sensitivity (PCR-free strategies), specificity and fast analysis in a low-cost manner.

In recent years, integration of nucleic acids (NAs) and nanoparticles (NPs) has generated a wealth of research in the area of nanotechnology, with particular emphasis to nanostructures with unique physicochemical properties such as noble metal nanoparticles. As a result, an increasing number of NA-based nanotechnologies is continuously emerging, finding a diverse set of applications in biomedicine, sensing, bioelectronics, biocomputing etc.[54-57] In particular, surface-enhanced Raman scattering (SERS) has emerged as a valuable bioanalytical tool for the interrogation of NAs with extraordinary sensitivity.[58,59]

1.8. Surface-enhanced Raman spectroscopy: General concepts

1.8.1 Basic theory of Raman scattering

Raman spectroscopy is a spectroscopic technique that relies on the inelastic (Raman) scattering to acquire a structural fingerprint of the molecular system when illuminated with a monochromatic light (typically, in the near ultraviolet to near infrared range). The Raman effect was historically postulated in 1923 by A. Smekal and experimentally demonstrated in India by Chandrasekhara Venkata Raman and Krishna in 1928.[60,61] Two years later, C.V. Raman received the Nobel Prize in physics for the discovery.

When a monochromatic light from a laser source (composed of elementary particles known as photons) impinges on matter, the light can be absorbed, scattered, reflected or transmitted (without interacting with the material). In general, absorption requires that the energy – given by the Planck equation $\Delta E = h\nu$ – of the incident photon, matches the energy gap of the ground (S_0) and excited state (S_1) of the molecule. This process is outlined in **Figure 1.16**. In contrast, light scattering can occur without this matching condition.[62] For the sake of clarity, the scattering process can be approximated as a two-photon event, where a molecule simultaneously absorbs the incident photon and radiates another photon (the scattered photon).[63] This first interaction of the incident monochromatic light with the molecular vibrations, distorts (polarizes) the electron cloud of the molecule inducing a dipole moment and directs the molecule to a short-lived virtual state.[64] Due to the unstable nature of this virtual state, the molecule relaxes to the ground state emitting instantaneously a photon.

Most of these emitted photons (99.99999%) are scattered with the same incident energy, in any direction, in a process known as elastic or Rayleigh scattering.[65] A small fraction, however, is scattered at different energy with respect to the incident photon (inelastically scattered) and the emitted photons can either gain (anti-Stokes scattering) or lose energy (Stokes scattering) as shown in **Figure 1.16**. This change in energy is the result of the interaction of the photons with the molecular vibrations of the analyte. Raman spectroscopy is focused on the collection of these inelastically scattered photons, which provide

specific information of molecular vibrations that can be used for identification and quantification of analytes.

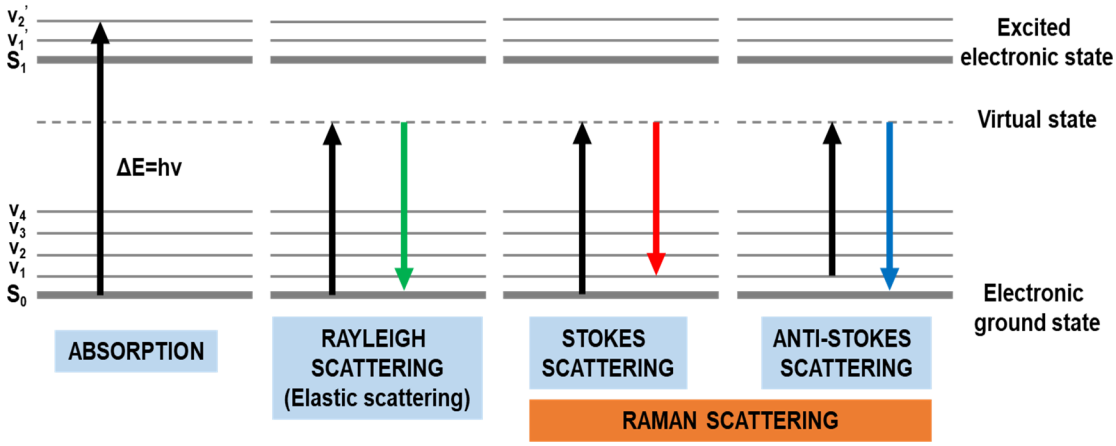

Figure 1. 16. Simplified Jablonski diagram of absorption, Rayleigh and Raman scattering processes. In the Planck equation, the energy (E) is the product of the Planck constant (h, $6.62 \cdot 10^{-34}$ J·s^{-1}) and the frequency of radiation (υ).

1.8.2 Raman spectrum

Raman spectra are routinely represented in terms of Raman intensity as a function of wavenumber ($\tilde{\nu}$, cm^{-1}) — rather than the wavelength (λ, nm), the unit of radiation. This terminology is especially useful in spectroscopy because, first, the Raman effect is often described in terms of energy and, second, $\tilde{\nu}$ is directly proportional to energy in the Planck equation (**Equation 1.1**). In a Raman spectrum therefore, we can either find in the x axis "wavenumber ($\Delta\tilde{\nu}$)" or "Raman shift", which represent the energy loss/gain of the photons during the scattering process.[66]

$$\Delta E = E_L - E_S = h\upsilon = \hbar\omega = hc\tilde{\nu} = \frac{hc}{\lambda} \qquad (1.1)$$

Where, E_L is the energy of the incident photon, E_S the energy of the scattered photon, h the Planck constant (J·s^{-1}), υ frequency (s^{-1}), ω the angular frequency (rad/s), $\tilde{\nu}$ the wavenumber (cm^{-1}), c the speed of light constant (m/s) and λ the wavelength (nm).

Any Raman spectrum is divided into two main regions (anti-Stokes and Stokes scattering regions) separated by an intense Rayleigh scattering section

(**Figure 1.17**). It is important to note that both regions have positive or negative wavenumbers depending on the difference in energy of the scattered photon. If the scattered photon (E_S) has more energy than the incident one (E_L), the Raman shift is negative (anti-Stokes process).

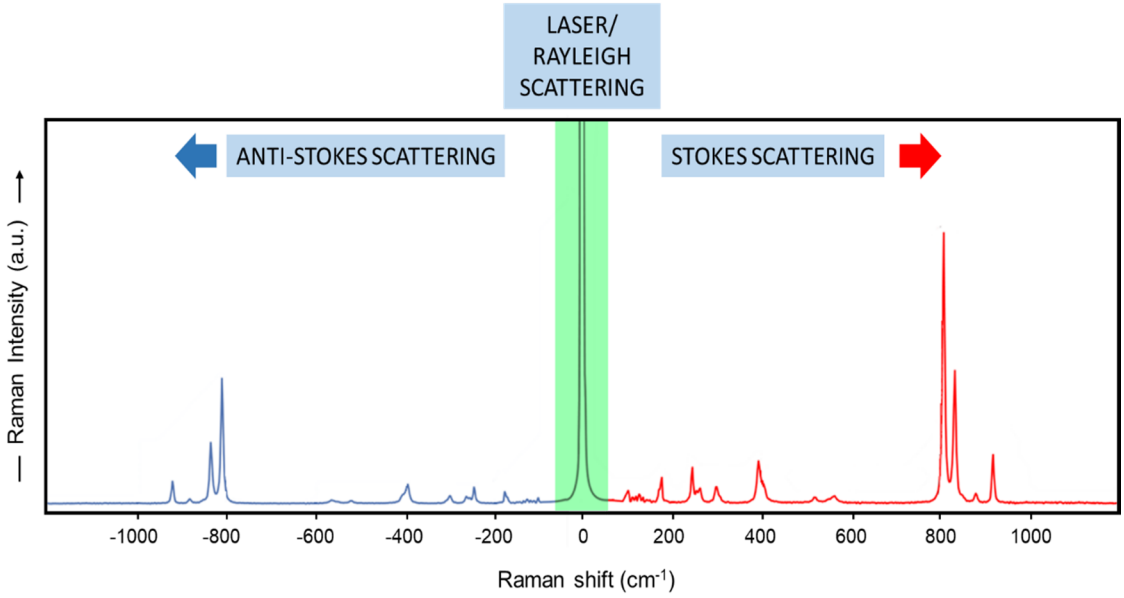

Figure 1. 17. Example of a typical Raman spectrum, where the inelastic (Stokes and weaker anti-Stokes scattering) and elastic scattering are represented.

On the contrary, if the scattered photon has less energy than the initial photon, the Raman shift is positive (Stokes scattering). Near to the excitation region (Rayleigh scattering region), the wavenumber is zero along the x axis, because there is no frequency shift from the incident light. In Raman instrumentation, the elastically scattered light is efficiently blocked by means of filters.

In the anti-Stokes side, the vibrational bands are usually weak — and most of the times ignored — as compared to the Stokes region. This weakness in signal intensity is caused the population distribution of molecules at equilibrium, which is given by the Boltzmann law in **Equation 1.2**.

$$\frac{N_1}{N_0} = e^{-\frac{(E_1 - E_0)}{k_B \cdot T}} \tag{1.2}$$

Where, N_i is the number of molecules in the vibrational level i of energy E_i, k_B is the Boltzmann constant ($1.38 \cdot 10^{-23}$ J K^{-1}) and T the temperature (K).

For the anti-Stokes process to occur, the molecules have to be in an excited vibrational state first (**Figure 1.16**) and this fact implies thermal energy because at room temperature most of the molecules are in the ground state. This is one of the reasons why most of the times the anti-Stokes signal is low, but the signal can become exponentially weaker as the energy of the molecular vibration increases (which is implied in the **Equation 1.1** (ω) and consequently in **Equation 1.2**).[66] Therefore, most Raman studies are carried out in the lower energy region (Stokes), were more intense vibrational bands are obtained. Although in certain occasions, anti-Stokes scattering may be useful for example, to avoid interference from fluorescence, analyze highly fluorescent samples or to monitor vibrational changes as a function of temperature.[65]

1.8.3 Raman polarizability and Raman cross section

For a molecule to exhibit a Raman effect, a change in polarizability with respect to the vibrational coordinate corresponding to the vibronic state is required. As previously mentioned, when the oscillating electric field of the excitation light strikes a molecule, it distorts (polarizes) the electron cloud surrounding the nuclei of the molecule and induces a dipole moment (**Equation 1.3**). The measure of this distortion or dipole moment induction is the polarization (α) and can be understood as a constant of the deformability of the molecule.

$$\mu = \alpha \cdot E \tag{1.3}$$

Where, μ is the induced electronic dipole moment, E the incident electric field and α the polarizability of the molecule.

The polarizability of the molecule is directly related to the intensity of Raman scattering, i.e. larger changes in polarizability imply larger Raman scattering. However, it is important to note that not all the vibrational modes of the molecules give rise to strong Raman scattering, and the intensity varies from one mode to another. For example, symmetric stretches in Raman usually result in the highest scattering because they are caused by larger changes in polarizability. On the other hand, centrosymmetric molecules are not Raman (neither IR) active because the reflection at any point through the center of the molecule reaches the identical place on the other side.[62] These considerations are based in Raman

selection rules, which will not be further discussed in the scope of this thesis, although the reader can refer to specialized literature.[48]

On the other hand, the molecular polarizability is also correlated to the scattering cross section (either Rayleigh or Raman scattering) of the molecule, which provides fundamental insights of the molecular properties.[67] A scattering cross section (σ) is defined as the probability of interaction between two particles or in other words, the effective area for collision. It is measured in surface units (m^2) and most of the times depends on the excitation wavelength and the refractive index of the environment. In simple terms, the scattering cross section can be described as **Equation 1.4**.

$$P = \sigma \cdot S_{Inc} \tag{1.4}$$

Where, P is the intensity or power of the produced signal (W), σ the cross section (m^2) and S_{Inc} the incident power density ($W \cdot m^{-2}$).

Equation 1.4 is a simple definition of cross section and only applies for linear processes because, here, the observed intensity of scattering (P) is directly proportional to the incident power density. The scattering process is, however, a more complex optical effect, determined also by the molecular orientation with respect to the incident field polarization.[66] For this reason, the value of scattering cross section obtained empirically refers to an average of many analyte molecules in random orientations. Taken this consideration into account, the Raman cross section can be more precisely expressed in differential form, as the absolute differential Raman cross section (**Equation 1.5**).

$$\frac{dP_{Sca}}{d\Omega}(\Omega) = \frac{d\sigma_R}{d\Omega} \cdot S_{\mathrm{Inc}} \tag{1.5}$$

Where, $\frac{dP_{Sca}}{d\Omega}$ is the angular dependence of the scattered power, $\Omega = (\theta, \phi)$ the angles that specifies the direction, and $\frac{d\sigma_R}{d\Omega}$ the differential Raman cross section.

Therefore, the value of σ can be used to estimate the Raman scattering strength for a given band in the Raman spectrum because, the larger the cross

section, the strongest interaction, and the larger probability of collision between a photon and the molecule.

1.8.4 Transition from Raman scattering to SERS

Raman spectroscopy, as previously discussed, offers a unique vibrational fingerprint of the target molecule. It is characterized by high versatility and analytical potential by the fact that analytes can be measured in almost any kind of matrix, with minimum or null sample preparation under the original (chemical, thermodynamic etc.) conditions.[68,69] Moreover, Raman studies can be performed over a wide spectral range (normally in the visible and near-IR range) for any kind of molecular system and the excitation wavelength is not restricted to the optical properties of the analyte molecule.[70] Notably, the invention of the laser in the 1960s to be used as a powerful monochromatic light source, supposed a breakthrough in the Raman spectroscopy, which is now a well-established technique used in many fields such as art and heritage, materials science, vibrational and biomedical studies, forensic science and pharmaceutical studies.[71-73]

However, the implementation of the technique to chemical analysis of compounds at low concentrations has been historically hampered by the lack of sensitivity. In fact, the Raman effect is inherently weak for the vast majority of molecules (only 1 every 10^6-10^8 photons is inelastically scattered).[62] Only in specific cases the sensitivity is improved, such as for Resonance Raman (RR) scattering, when the incident laser frequency is close in energy to an electronic transition of the analyte. Under this condition, the Raman scattering can be greatly enhanced up to several orders of magnitude, facilitating the study of these classes of compounds at lower concentrations.

To this point, in 1974, Fleischmann et al. reported for the first time the observation of an unexpected Raman signal enhancement from pyridine, in the presence of rough silver electrodes.[74] However, it was not until 1977 when a series of independent reports of Jeanmaire et al., and Albrecht et al. correctly interpreted the origin of the enhancement.[75,76] In their publications, they demonstrated that the presence of the noble metal with features at the nanoscale

range was at the heart of the enhancement. This first discovery and the subsequent technological development in instrumentation and optics paved the way for the application for chemical analysis of the technique, in the new terms of surface-enhanced Raman scattering (SERS).[77]

Therefore, the effective detection of any analyte molecule by SERS resides in the presence of a nanostructured metal surface (mostly silver or gold). This is an indispensable condition for SERS, which differs from Raman scattering because it is not only based on the light-matter interaction. SERS benefits from the optical properties of nanostructured metals and their resonant interaction with the electromagnetic radiation of light. It is also worth mentioning that when SERS experiments are performed under resonant Raman conditions (i.e., the analyte has a chromophore close in energy to the frequency of the excitation source), both plasmon resonance and molecular resonance from the analyte multiplicatively contribute to the final enhancement (surface-enhanced resonance Raman scattering – SERRS).[78]

In the past ten years, the emerging of the nanotechnology-based techniques, especially for SERS, has become evident (**Figure 1.18**).

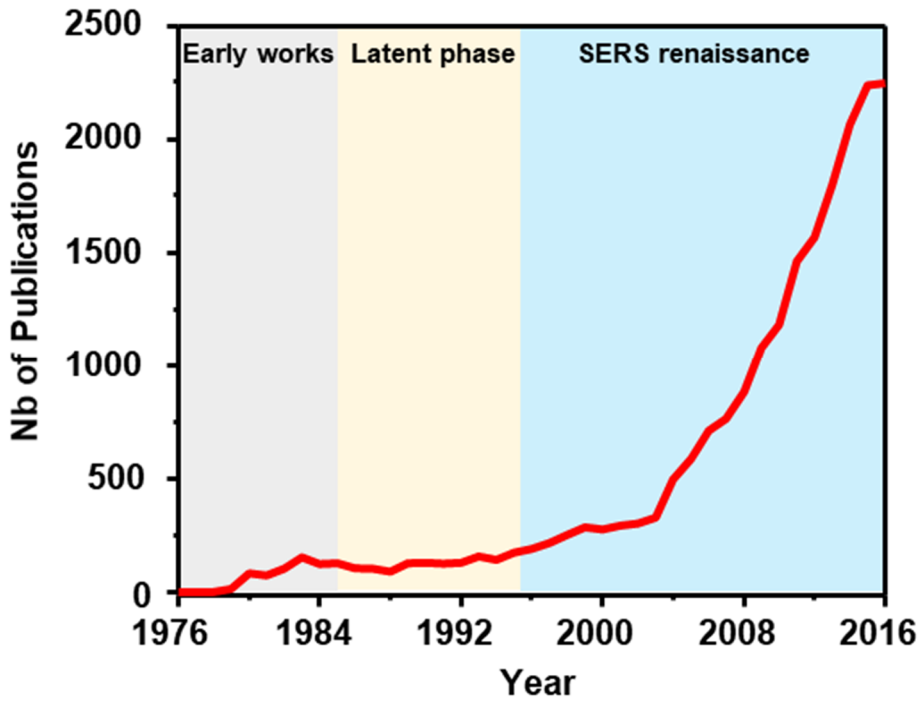

Figure 1. 18. Number of publications containing the title-only “Surface enhanced Raman” from the early works in 1977 until 2016. Data obtained from Scopus database.

This fact can be reflected following the publications containing the words "surface-enhanced Raman" from the database Scopus in **Figure 1.18**. Although the number of publications in this case should be normalized to the total number of publications, it can give a hint of the gain in importance of the technique.

1.8.5 Electromagnetic enhancement and additional mechanisms

The origin of the Raman signal enhancement in SERS can be explained as a result of two multiplicative effects: the electromagnetic (EM) enhancement and, facultatively, the chemical (CE) enhancement. Both mechanisms are schematically depicted in **Figure 1.19**. The EM enhancement is the dominant effect and constitutes the *conditio sine qua non* to observe SERS. EM mechanism relies on the enhancement of the local electromagnetic field originated in close vicinity of metals with features in the nanoscale range. It is associated with the excitation of localized surface plasmon resonances (LSPRs), which are collective oscillations of conduction electrons, generated on the metal surface with an incident light beam.[79] When the oscillating electromagnetic field of light interacts with the free electron cloud in the metal, it transposes them with respect to the ionic lattice of the metal and subsequently a restoring force turns them back to the equilibrium.

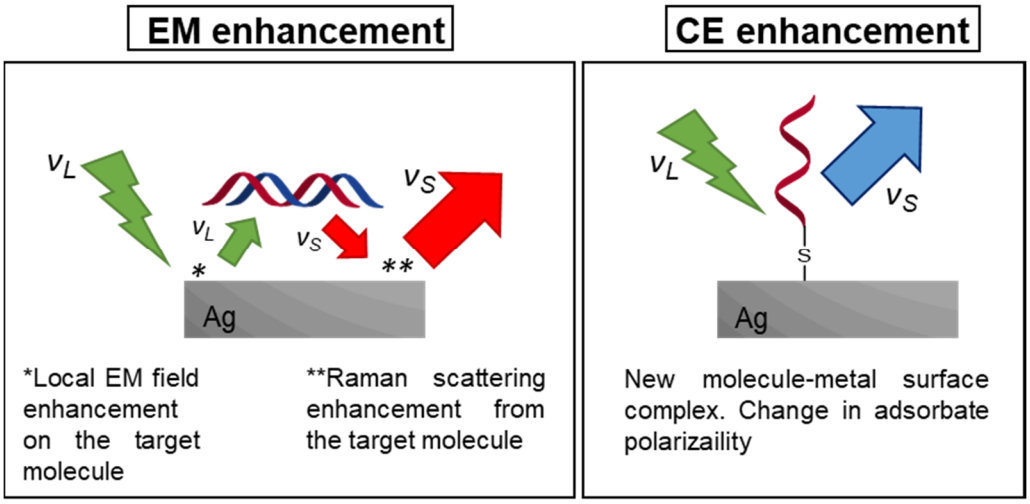

Figure 1. 19. Schematic EM and CE enhancement mechanisms experienced by DNA molecules in close proximity to a nanostructured metal surface. In the graph, ν_L and ν_S are the frequencies of the laser and scattering respectively.

Thus, metallic nanoparticles can be seen as an oscillating system originating resonances at specific wavelengths (**Figure 1.20**). As a result, large local electric

fields are confined at the metal surface which couple with the vibrational modes of molecules in their close proximity.[80] This coupling is at the heart of the dramatic enhancement of the characteristic signal of the molecules, making possible its specific and ultrasensitive detection. Nowadays, EM enhancement factors as high as 10^{10}-10^{11} with respect to normal Raman scattering have been reported in the literature.[70]

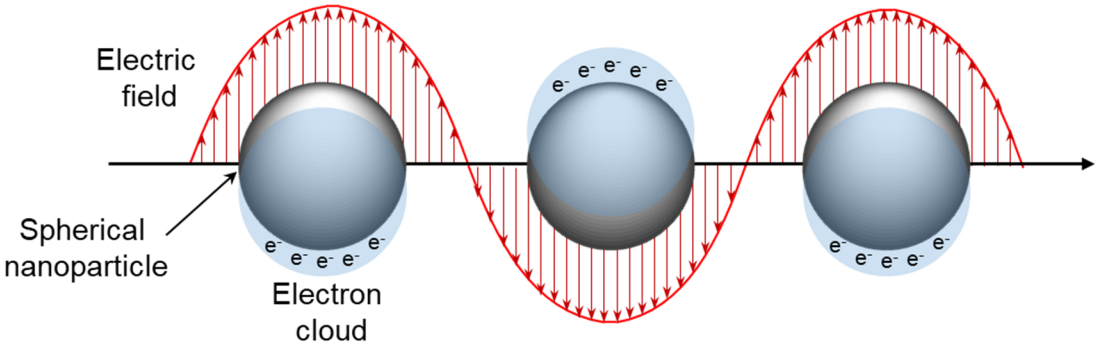

Figure 1. 20. Scheme of induction of LSPRs in spherical nanoparticles. The oscillating electric field triggers a coherent motion of conduction electrons generating a dipole along one axis of symmetry in anisotropic spherical particles.

Importantly, since the EM enhancement is based on the field enhancement of incident and scattered fields due to the LSPR excitation, molecules must be adsorbed or extremely close to the metallic surface (within ca.10 nm) in order to observe SERS.

1.8.5.1 Properties of the electromagnetic (EM) enhancement

In simple terms, the EM enhancement mechanism can be described for metallic spherical nanoparticles, smaller than the incident wavelength of light.[81] When the incident light beam enters in resonance with the surface plasmon, the spherical metallic nanoparticle emits a dipolar field (E_{SP}). The magnitude of this E_{SP} radiated by the sphere to a closely located molecule, depends on the characteristics of the metal substrate (material, size, shape) and dielectric environment. This approach applies to all analyte molecules and can be pictured as in the **Equation 1.6**.

$$E_{SP} = \frac{\varepsilon - \varepsilon_0}{\varepsilon + 2\varepsilon_0} \cdot \left(\frac{r}{r+d}\right)^3 \cdot E_0 \qquad (1.6)$$

Where, ε and ε_0 are the dielectric constants of the metal (a wavelength dependent function, ε(ω)) and the surrounding medium respectively, *r* the spherical nanoparticle radius, *d* the molecule-metal surface distance, and E_0 the incident field strength. The magnitude of the E_{SP} is larger when the denominator $\varepsilon+2\varepsilon_0$ is very small (i.e., under plasmon resonance conditions). For metals, this condition can be approximately met at the incident wavelength ω_R for which the real part of metal dielectric constant $Re(\varepsilon(\omega_R))$ is ca. equal to $-2\varepsilon_0$ and, simultaneously, the imaginary part $Im(\varepsilon(\omega_R))$ is very small.

Subsequently, the magnitude of the field enhancement factor sensed by molecule, $A(\nu)$, can be expressed as the ratio between the enhanced local field at the molecule ($E_M = E_0+E_{SP}$) and the incident field E_0 in **Equation 1.7**.

$$A(\nu) = \frac{E_M(\nu)}{E_0\,(\nu)} \approx \frac{\varepsilon-\varepsilon_0}{\varepsilon+2\varepsilon_0} \cdot \left(\frac{r}{r+d}\right)^3 \tag{1.7}$$

Finally, the EM SERS enhancement factor (G_{SERS}^{EM}, **Equation 1.8**) for Stokes scattering can be determined as the enhancement factor product of the incident and Raman-scattered fields $A(\nu_L)$ and $A(\nu_S)$. From the equation it is important to note that the field enhancement factor rapidly decreases by a factor of ca. $(1/ r + d)^{12}$, when the distance between the molecule and the metal surface of a given radius increases.

$$G_{SERS}^{EM}(\nu_S) = |A(\nu_L)|^2|A(\nu_S)|^2 \approx \left|\frac{\varepsilon(\nu_L)-\varepsilon_0}{\varepsilon(\nu_L)+2\varepsilon_0}\right|^2 \left|\frac{\varepsilon(\nu_S)-\varepsilon_0}{\varepsilon(\nu_S)+2\varepsilon_0}\right|^2 \left(\frac{r}{r+d}\right)^{12} \tag{1.8}$$

Since both, the incident field and the scattering field, are enhanced — and assuming that the field enhancement is roughly the same— the EM enhancement raises approximately with the enhancement factor field to the power of 4 ($|E|^4$). This is the common approximation for the zero-Stokes shift (**Equation 1.9**).

$$EF(\nu_L) \approx \frac{|E_{Loc}(\nu_L)|^4}{|E_{Inc}|^4} \tag{1.9}$$

Where, E_{Loc} (ν_L) and E_{Inc} are the local field at the analyte molecule and incident field on the metallic surface of the sphere.

From the practical point of view, most applications are focused on acquiring averaged signals from a large number of molecules adsorbed at the metallic surfaces (i.e., average-SERS response). Experimentally, it is difficult to determine the local field enhancement at a given position on the surface as shown in the previous equations. Instead, it is more useful to calculate the average SERS EF for a given substrate (SSEF) as shown in **Equation 1.10**.

$$SSEF = \frac{I_{SERS}/N_{Surf}}{I_{RS}/N_{Vol}} \quad (1.10)$$

Where N_{Surf} is the average number of molecules in the scattering volume, N_{Vol} the average number of molecules in the same scattering volume, I_{RS} the Raman intensity for N_{Vol} and I_{SERS} the SERS intensity for N_{Surf} in a sub-monolayer range.

1.8.5.2 The chemical enhancement (CE) mechanism

An additional contribution to the overall SERS enhancement can be provided by the so-called CE enhancement effect. In general, the CE enhancement involves a change in polarizability of molecules directly coordinated on a metallic surface (**Figure 1.19**). The formation of this new surface complex can enable charge transfer events between the metal and the molecule in a similar fashion as traditional resonant Raman mechanisms, where new electronic states within the system appear, which serve as resonant intermediates in the scattering process.[82] Typically, the CE enhancement effect contributes to the signal enhancement to a far lesser extent than the EM mechanism. Also, differently to the EM enhancement effect, it is an analyte-dependent process.

Before entering into detail about the CE enhancement mechanism, several concepts about metals are briefly described below for better understanding of the process.

- In metals, the energy levels that electrons can occupy are quantized. When atoms gather close together, the energy levels become closely spaced forming bands.

- Metals are composed of two bands, the valence and the conduction band, which most of the times overlap. The valence band is the highest electron occupied energy band, while the conduction band is higher in energy and can be considered as the lowest unfilled energy band.
- In between these bands, the Fermi level is found, and corresponds to the top available energy level for electrons at 0 K. Due to the close disposition of both bands (valence and conduction bands), there are electrons that are not firmly bound to atoms and can move freely. These electrons are called free electrons or conduction electrons.

From this point, the CE enhancement mechanism can be visualized in more detail, where the Fermi level of the metal has a symmetric disposition respect to the highest and lowest occupied molecular orbitals of the molecule, HOMO and LUMO (**Figure 1.21**). Upon light excitation, (1) the electronic transition of the metal-ligand complex can be directly resonant with the laser or (2, 3) charge transfer excitations from the molecule to the metal (from the HOMO molecular orbitals to unoccupied states above the Fermi level) or metal to molecule (from the states just below the Fermi level to the LUMO molecular orbitals) can take place. As a result, this process may enable transitions that can happen at half the energy that would be required for intramolecular excitations of the adsorbed molecule.

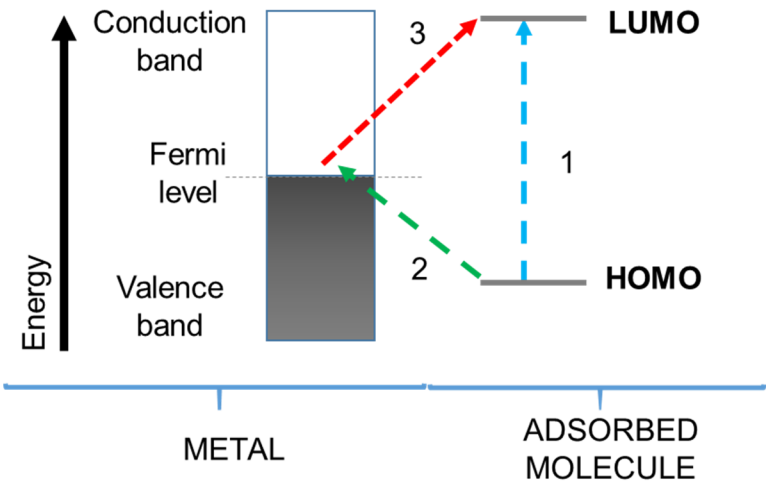

Figure 1. 21. Detailed CE enhancement mechanism of (1) direct electronic resonant transition of the metal-molecule complex and (2, 3) indirect charge transfer process through the metal.

1.8.6 SERS substrates

For many years after its initial discovery, SERS technique largely failed to translate its tremendous analytical potential beyond the spectroscopic community into viable applications. This was mainly ascribed to the lack of nanofabrication methods capable of designing SERS substrates with the required reproducibility, homogeneity and high enhancement factors. However, more recently, spectacular advances in nanofabrication techniques in combination with the ongoing revolution of spectroscopic instrumentation, finally paved the way towards overcoming such previous limitations, turning SERS into one of the most promising incisive analytical methods for biochemical detection and analysis.[59,83,84]

Good SERS substrates are considered to be those that combine largest amplifications with stable, homogeneous and reproducible responses.[66] Nonetheless, it important to stand out that there are no universal SERS substrates and the selection of the specific features of the substrate are strictly related to the final application.

As a rule of thumb, the higher the EM enhancement, the more localized is the area where such intensification takes place.[85] Thus, for quantitative analyses, SERS substrates are typically tailored to provide lower but relatively uniform and reproducible enhancements (10^5-10^7). In other cases, such as for single/few molecule detection studies, SERS substrates need to be designed to maximize the local enhancements (up to 10^{11}), normally to the detriment of signal uniformity.

In general terms, SERS substrates can be classified in three main groups: colloidal NPs (dispersions of small particles in a continuous phase of different material), planar metallic structures (arrays of NPs sustained on planar supports such as glass) and metallic electrodes. Among these three classes of substrates, NP colloids are the most common materials for SERS, both in early and recent studies.[48]

1.8.6.1 Common synthetic routes for SERS-active colloidal NP solutions

The most common routes of synthesis of anisotropic noble metal colloids involve bottom-up approaches based on the wet-chemical synthesis of particles at the atomic or molecular scale.[86-88] The possible size range of the so-synthetized particles can vary from tens of nanometers up to 500 nm. The fabrication of these colloids through chemical reactions involve two main parts: reduction and stabilization. While the choice of the strength of the reducing agent is important, the selection of the stabilizer is critical. This stabilization is achieved via steric or electrostatic repulsions where the most used stabilizing agents are surfactants, thiolated and aliphatic molecules, biomolecules, and polymers.[89] On the other hand, typical reducing agents are sodium citrate, borohydrides, hydroxylamine, polyols, citric and oxalic acids, hydrogen or hydrazine, among others. In some syntheses only a single molecule acts as the reducing and stabilizing agent.

In general, the resultant colloids obtained via these bottom-up methods are negatively or positively charged due to the adsorption of negatively/positively charged ions on their surface.[90] In the case of negatively charged NPs, the most widespread methods of synthesis of Au and Ag NPs involve the well-known Lee-Meisel and Turkevich methods.[88,91] Notably, the Turkevich method has been further improved by other research groups.[86,92-96] In both cases, the NPs are obtained via chemical reduction reaction in aqueous solution of a Au or Ag salt.

In the case of positively charged NPs, alkylamines (such as spermine tetrahydrochloride), surfactants (e.g. hexadecyltrimethylammoniumbromide, CTAB) or polymers (poly-L-Lysine (PLL) and polyethyleneimine (PEI) among others) have been employed to confer a positive charge to either Au or Ag NPs. In some cases, the amine-containing molecules play a double role as reducing/stabilizing agent. While in others, an additional reducing agent is necessary to reduce the metal salt.

1.8.6.2 Colloidal stability: The DLVO theory

In general, colloidal solutions are not thermodynamically stable with respect to the bulk dispersant.[97] As a consequence, NPs tend to agglomerate and form

aggregates of increasing size, which eventually sediment by gravity. This aggregation behavior can be thermodynamically reflected in the surface tension equation (**Equation 1.11**), which is defined by the reversible work necessary to increase the surface of a liquid by a unit area.

$$dw = \gamma \mathrm{dA} \tag{1.11}$$

Where γ is the surface tension (or surface energy), *w* the reversible work and A the area.

At constant temperature, composition and pressure, the term γdA can be considered to be equal to dG (the Gibbs free energy). For a process to be spontaneous dG should be smaller than zero (dG<0). Therefore, if dA<0 the system will tend to decrease the interface area and the surface tension, forming large aggregates and ultimately a phase separation.

Importantly, these thermodynamically unstable NPs can be kinetically protected against aggregation/coagulation (formation of a compact network of particles) or flocculation (formation of a loose network of particles or flocs) by stabilizing agents. Usually, the formation of flocs may be reversed while the formation of aggregates is irreversible. The stabilization of NPs can be carried out via two different approaches: sterically and electrostatically (**Figure 1.22**). In this way, the existing attraction between particles can be screened.

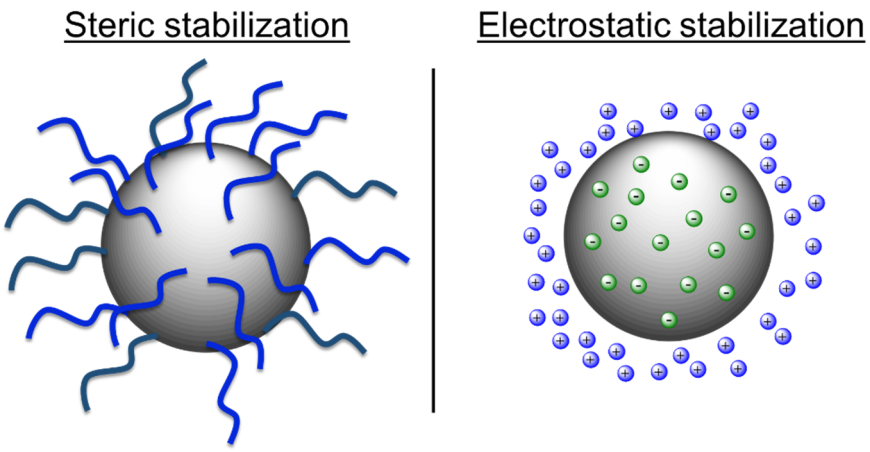

Figure 1. 22. Illustration summarizing the main protocols of NP stabilization (steric and electrostatic stabilization).

The electrostatic stabilization depends on the balance between attraction van der Waals forces and repulsive Coulomb forces that exist when particles get close to one another as a result of Brownian motion. If there is mutual repulsion between particles, the NP solution will remain stable. Conversely, if there are null or minor repulsive forces, the particles will eventually get close enough to result in the aggregation of the system.

On the other hand, the steric stabilization relies on the protective action of large layers of adsorbed molecules on the particle surfaces, such as polymers. In this case, work is necessary to force the NP close together because the large chains of adsorbed molecules form a physical barrier that prevents aggregation. In addition, charged polymers such as polyelectrolytes protect the NPs electrostatically and sterically against aggregation.

The stability of colloidal solutions, in which particles are electrostatically stabilized, is classically explained by the DLVO theory, described by Derjaguin, Landau, Verwey, and Overbeek in 1940s. The DLVO theory suggests that the conditions of colloidal stability/instability of NPs can be quantitatively established by an energy-distance curve, which combines van der Waals attraction and double-layer repulsion forces.[98]

Electric potential near a particle surface and the double layer repulsion

The ions adsorbed on the surface of colloids (referred as co-ions) determine the surface charge. In a solution, co-ions and counter ions (ions with opposite charge) exist and are unevenly distributed in close vicinity to the particle surface. This distribution depends on Coulombic forces, entropic forces and the Brownian motion. The concentration of counter ions is always the highest in the proximity of the particle surface, whereas the concentration of co-ions have the opposite trend. Such distribution determines the commonly known double layer structure, which comprises two layers: the Stern layer and the diffuse (Gouy) layer separated by the Helmholtz plane (**Figure 1.23**). The first inner layer, where solvent and counter ions are firmly bound is called the Stern layer and is about 0.5 nm thick. In the case for example of positively-charged particle surfaces in an aqueous solution, the Stern layer would contain intensely polarized water molecules and desolvated ions firmly bound onto the surface. This layer always

travels with an outer (diffuse) layer of ions, which are less firmly bound, as the NP diffuse through the colloidal solution. It is in this region where counter ions reach average concentration in the solvent. The electric potential at the interfacial double layer is known as ζ potential, which is in turn indirectly related to the charge at the nanoparticle surface.[99]

In general, the electric potential (E) for a flat surface drops linearly through the Stern layer until the Helmotz plane. Beyond this plane, the electric potential in the diffuse layer drops approximately following the trend shown in **Equation 1.12**.

$$E \propto \mathrm{e}^{-\kappa(x)} \tag{1.12}$$

Where E is the electric potential, x is the distance and 1/κ is the Debye-Hückel screening strength, normally used to describe the double layer thickness (**Equation 1.13**). Being κ:

$$\kappa = \sqrt{\frac{2F^2 C_i Z_i^2}{\varepsilon_r \varepsilon_0 RT}} \tag{1.13}$$

Where F is the Faraday constant, C_i the concentration of ions of type i, Z_i the valence of ions of type i, ε_0 the permittivity of the vacuum and ε_r the dielectric constant of the solvent.

Equation 1.12 and **1.13** shows that E decreases in close vicinity to the flat solid surface with increasing concentration and valence of counterions. On the other hand, E increases when the dielectric constant of the solvent is increased. Thus, high concentrations and valence of counter ions would result in the reduced thickness of both layers.

The same approximation can be done for spherical nanoparticles dispersed in an electrolyte solution (**Equation 1.14**).

$$E = E_0 \frac{r}{a} \mathrm{e}^{-\kappa(a-r)} \tag{1.14}$$

Where E_0 is the surface potential, r the radius of the sphere and a the distance from the center of the sphere. This approximation is valid for NPs

separated by a large distance, where the charge distribution is not influenced by other NPs. In this case, there is no overlap between the double layers of the NPs and the electrostatic repulsion is zero.

As NPs approach one another, mutual electrostatic repulsion arises and their double layers overlap. Then, the electrostatic repulsion for two NPs of the same size can be expressed as in **Equation 1.15**.

$$V_R = 2\pi\varepsilon_r\varepsilon_0 r E^2 e^{-\kappa S} \quad (1.15)$$

Where V_R is the electrostatic repulsion, r the NP radius and S the surface-to-surface separation distance between the NPs.

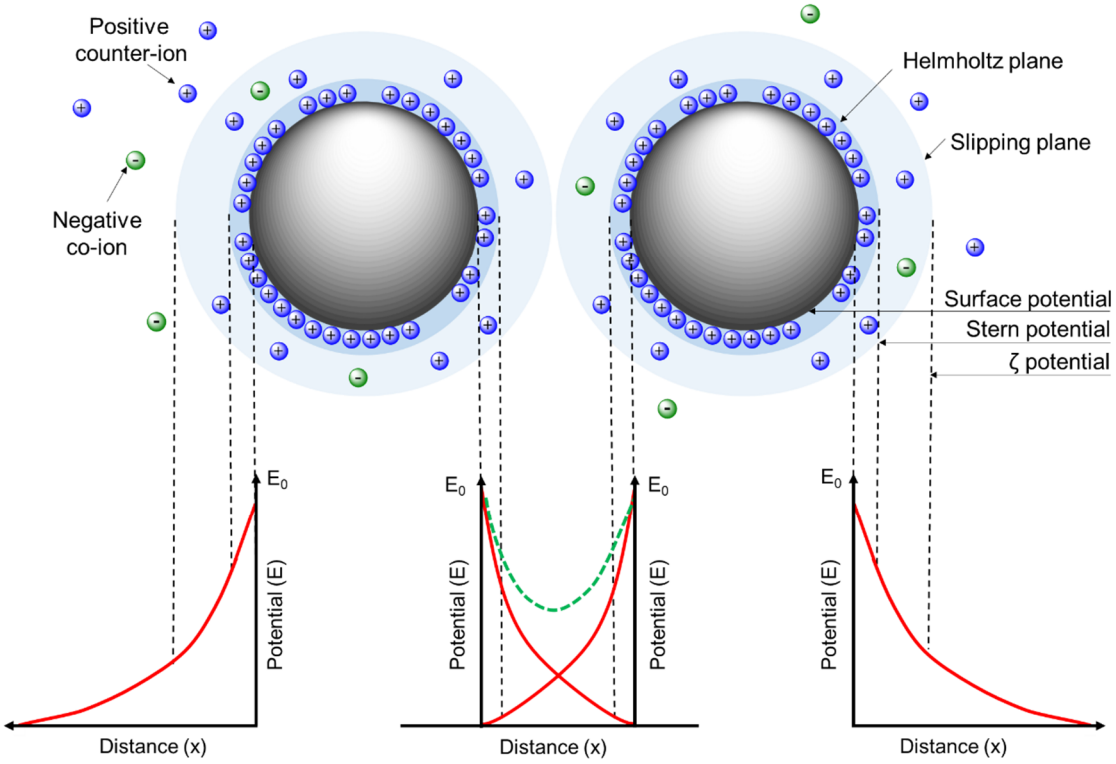

Figure 1. 23. Model showing the trend of the electric potential (E) as a function of the NP surface distance for two approaching negatively charged NPs. The electric double layer surrounding the NPs and the distribution of co-ions and counterions are also shown. E_0 represents the potential at the surface.

Van der Waals attraction potential

Van der Waals attractive forces have also an important role for particles dispersed in a solvent in continuous Brownian motion. These attractive forces are usually weak but become important at short distances. In addition, van der Waals

forces are present for any kind of molecules, charged or neutral, as well as for NPs dispersed in a solution. The van der Waals forces between two molecules onto two spherical NPs of radius r, and separated by an interparticle distance S can be integrated as shown in **Equation 1.16**. The negative charge indicates the attraction nature of the interaction between two NPs of equal sizes.

$$\mathrm{V}_A = -\frac{A}{6}\left\{\frac{2r^2}{S^2+4rS} + \frac{2r^2}{S^2+4rS+4r^2} + ln\left(\frac{S^2+4rS}{S^2+4rS+4r^2}\right)\right\} \qquad (1.16)$$

Where A is the Hamaker constant, a positive constant which depends on the polarizability of the molecules (onto the two particle surfaces) and in the solution separating them.

When the interparticle separation is significantly smaller than the NP radius (S/r<<1), the van der Waals attraction potential between NPs can be approximated as:

$$\mathrm{V}_A = -\frac{Ar}{12S} \qquad (1.17)$$

Total potential energy of interaction between two particles: the DLVO theory

In the DLVO theory, the total energy of interaction (V) between two approaching spherical NPs is considered as the combination of the electrostatic repulsion potential (V_R) and the van der Waals attraction potential (V_A). This relationship is summarized in **Equation 1.18**.

$$\mathrm{V} = \mathrm{V}_R + \mathrm{V}_A = 2\pi\varepsilon_r\varepsilon_0 r E^2 \mathrm{e}^{-\kappa S} - \frac{Ar}{12S} \qquad (1.18)$$

Figure 1.24 shows graphically the Coulombic repulsion potential, the van der Waals attraction potential and the combination of the two of them as a function of distance from the NP surface. At first, it can be noticed that at distances far from the NP surface, the potential energy of attractive and repulsive forces drops to almost zero. While the decay of the repulsion potential is approximately exponential, the van der Waals attraction potential drops as a function of the inverse power of interparticle separation. Near the NP surface there is a deep minimum, known as the primary minimum, which is mainly determined by the van

der Waals attraction potential. At intermediate distances, the repulsion potential dominates over the van der Waals attraction potential resulting in an energy maximum. The height of this maximum, normally referred as repulsive barrier, depends on the surface (Stern or ζ potential) and electrolyte valence and concentration.[98] In this case, the NP stability is conditioned by the fact that the energy maximum in the repulsive barrier has to be larger than the thermal energy of the NPs (given by 10 kT, where k is the Boltzman constant). In this way, the collisions between NPs as a result of the Brownian motion will not lead to agglomeration because the repulsive barrier will not be overcome. In some cases, when the concentration of counter ions is high enough, a secondary minimum is present and NPs may tend to attach to each other resulting in flocculation of the system. This flocculation however, can be simply reversed by sonication or mixing for example.

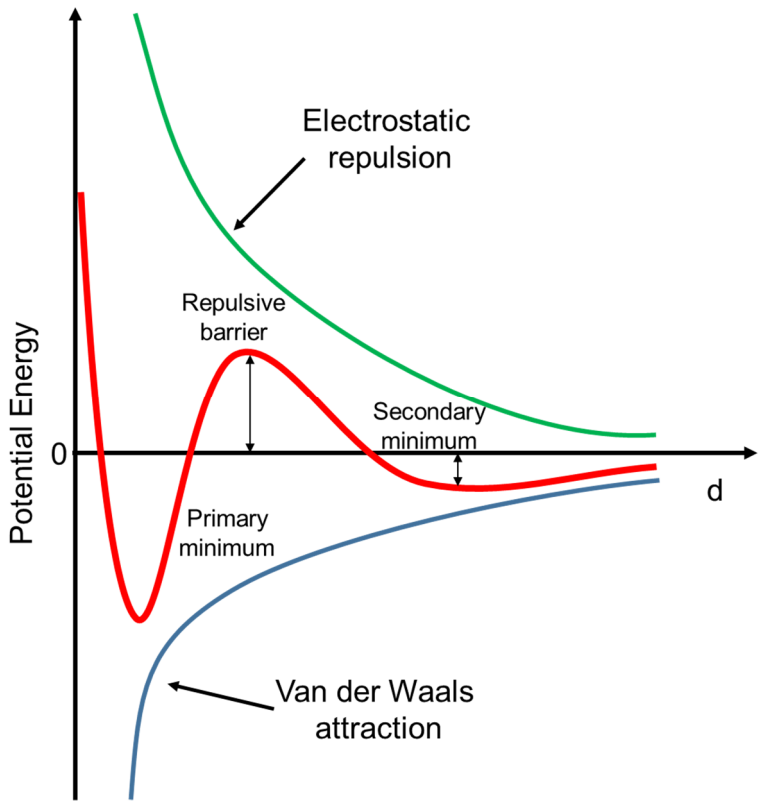

Figure 1. 24. Diagram of the total DLVO potential energy of interaction (red line) as a sum of van der Waals attraction potential (blue line) and repulsive potential (green line).

Importantly, since the electrical potential depends on the valence and concentration of counter ions (as shown in **Equation 1.12** and **1.13**), increasing the electrolyte concentration will lead to a compression of the double layer and

the repulsive barrier will gradually decrease. If the barrier disappears, the net interaction will be solely attractive and the NPs will coagulate. For a given electrolyte concentration, the barrier will decrease with increasing the valence of the electrolyte. For this reason, NPs are poorly stable in the presence of multivalent ions.

The DLVO theory is based in several assumptions such as: the surface of the NPs is infinitely flat, there is an even surface charge density, constant surface electric potential and no chemical reactions between NPs and solvent are considered (the solvent only influences through the dielectric constant).[100] Despite these assumptions, the DLVO theory is valid in many cases and has been widely accepted and applied.

1.8.6.3 SERS signal dependence on the SERS substrate properties

To date, noble metal nanoparticles, especially Au and Ag NPs, are one of the most widespread SERS-active substrates due to their simplicity in preparation and tunable surface plasmon resonance (SPR) properties. Optically, Au and Ag can sustain plasmon resonances in the visible/NIR spectral window (~400-1000 nm), the most interesting spectral range for SERS.[48] Additionally, Au and Ag are air stable materials, differently to other metals such as Cu and Al which also present plasmon resonances in the same spectral range. For this reason, Au and Ag are by far the most employed materials for SERS applications.[101]

It is important to note that the SPR properties of the substrate directly affect the overall SERS signal enhancement and are ultimately dictated by their composition, size, shape and dielectric environment.[102] In consequence, these factors can be tuned according to the final application and must be considered for the optimal design of the SERS substrate:

- Nanoparticle composition. The NP composition is one of the key factors affecting the final SERS signal amplification. When comparing similar nanostructures Ag is generally considered a much more efficient optical material than Au (Ag offers from 10 to 100 fold greater EFs than Au).[103] Additionally, Ag embraces a wider wavelength range of the visible and near-IR spectrum (~ 400-1000 nm) as compared to Au (~ 600-1250 nm).

Below 600 nm, most of the incident light is absorbed by Au NPs which results in the dumping of SPRs. Despite this, Au NPs are more biocompatible and display chemical stability over longer periods of time under ambient conditions. Therefore, they are typically preferred for in vivo applications.

- Nanoparticle size. As a rule of thumb, the SERS signal increases with the NP size. However, an optimal range for the effective amplification exist. Too small NPs (smaller than 5 nm) are not capable of supporting plasmon resonances because the scattering of the conduction electrons on the surface becomes dominant and thus, the energy is lost through scattering.[104] On the other hand, too large NPs (approaching the incident excitation wavelength), are affected by radiative dumping effects, where non-radiative modes are preferentially excited.[105,106]
- Nanoparticle morphology. Nanoparticle morphology is by far the most efficient parameter to be used for manipulating the plasmon response of the nanomaterials. Further, NPs with asymmetric features have been observed to display highly focalized electromagnetic fields in sharp edges and corners. Such concentration of the EM field in specific regions within the particle (also known as hot spots), may give rise to higher orders of enhancement for NPs of similar size and composition. In this regard, many synthetic protocols have been developed to produce monodispersed NPs with a wide range of geometries such as spheres, cubes, rods, triangles, plates, wires etc.[107,108]

Some examples of anisotropic noble metal NPs and their respective optical responses are illustrated in **Figure 1.25**. In the first case (**Figure 1.25A**), the extinction spectra of AgCit and AuCit nanospheres of 70 nm reveal a single LSPR band, as a result of the dipole resonance excitation (**Figure 1.20**). When the simple geometry of the sphere is remodeled into other morphologies such as the cubic shape, the oscillation of the electron cloud can take place along different symmetry axes. In consequence, other modes can be excited, as reflected in the extinction spectrum of Ag nanocubes (**Figure 1.25B**).

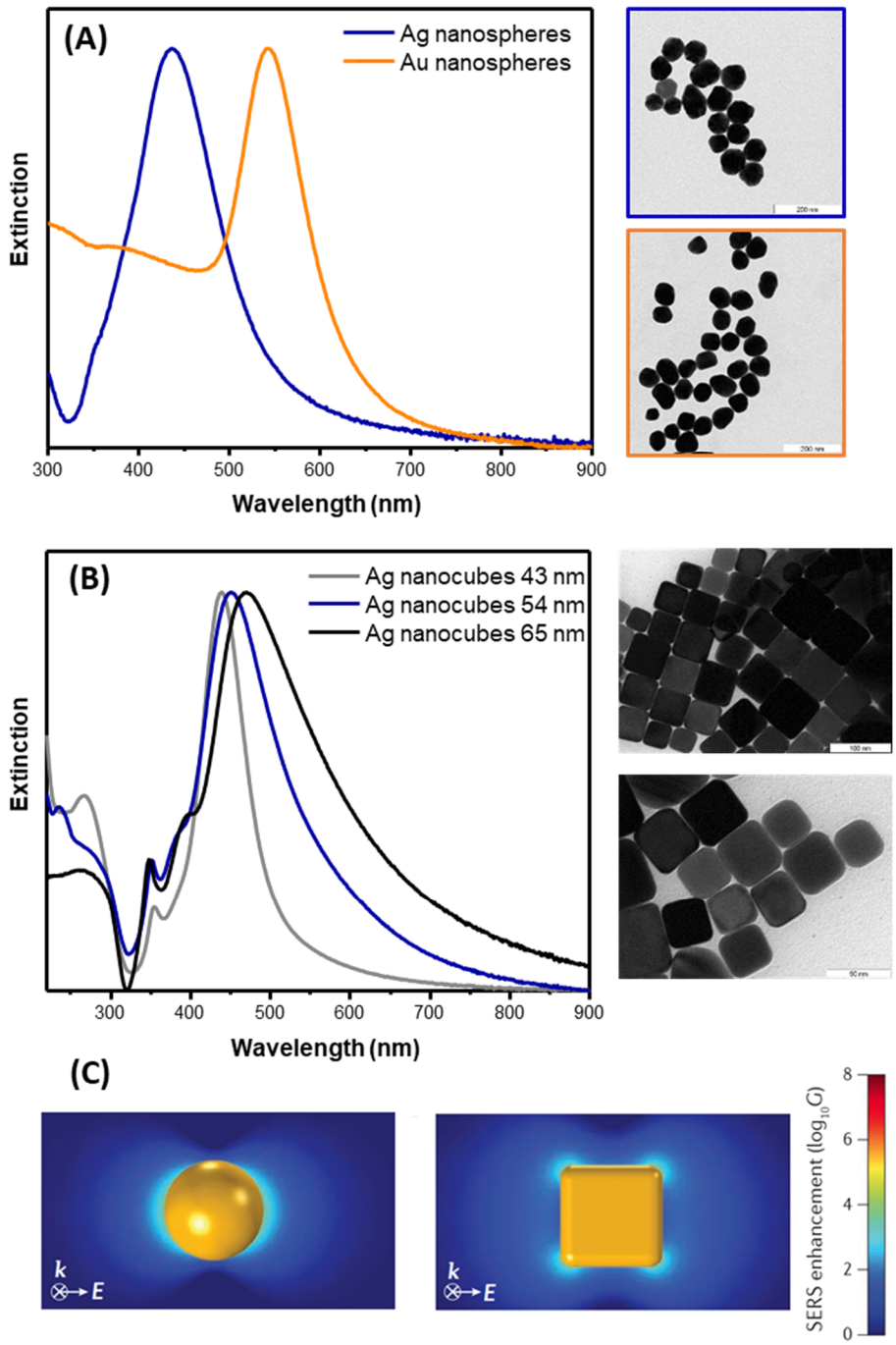

Figure 1. 25. (A) Extinction (absorption+scattering) spectra and TEM images of spherical Ag and Au NPs of 70 nm diameter. (B) Extinction spectra of Ag nanocubes of different sizes and TEM images of dried Ag cubes of 54 nm. (C) Local field contours for spherical and cubic isolated nanoparticles, where G represents the enhancement factor.[109] Reprinted with permission from Ref. 109. Copyright 2016, Nature Reviews Materials.

The spectrum in **Figure 1.25B** shows a dominant dipolar mode at ca. 450 nm and a weaker quadrupole contribution at ca. 350 nm.[110] In addition, the effect of the NP size on the optical response of the substrate is exemplified in **Figure 1.25B**, where the dominant LSPR band of the Ag cubes redshifts as a function of the NP size. Finally, **Figure 1.25C** shows the concentration of the

electromagnetic field in both spherical and cubic NPs. As can be observed, the concentration of the electromagnetic field is unevenly distributed throughout the entire NP structures and is highly focalized in edges and corners.

1.8.6.4 Plasmon coupling between interacting nanoparticles

While individual isolated nanoparticles do display significant EFs (up to the order of 10^6), much higher EFs~ 10^{11} can be achieved in highly localized regions with intense EM field (hot spots) such as at the interparticle gaps between two or more NPs (**Figure 1.26**). The SERS signal amplification at these junctions is the result of the near-field coupling between the plasmon resonances of the involved NPs.[111]

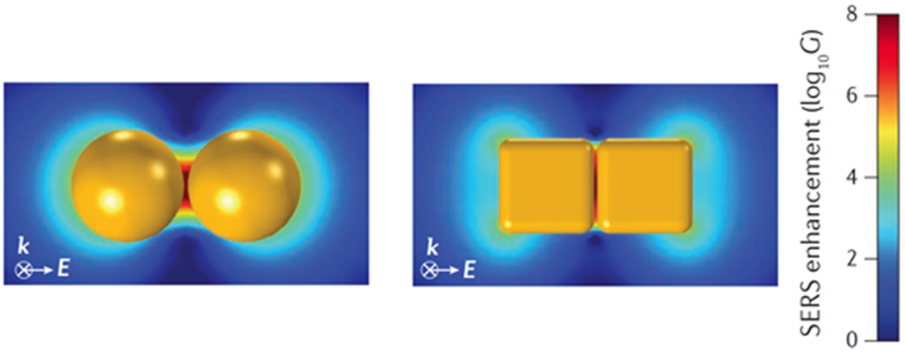

Figure 1. 26. Simulation of the SERS EF distribution for nanosphere and nanocube dimers with incident polarization along the dimer axis.[109] Reprinted with permission from Ref. 109. Copyright 2016, Nature Reviews Materials.

A simple model consisting of a dimer has been generally used to predict the optical response of interacting NPs (**Figure 1.27, 1.28A, 1.28D**). When the polarization of the incident beam is perpendicular with respect to the dimer axis, the coupling between plasmon resonances is almost nonexistent and the optical outcome in the extinction spectrum tends to be that of isolated NPs. On the contrary, when the polarization of the incident beam is aligned along the axis of the dimer (parallel to the z axis, **Figure 1.28A, D**), the coupling between plasmon resonances is maximized (**Figure 1.26**). In the extinction spectrum two modes are expected, an intense red-shifted mode coming from the dipolar coupling of LSPRs and a weak band at lower wavelengths arising from higher order modes (i.e. quadrupole). Note, however, that for Au NP dimers the quadrupole modes are basically unnoticed due to the strong absorption of Au at wavelengths below 600 nm.

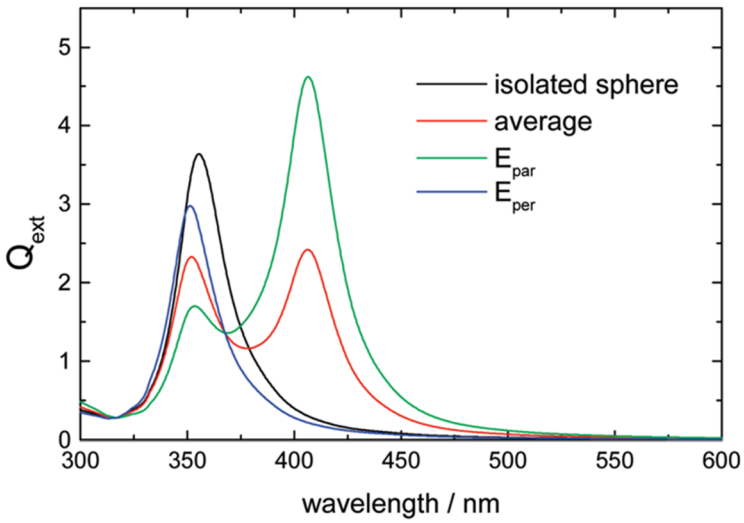

Figure 1. 27. Theoretical extinction coefficient (Q_{ext}) of a Ag dimer, excited with an incident polarization parallel (E_{par}) and perpendicular (E_{per}) to the dimer axis in vacuum.[112] The average extinction spectrum with Epar and Eper polarization is also shown (red line). Reprinted with permission from Ref. 112. Copyright 2010, American Chemical Society.

Mie theory can be used to theoretically explain the main features of gap-plasmon resonances in Au and Ag dimers. The analysis is depicted in **Figure 1.28**.[48] As a global picture, it can be observed that, when isolated spherical NPs approach one another, there is an interparticle distance dependence effect in their optical responses. As a general trend, the shorter the distance between the NPs of the dimer, the higher red-shift of the modes in the extinction spectrum and, in turn, the larger increase of the local SERS enhancements (**Figure 1.28B, C, E and F**). Having this in mind, several conclusions can be extracted:

- The red-shifted modes respect those observed for individual NPs, are the most important in SERS because they broadly determine the intense EM fields at the hot spot.
- The distance in between NPs strongly influences the gap plasmon resonances and local SERS EFs. This interparticle distance dependency, however, affects differently the SERS EFs and the extinction spectrum of the substrate. While a qualitative correlation between the extinction and SERS spectra for individual NPs can be extracted, this fails for highly interacting NPs. This is mainly due to the fact that the overall SERS enhancement is dominated by the resonances located at the hot spot, while the extinction spectrum measures the average response of the plasmonic substrate.[113]

- As a rule of thumb, the higher the SERS EF, the more narrowly localized it becomes. As a result, the gap between the localized SERS EF and the average SERS EF of the dimer increases. This fact directly affects the reproducibility and homogeneity in SERS experiments, because the diffusion/adsorption of molecules only at the hot-spot volume for very shorts gaps may be difficult to control.

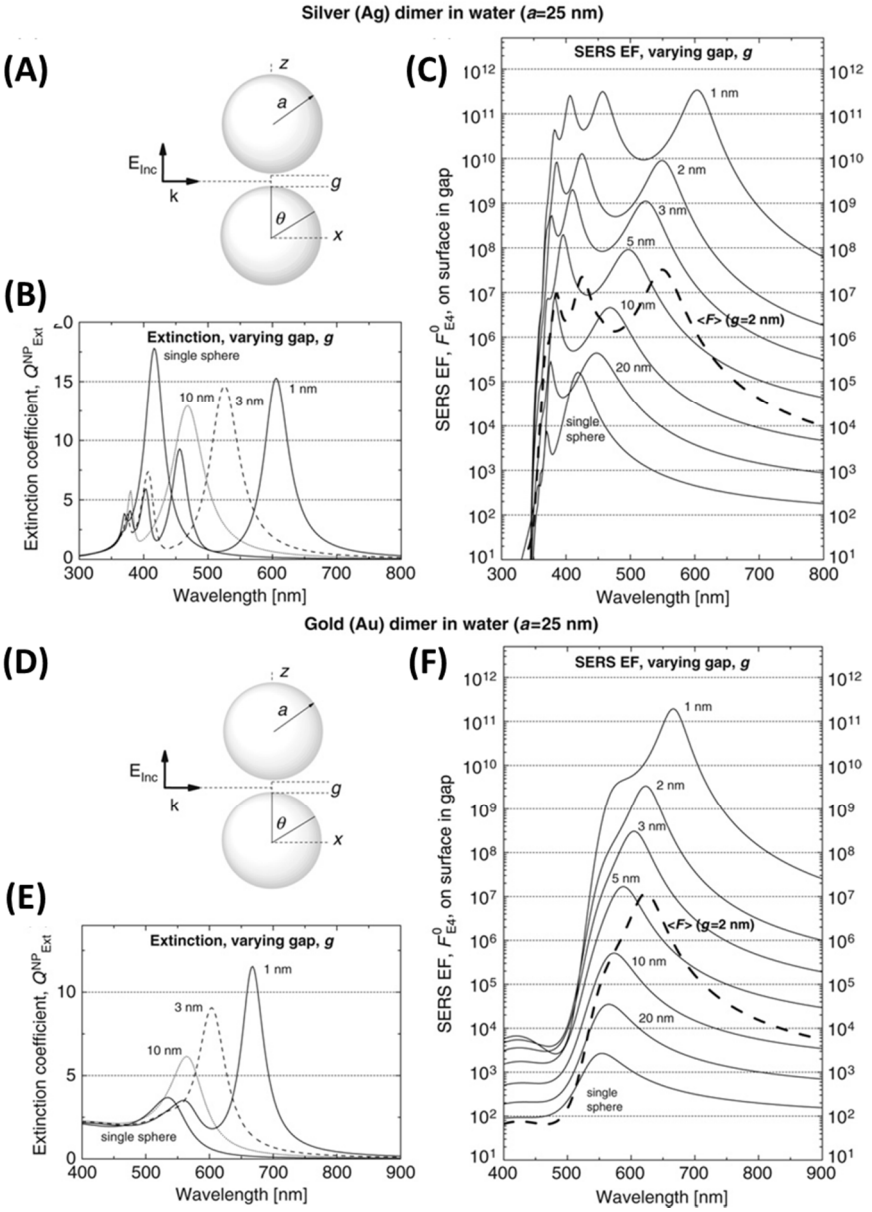

Figure 1. 28. (A,D) Schematic illustration of Ag and Au dimers of equal sizes, excited with an incident polarization along z (maximum coupling of LSPRs) with a wave-vector k along x. (B,E) Theoretical extinction coefficients,Q^{NP}_{Ext}, for Ag and Au dimers respect the incident wavelength, at different interparticle distances.(C,F) Distribution of EF (F^0_{E4}) at different points on the surface allocated at hot spot. Each of the SERS EF distribution spectrum correlates with the theoretical extinction spectrum. The dashed line represents the average SERS EF for a gap distance of 2 nm.[48] Reprinted with permission from Ref. 48. Copyright 2009, Elsevier.

1.8.7 SERS instrumentation

SERS requires the use of intense excitation sources such as lasers to acquire Raman spectra since the Raman effect is a weak process. The wavelengths available for lasers usually span from the visible, near-infrared (NIR) or near ultraviolet (UV) range. In **Figure 1.29** the wavelength ranges of some frequently used lasers are represented.

The choice of the laser ultimately depends on the application, although it is important to take into account that the scattering efficiency increases with the fourth power of the frequency of the excitation light.[114] As a consequence, shorter wavelengths improve the Raman scattering efficiency, but the risk of sample degradation or fluorescence must be considered.

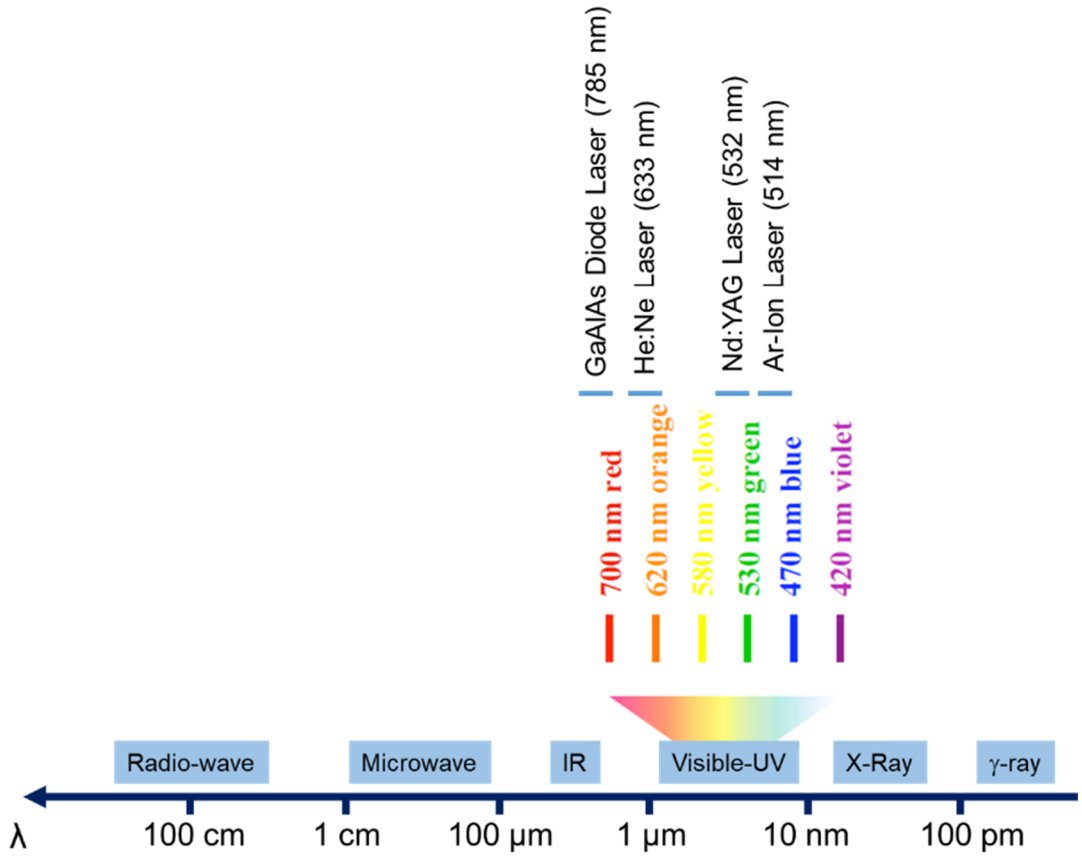

Figure 1. 29. The electromagnetic spectrum and different wavelength ranges of some commercially available lasers.

Figure 1.30 outlines the typical arrangement of a dispersive Raman instrument coupled with a microscope. In this configuration, the incident light from the laser is focused through a pinhole aperture and subsequently delivered to a notch filter, where the light is totally reflected into the microscope. Once the light reaches the sample, the scattering radiation is collected back through the same objective (180º geometry) and passes through the same optics up to the notch filters. In these interference filters, the elastically scattered light is efficiently blocked and the Stokes and anti-Stokes photons pass through the grating system. There, each wavelength is dispersed at different angles and finally reach the CCD (charged-couple device) array detector. As a result, each wavelength focused in each pixel of the array can be calculated and construct a spectrum.

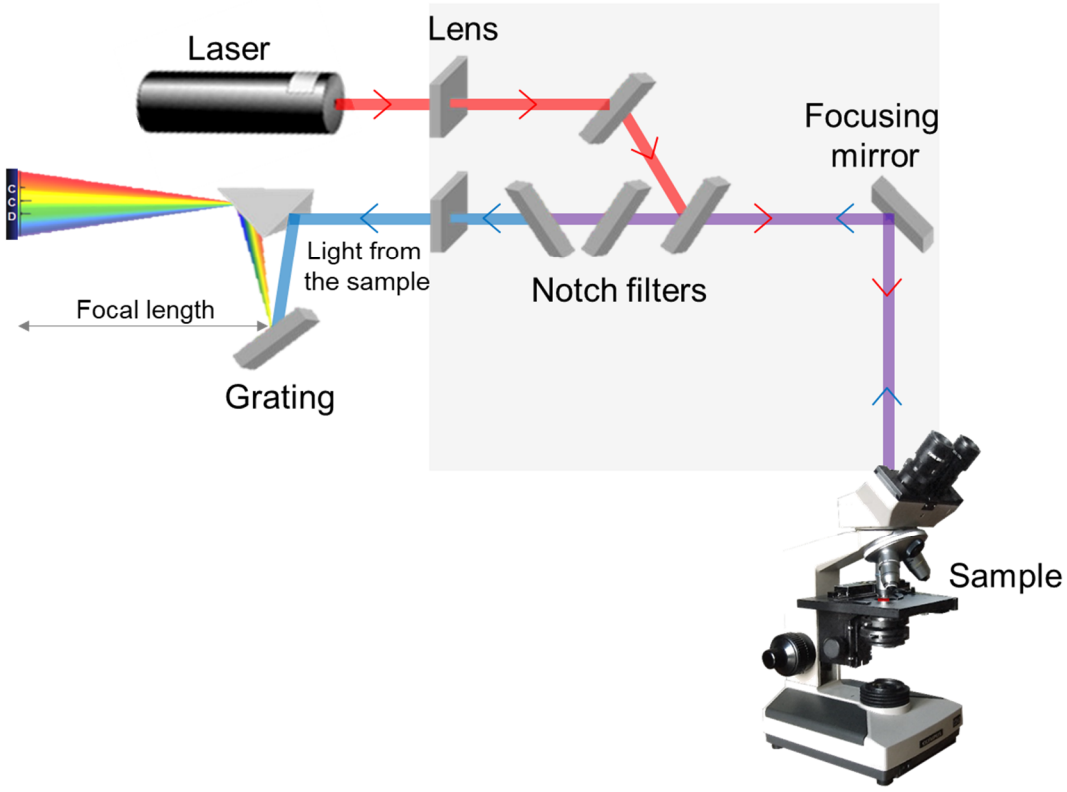

Figure 1. 30. Scheme of a dispersive Raman spectrometer set-up.[80]

1.9. Direct and indirect SERS sensing strategies for DNA analysis

Two different strategies are commonly used for the detection of DNA by SERS: direct and indirect SERS. For direct SERS, the identification and quantification of DNA relies on the acquisition of the intrinsic SERS spectrum of the DNA sequence under study. On the other hand, for indirect approaches the

detection is performed by monitoring the SERS spectrum of a Raman label bound to a nanostructured material which has been devised to indirectly inform about the presence of the target DNA.

1.9.1 Indirect SERS sensing of DNA

To date, the vast majority of the SERS-based detection strategies for DNA rely on the indirect sensing approach, combining a highly SERS active molecule as Raman label (RL) and short ssDNAs bearing a terminal thiol group as capture probes (the thiol group ensures the firm binding of the oligonucleotide onto the enhancing substrate via a covalent bond) onto the plasmonic material.[115,116] As an example, **Figure 1.31** outlines the strategy exploited by Moskovits et al.[115] Here, the target ssDNA is first captured by the complementary DNA strand anchored on a smooth Ag film bearing a fluorescein dye ("RL in the image"). Then, AgNPs carrying also a complementary ssDNA sequence to the target DNA, are selectively self-assembled onto the solid substrate. This complementary interaction drives the formation of hot spots, which efficiently enhance the signal of the RLs leading to target detection down to the ca. 50 nM level.

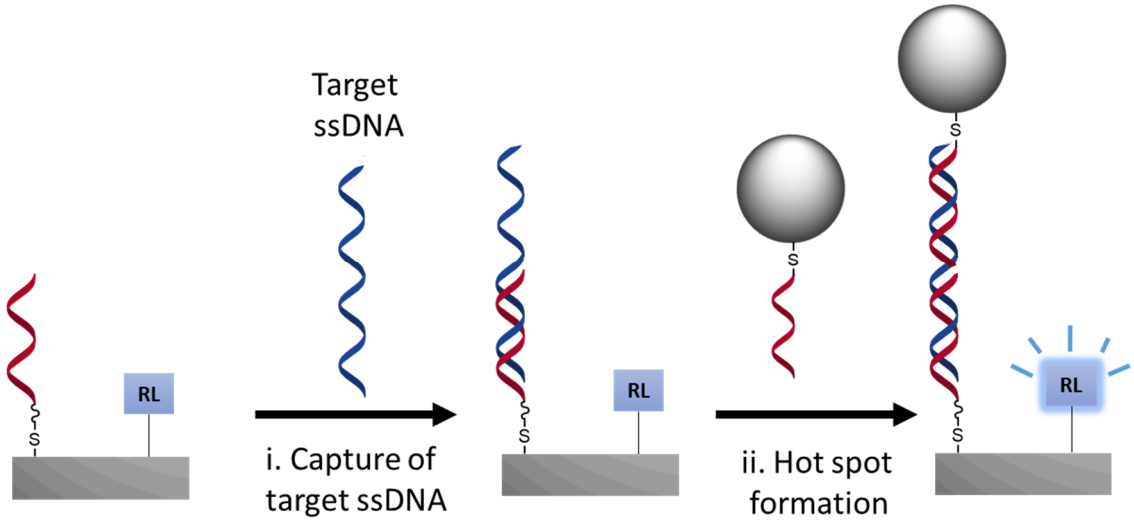

Figure 1. 31. Scheme of an indirect SERS sensing approach for detection of a specific sequence of DNA. RL= Raman label. The NA in blue represents the target ssDNA strand and the NAs in red the complementary ssDNA probes.

This "sandwich hybridization" scheme has been extensively exploited by a wide number research groups. Mirkin and co-workers for example exploited this strategy in a microarray format.[117] This group used functionalized AuNPs with

dye-labeled oligonucleotides as reporter probes. In order to form hot spots, these NPs were added after the target ssDNA was captured by immobilized complementary ssDNA strands. The SERRS signal of the dye was further enhanced by Ag coating reaching 20 fM detection limit. The same group, also reported a similar detection limit (ca. 100 fM), by means of a lithographic technique, creating pairs of Au nanodiscs on Ni wires with edged gaps, in order to obtain SERS signal from dyes conjugated to the assembled DNAs.[118]

Strategies based on the secondary structure of DNA have been also developed. Vo-Dinh and co-workers for example, created different molecular beacon strategies for the detection, among others, of HIV-I and breast cancer genes.[119] To this aim, metallic NPs were functionalized with a hairpin ssDNA sequence. One of the stems of the hairpin was functionalized with a thiol group and the other with a Raman label. Upon hybridization with the target DNA, the hairpin loop opened, which was translated in a change in the SERS signal of the RL. This strategy has been also extended for multiplexed detection using different Raman-active fluorophores.[120]

Overall, the indirect sensing approach can offer high performance and multiplexing capabilities for the detection of DNA. Moreover, when compared to the conventional techniques such as fluorescence, lower limit of detection can be achieved. However, the use of Raman labels or the labeling of strands, increases the cost of the analysis and, more importantly, the rich chemical and structural information contained in the intrinsic SERS spectrum of the targeted DNA under analysis is completely dismissed.

1.9.2 Direct SERS sensing of DNA

The second sensing scheme is a pure label-free method, where direct analysis of DNA is carried out by approximation of the nucleotide to the metallic nanomaterial. This sensing scheme not only offers the possibility to detect the target DNA, but also provides an extra layer of information of the molecule such as hydrogen bonding, hydrophobic (base-stacking) or electrostatic interactions.

Despite the potential of this label-free method, the direct acquisition of the SERS spectrum of DNA has traditionally suffered from limited sensitivity and/or

reproducibility, largely due to the low degree of affinity of DNA towards the nanomaterial or to the scarce control over the final DNA-substrate properties. Many scientific groups have tried to address these issues by improving the degree of affinity of DNA towards the enhancing substrate, developing SERS substrates that provide more homogeneous enhancements or combining SERS with statistical analysis such as partial least-squares (PLS) or principal components analysis (PCA).

Among them, thiolation of ssDNA oligonucleotides as well as thermal annealing strategies have been developed to improve the reproducibility of the label-free SERS assays.[121-123] In these cases however, the adenine modes dominated the SERS spectrum, because adenine is the nucleobase with the highest cross section respect the other naturally occurring bases. Halas et al. for example, used the overwhelming ring breathing band of adenine at 736 cm^{-1} as spectral marker to detect the target ssDNA.[121] To this aim, thiolated ssDNAs immobilized on Au nanoshell surfaces were used as capture probes. Importantly, the adenine nucleobases of the probe were replaced by 2-aminopurine. In this way, any adenine containing complementary target could be detected by SERS, because it showed a different vibrational pattern in the SERS spectrum respect the probe spectrum.

On the other hand, the SERS signal of dried unmodified nucleic acids on Ag nanorods have been also analyzed by SERS in combination with chemometrics.[124,125] By this approach, nucleic acids are physically deposited close to the enhancing substrate. However, the drying of the samples results in a diverse set of changes of the native structural features, which in turn yields to low spectral reproducibility.

Negatively charged colloids in suspension have been the most extensively used SERS substrates for the label-free detection of DNA. By this method, DNA preferentially adsorbs onto the metallic substrate mostly through the heterocyclic nitrogen or exocyclic amine groups of the nucleobases, being adenine the nucleobase with highest cross-section and affinity to the metallic surface.[126] This preferential binding largely hampers the detection of DNA duplexes, due to the repulsion between the outer phosphate backbone of DNA (negatively charged at

physiological pH) and the negative surface charge of the NPs. The stacked nucleobases are located within the double-helix, therefore limiting their direct adhesion onto the metallic surfaces. Typically, aggregating agents are used in combination with negatively charged AgNPs in the DNA detection as a method promote the formation of hot spots and generate intense SERS signals from the so-formed aggregates.[127-130] $MgSO_4$ is frequently used as aggregating agent because is a "passive" electrolyte that induces nanoparticle coagulation by simply increasing the ionic concentration without firmly adsorbing onto the silver surface. This means that it does not compete with the target molecule for the adsorptive sites. For example, Bell and co-workers[127,129] exploited this approach in combination with hydroxylamine AgNPs (AgHX NPs) to detect single base mismatches in short ssDNAs. Additionally, in combination with the aggregating role of $MgSO_4$, the Mg^{2+} ion has been also exploited to neutralize the surface charge of iodide-modified AgNPs and, thus, enhance the interaction with negatively charged DNA.[130] Other small positively charged molecules have been also used for the same purpose. For instance, Graham and co-workers[131] described the use of spermine molecules as effective neutralizers of the negatively charged phosphate backbone of DNA, which induced the controlled aggregation of the Ag colloids. However, the use of external aggregating agents makes more complex the sensing scheme and, as reported by Torres-Nuñez et al.,[132] the resulting SERS spectra display large dependency on DNA composition and NP surface chemistry. To this end, some strategies based on the use of positively charged NPs have been developed in order to ensure the direct electrostatic interaction between the negatively charged phosphate backbone of DNA and the metallic surface of the NPs with no need of additional external agents. In this regard, surfactants (Cetyl trimethylammonium bromide, CTAB) or polymers (poly-L-Lysine, PLL, or polyethylenimine, PEI) have been employed.[133-135] Efficient electrostatic adhesion of negatively charged analytes can be obtained, although the intrinsic shell thickness of the molecules creates large interparticle gaps reducing the SERS detection capabilities. Additionally, polymers can present high SERS background signals and the stability of DNA can be compromised at high concentrations of surfactants.

In the last years, a novel synthesis of cationic spermine-coated Ag nanoparticles (AgSp NPs), described by D. van Lierop et al.[136], has been used for direct SERS analysis of DNA.[137-141] These NPs contain small spermine molecules electrostatically adsorbed onto the metallic surface, which confer colloidal stability via electrostatic repulsions and an overall positive charge to the NPs. As a result, DNA strands act as electrostatic molecular linkers, promoting the formation of NP clusters which selectively trap DNA at the interparticle junctions.[142,143] This interaction is fast and independent of base composition.[137] As a result, highly stable and SERS active clusters in suspension are formed, where the signal of DNA is maximized into highly efficient electromagnetic hot spots (**Figure 1.32**). In consequence, highly intense and reproducible SERS signals are obtained. Moreover, the addition of aggregating agents is avoided, reducing the number variables to be controlled (i.e., aggregation dynamics, properties of the aggregating agent and so on).

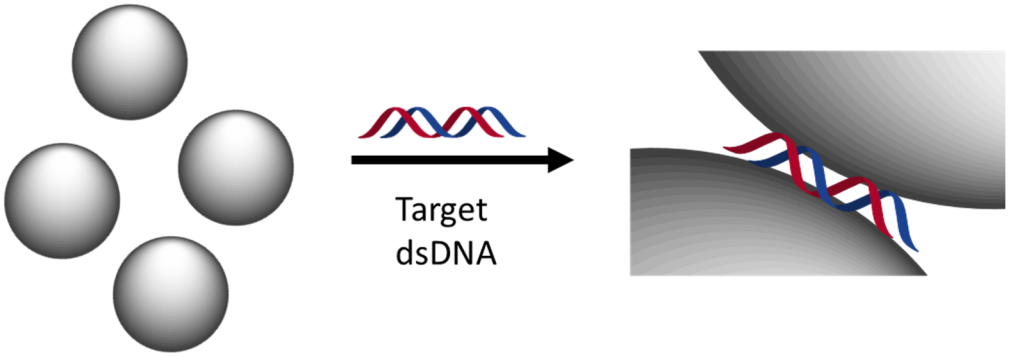

Figure 1. 32. Direct SERS sensing strategy using AgSp NPs as plasmonic substrates to entrap DNA at the interparticle junctions.

1.9.2.1 Direct SERS as a tool to characterize the DNA structural impact upon interaction with nanomaterials

While countless efforts have been devoted to the study of chemically modified oligonucleotides (mostly thiolated DNA) covalently attached to plasmonic nanoparticles,[144-146] the understanding of the mechanisms involved in the non-covalent interaction between native DNA duplexes (dsDNAs), as well as the impact that such interaction has on the double-helix structure, are far less explored and reports in the literature often diverge significantly in their findings.[54,147]

The interaction between unmodified dsDNA and nanoparticles is largely determined by the physicochemical properties of the interface, with the nanoparticle surface charge playing a major role in this process.[148-154] In particular, cationic nanoparticles with sufficiently high surface charge are capable of irreversible interactions with the negatively charged phosphate groups of nucleic acids, leading to DNA damage.[151-153,155-157] Partial denaturation of DNA duplexes upon complexation with positively-charged nanoparticles was previously revealed mainly by direct monitoring the hyperchromic shift of the DNA absorption band at 260 nm[158-160] and indirect examination of the optical (absorbance or fluorescence) response of intercalating dyes sensitive to the structures of the bound DNA (i.e., duplex vs single strand).[159,160] Interestingly, fluorescence studies as well as molecular dynamics (MD) simulations[159] suggested that only high concentrations of nanoparticles can bend and separate DNA strands. This led to the hypothesis that the partial strand separation may only occur via a cooperative action of an ensemble of interacting nanoparticles. However, insertion of intercalating molecules causes itself local structural changes to the duplex, including unzipping of the double helix and lengthening of the strand.[161] Additionally, the near-field interaction of the excited-state fluorophore with the surface plasmon resonances of metallic nanoparticles perturbs the optical properties of the dye and, thus, its fluorescence emission in a way that is largely dependent on the properties of the plasmonic nanoparticles and the fluorophore, as well as the distance between the two.[162] On the other hand, UV-Vis spectroscopy analysis of DNA-NP complexes can be only performed on soluble complexes, thus restricting the case study to very small nanoparticles and/or large DNA/NP molar ratios when phase separation is avoided.[158] To a certain extent, this trend is mirrored in theoretical studies, where the nanoscale size of DNA-NP systems in most cases prevents their direct investigation through atomistic simulations.[163] Thus, in the literature, MD simulations have been carried out only for very small nanoparticles, with diameters not exceeding 1.5 nm, so as to keep the problem computationally manageable.[159,164]

Within this fragmented picture, a plasmon-assisted spectroscopy such as SERS has the potential to be used as a highly informative, ultrasensitive

analytical method for the direct interrogation of nucleic acids/nanoparticles interactions and their impact on the structure of the genetic material.[71,130,138,165-169] Notably, the largest SERS enhancements usually show a high degree of spatial localization, such as those that take place at the interparticle junctions (i.e., hot spots) of highly interacting nanoparticles in colloidal aggregates.[66] Under this scenario, SERS can provide a unique tool to isolate the vibrational signature of those molecules trapped at the nanoparticle junctions.

1.10. References

(1) Watson J., Crick F., *Nature* **1953 Apr 25**, *171 (4356)*, 737.
(2) Franklin, R. E.; Gosling, R. G. *Nature* **1953**, *171*, 740.
(3) H. Lodish, A. B., C. A. Kaiser, M. Krieger, M. P. Scott, A. Bretscher, H. Ploegh, and P. Matsudaira *Molecular Cell Biology*; 6th ed., 2016.
(4) Albert Lehninger, D. L. N., Michael M. Cox *Lehninger Principles of Biochemistry*; 6th ed.; W. H. Freeman, 2012.
(5) Bruce Alberts, A. J., Julian Lewis, David Morgan, Martin Raff, Keith Roberts, Peter Walter *Molecular Biology of the Cell*; 6th ed., 2014.
(6) Devlin, T. M. *Textbook of Biochemistry with Clinical Correlations*, 2004.
(7) Sinden, R. R. *DNA Structure and Function*; Elsevier, 2012.
(8) Yakovchuk, P.; Protozanova, E.; Frank-Kamenetskii, M. D. *Nucleic Acids Research* **2006**, *34*, 564.
(9) Ussery, D. W. In *Enciclopedia of Life Sciences, eLS*; John Wiley & Sons, Ltd: 2001.
(10) Wilkins, M. H. F.; Stokes, A. R.; Wilson, H. R. *Nature* **1953**, *171*, 738.
(11) Russell, P. J. *iGenetics: a molecular approach*; 3rd ed., 2010.
(12) DiMaio, F.; Yu, X.; Rensen, E.; Krupovic, M.; Prangishvili, D.; Egelman, E. H. *Science* **2015**, *348*, 914.
(13) Whelan, D. R.; Hiscox, T. J.; Rood, J. I.; Bambery, K. R.; McNaughton, D.; Wood, B. R. *Journal of the Royal Society Interface* **2014**, *11*, 20140454.
(14) Wang, A. H. J.; Quigley, G. J.; Kolpak, F. J.; Crawford, J. L.; van Boom, J. H.; van der Marel, G.; Rich, A. *Nature* **1979**, *282*, 680.
(15) Marincs, F.; White, D. W. R. *FEBS Letters* **1996**, *382*, 1.
(16) Ray, B. K.; Dhar, S.; Shakya, A.; Ray, A. *Proceedings of the National Academy of Sciences* **2011**, *108*, 103.
(17) Victor A. Bloomfield, D. M. C., Ignacio Tinoco, John E. Hearst, David E. Wemmer, Peter A. Killman , Douglas H. Turner *Nucleic Acids: Structures, Properties, and Functions*; 1st Edition ed.; University Science Books, 2000.
(18) NatureEducation2014, https://www.nature.com/scitable/topicpage/eukaryotes.
(19) Meselson, M.; Stahl, F. W. *Proceedings of the National Academy of Sciences* **1958**, *44*, 671.
(20) OpenStaxCNX, https://cnx.org/contents/FPtK1zmh@6.17:9TxHOD3O@4/The.
(21) Nicolle Rager,N., https://www.nsf.gov/news/overviews/biology/interactive.jsp
(22) Carlin, J. L. *Nature Education* **2011**, Knowledge 3(10):10.
(23) Freese, E. *Proceedings of the National Academy of Sciences of the United States of America* **1959**, *45*, 622.
(24) Carell, T.; Brandmayr, C.; Hienzsch, A.; Muller, M.; Pearson, D.; Reiter, V.; Thoma, I.; Thumbs, P.; Wagner, M. *Angewandte Chemie-International Edition* **2012**, *51*, 7110.
(25) Stolze, B.; Reinhart, S.; Bulllinger, L.; Fröhling, S.; Scholl, C. **2015**, *5*, 8535.
(26) Pylayeva-Gupta Y, G. E., Bar-Sagi D. *Nature reviews Cancer* **2011**, *11*, 761.
(27) Ahearn, I. M.; Haigis, K.; Bar-Sagi, D.; Philips, M. R. *Nat Rev Mol Cell Biol* **2012**, *13*, 39.
(28) Arun Bahadur Gurung, A. B. *Oncology & Hematology Review* **2015**, *11*, 147.

(29) Karnoub, A. E.; Weinberg, R. A. *Nat Rev Mol Cell Biol* **2008**, *9*, 517.
(30) Friday, B. B.; Adjei, A. A. *Biochimica et Biophysica Acta (BBA) - Reviews on Cancer* **2005**, *1756*, 127.
(31) Goitre, L.; Trapani, E.; Trabalzini, L.; Retta, S. F. In *Ras Signaling: Methods and Protocols*; Trabalzini, L., Retta, S. F., Eds.; Humana Press: Totowa, NJ, 2014, p 1.
(32) Berns, A. *Nat Genet* **2008**, *40*, 1149.
(33) Johnson, L.; Mercer, K.; Greenbaum, D.; Bronson, R. T.; Crowley, D.; Tuveson, D. A.; Jacks, T. *Nature* **2001**, *410*, 1111.
(34) Schubbert, S.; Shannon, K.; Bollag, G. *Nat Rev Cancer* **2007**, *7*, 295.
(35) Adrienne D. Cox, S. W. F., Alec C. Kimmelman,Ji Luo & Channing J. Der *Nature Reviews Drug Discovery* **2014**, *13*, 828.
(36) Sauer, M.; Branduardi, P.; Gasser, B.; Valli, M.; Maurer, M.; Porro, D.; Mattanovich, D. *Microb Cell Fact* **2004**, *3*.
(37) George P. Patrinos, W. A., Phillip B. Danielson *Molecular Diagnostics*; 3rd ed., 2016.
(38) Hayashi, K. *PCR Meth. Appl.* **1991**, *1*, 34.
(39) Kusakabe, T.; Maekawa, K.; Ichikawa, A.; Uesugi, M.; Sugiura, Y. *Biochemistry* **1993**, *32*, 11669.
(40) Kakavas, V. K.; Konstantinos, K. V.; Plageras, P.; Panagiotis, P.; Vlachos, T. A.; Antonios, V. T.; Papaioannou, A.; Agelos, P.; Noulas, V. A.; Argiris, N. V. *Mol. Biotechnol.* **2008**, *38*, 155.
(41) Nataraj, A. J.; Olivos-Glander, I.; Kusukawa, N.; Highsmith, W. E. *Electrophoresis* **1999**, *20*, 1177.
(42) Sheffield, V. C.; Beck, J. S.; Kwitek, A. E.; Sandstrom, D. W.; Stone, E. M. *Genomics* **1993**, *16*, 325.
(43) Xiao W, O. P. *Human Mutation* **2001**, *17*, 439.
(44) Taylor, C. F. T. a. G. R. *Methods Mol Med* **2004**, 9.
(45) Costabile, M.; Quach, A.; Ferrante, A. *Human Mutation* **2006**, *27*, 1163.
(46) Jallow, S.; Kaye, S.; Schutten, M.; Brandin, E.; Albert, J.; McConkey, S. J.; Corrah, T.; Whittle, H.; Vanham, G.; Rowland-Jones, S.; Janssens, W. *Journal of Clinical Microbiology* **2007**, *45*, 1565.
(47) Jaluria, P.; Konstantopoulos, K.; Betenbaugh, M.; Shiloach, J. *Microbial Cell Factories* **2007**, *6*, 4.
(48) Etchegoin, E. C. L. R. a. P. G. *Principles of Surface-Enhanced Raman Spectroscopy*; Elsevier: Amsterdam, 2009.
(49) Hondow, H. L.; Fox, S. B.; Mitchell, G.; Scott, R. J.; Beshay, V.; Wong, S. Q.; Dobrovic, A. *BMC Cancer* **2011**, *11*, 265.
(50) Smith, C. J.; Osborn, A. M. *FEMS Microbiology Ecology* **2009**, *67*, 6.
(51) Yang, S.; Rothman, R. E. *The Lancet Infectious Diseases* **2004**, *4*, 337.
(52) Syvanen, A.-C. *Nat Rev Genet* **2001**, *2*, 930.
(53) Mardis, E. R. *Nature* **2011**, *470*, 198.
(54) Samanta, A.; Medintz, I. L. *Nanoscale* **2016**, *8*, 9037.
(55) Tan, S. J.; Campolongo, M. J.; Luo, D.; Cheng, W. L. *Nat. Nanotechnol.* **2011**, *6*, 268.
(56) Clever, G. H.; Shionoya, M. *Coord. Chem. Rev.* **2010**, *254*, 2391.
(57) Jones, M. R.; Seeman, N. C.; Mirkin, C. A. *Science* **2015**, *347*, 12.
(58) Peng, H.-I.; Miller, B. L. *Analyst* **2011**, *136*, 436.
(59) Alvarez-Puebla, R. A.; Liz-Marzan, L. M. *Small* **2010**, *6*, 604.
(60) Smekal, A. *Die Naturwissenschaften* **1923**, *11*, 873.

(61) C. V. Raman, K. S. K. *Nature* **1928**, *121*, 501.
(62) Smith, E.; Dent, G. *Modern Raman Spectroscopy: A Practical Approach*; Blackwell Science Publ: Oxford, 2005.
(63) Ball, D. W. *Spectroscopy* **2001**, *16*, 28.
(64) Long, D. A. *Journal of Raman Spectroscopy* **2004**, *35*, 91.
(65) Matthew Baker, K. A. H., Caryn Hughes *Biophotonics: Vibrational Spectroscopic Diagnostics*; Morgan & Claypool, 2016.
(66) Le Ru, E. C.; Etchegoin, P. G. *Principles of Surface-Enhanced Raman Spectroscopy*; Elsevier, 2009.
(67) C. M. Penney , L. M. G. M. L. *nature physical science* **1972**, *235*, 110.
(68) Alvarez-Puebla, R. A.; Liz-Marzan, L. M. *Chemical Society Reviews* **2012**, *41*, 43.
(69) Alvarez-Puebla, R. A.; Liz-Marzán, L. M. *Angewandte Chemie International Edition* **2012**, *51*, 11214.
(70) Guerrini, L.; Graham, D. *Chemical Society Reviews* **2012**, *41*, 7085.
(71) Schlücker, S. *Angewandte Chemie International Edition* **2014**, *53*, 4756.
(72) Casadio, F.; Leona, M.; Lombardi, J. R.; Van Duyne, R. *Accounts Chem. Res.* **2010**, *43*, 782.
(73) Golightly, R. S.; Doering, W. E.; Natan, M. J. *ACS Nano* **2009**, *3*, 2859.
(74) Fleischmann, M.; Hendra, P. J.; McQuilla.Aj *Chem. Phys. Lett.* **1974**, *26*, 163.
(75) Duyne, D. L. J. a. R. P. V. *J. Electroanal. Chem.* **1977**, *84*, 1.
(76) Albrecht, M. G.; Creighton, J. A. *Journal of the American Chemical Society* **1977**, *99*, 5215.
(77) McCreery, R. L. *Raman Spectroscopy for Chemical Analysis*, 2000.
(78) McNay, G. E., David; Smith, W. Ewen; Faulds, Karen; Graham, Duncan *Appl. Spectrosc.* **2011**, *65*, 825.
(79) El-Sayed, M. A. *Accounts Chem. Res.* **2001**, *34*, 257.
(80) Alvarez-Puebla, R. A. *Journal of Physical Chemistry Letters* **2012**, *3*, 857.
(81) Kneipp, K. M., Martin; Kneipp, Harald (Eds.) *Surface-Enhanced Raman Scattering. Physics and applications*, 2006.
(82) Campion, A.; Kambhampati, P. *Chemical Society Reviews* **1998**, *27*, 241.
(83) Sharma, B.; Frontiera, R. R.; Henry, A. I.; Ringe, E.; Van Duyne, R. P. *Mater. Today* **2012**, *15*, 16.
(84) Darby, B. L.; Le Ru, E. C. *Journal of the American Chemical Society* **2014**, *136*, 10965.
(85) Aroca, R. *Surface-enhanced Vibrational Spectroscopy*; John Wiley & Sons, Chichester, 2006.
(86) Lee, J.-H.; Choi, S. U. S.; Jang, S. P.; Lee, S. Y. *Nanoscale Research Letters* **2012**, *7*, 420.
(87) Merkel, T. J.; Herlihy, K. P.; Nunes, J.; Orgel, R. M.; Rolland, J. P.; DeSimone, J. M. *Langmuir* **2010**, *26*, 13086.
(88) Turkevich, J.; Stevenson, P. C.; Hillier, J. *Discussions of the Faraday Society* **1951**, 55.
(89) Zhao, P. X.; Li, N.; Astruc, D. *Coord. Chem. Rev.* **2013**, *257*, 638.
(90) Tan, S.; Erol, M.; Attygalle, A.; Du, H.; Sukhishvili, S. *Langmuir* **2007**, *23*, 9836.
(91) Lee, P. C.; Meisel, D. *Journal of Physical Chemistry* **1982**, *86*, 3391.
(92) Frens, G. *Nature-Physical Science* **1973**, *241*, 20.

(93) Kimling, J.; Maier, M.; Okenve, B.; Kotaidis, V.; Ballot, H.; Plech, A. *Journal of Physical Chemistry B* **2006**, *110*, 15700.
(94) Polte, J.; Ahner, T. T.; Delissen, F.; Sokolov, S.; Emmerling, F.; Thünemann, A. F.; Kraehnert, R. *Journal of the American Chemical Society* **2010**, *132*, 1296.
(95) Kumar, S.; Gandhi, K. S.; Kumar, R. *Industrial & Engineering Chemistry Research* **2007**, *46*, 3128.
(96) Ji, X.; Song, X.; Li, J.; Bai, Y.; Yang, W.; Peng, X. *Journal of the American Chemical Society* **2007**, *129*, 13939.
(97) Leite, E. R.; Ribeiro, C. In *Crystallization and Growth of Colloidal Nanocrystals*; Springer New York: New York, NY, 2012, p 7.
(98) Tadros, T. In *Colloid Stability*; Wiley-VCH Verlag GmbH & Co. KGaA: 2006, p 1.
(99) https://www.malvern.com/en/products/measurement-type/zeta-potential/?gclid=EAIaIQobChMIpYnD6bPi1wIVZSjTCh0jqARuEAAYASAAEgJX6fD_BwE.
(100) Cao, G. *Nanostructures & Nanomaterials: Synthesis, Properties & Applications*, 2004.
(101) Andrea Cusano, F. J. A., Michele Giordano,Antonello Cutolo *Optochemical Nanosensors*, 2016.
(102) Pazos-Perez, N.; de Abajo, F. J. G.; Fery, A.; Alvarez-Puebla, R. A. *Langmuir* **2012**, *28*, 8909.
(103) Abalde-Cela, S.; Aldeanueva-Potel, P.; Mateo-Mateo, C.; Rodriguez-Lorenzo, L.; Alvarez-Puebla, R. A.; Liz-Marzan, L. M. *Journal of the Royal Society Interface* **2010**, *7*, S435.
(104) Ko, H.; Singamaneni, S.; Tsukruk, V. V. *Small* **2008**, *4*, 1576.
(105) Israelsen, N. D.; Hanson, C.; Vargis, E. *The Scientific World Journal* **2015**, *2015*, 124582.
(106) Moskovits, M. *Journal of Raman Spectroscopy* **2005**, *36*, 485.
(107) Mir-Simon, B.; Reche-Perez, I.; Guerrini, L.; Pazos-Perez, N.; Alvarez-Puebla, R. A. *Chemistry of Materials* **2015**, *27*, 950.
(108) Skrabalak, S. E.; Au, L.; Li, X. D.; Xia, Y. N. *Nature Protocols* **2007**, *2*, 2182.
(109) Ding, S.-Y.; Yi, J.; Li, J.-F.; Ren, B.; Wu, D.-Y.; Panneerselvam, R.; Tian, Z.-Q. *Nature Reviews Materials* **2016**, *1*, 16021.
(110) Edwards, P. R.; Sleith, D.; Wark, A. W.; Martin, R. W. *The Journal of Physical Chemistry C* **2011**, *115*, 14031.
(111) Maher, R. C. In *Raman Spectroscopy for Nanomaterials Characterization*; Kumar, C. S. S. R., Ed.; Springer Berlin Heidelberg: Berlin, Heidelberg, 2012, p 215.
(112) Encina, E. R.; Coronado, E. A. *The Journal of Physical Chemistry C* **2010**, *114*, 3918.
(113) Moskovits, M. *Physical Chemistry Chemical Physics* **2013**, *15*, 5301.
(114) Butler, H. J.; Ashton, L.; Bird, B.; Cinque, G.; Curtis, K.; Dorney, J.; Esmonde-White, K.; Fullwood, N. J.; Gardner, B.; Martin-Hirsch, P. L.; Walsh, M. J.; McAinsh, M. R.; Stone, N.; Martin, F. L. *Nat. Protocols* **2016**, *11*, 664.
(115) Braun, G.; Lee, S. J.; Dante, M.; Nguyen, T.-Q.; Moskovits, M.; Reich, N. *Journal of the American Chemical Society* **2007**, *129*, 6378.

(116) Lin, T.-W.; Wu, H.-Y.; Tasi, T.-T.; Lai, Y.-H.; Shen, H.-H. *Physical Chemistry Chemical Physics* **2015**, *17*, 18443.
(117) Cao, Y. C.; Jin, R.; Mirkin, C. A. *Science* **2002**, *297*, 1536.
(118) Qin, L.; Banholzer, M. J.; Millstone, J. E.; Mirkin, C. A. *Nano Lett.* **2007**, *7*, 3849.
(119) Ngo, H. T., Wang, HN., Fales, A.M. et al. *Anal Bioanal Chem* **2016**, 1773.
(120) Dougan, J. A.; Faulds, K. *Analyst* **2012**, *137*, 545.
(121) Barhoumi, A.; Halas, N. J. *Journal of the American Chemical Society* **2010**, *132*, 12792.
(122) Barhoumi, A.; Zhang, D.; Tam, F.; Halas, N. J. *Journal of the American Chemical Society* **2008**, *130*, 5523.
(123) Barhoumi, A.; Zhang, D.; Halas, N. J. *Journal of the American Chemical Society* **2008**, *130*, 14040.
(124) Abell, J. L.; Garren, J. M.; Driskell, J. D.; Tripp, R. A.; Zhao, Y. *Journal of the American Chemical Society* **2012**, *134*, 12889.
(125) Driskell, J. D.; Seto, A. G.; Jones, L. P.; Jokela, S.; Dluhy, R. A.; Zhao, Y. P.; Tripp, R. A. *Biosensors and Bioelectronics* **2008**, *24*, 917.
(126) Jang, N.-H. *Bulletin of the Korean Chemical Society* **2002**, *23*, 1790.
(127) Papadopoulou, E.; Bell, S. E. J. *Chemistry – A European Journal* **2012**, *18*, 5394.
(128) Prado, E.; Daugey, N.; Plumet, S.; Servant, L.; Lecomte, S. *Chemical Communications* **2011**, *47*, 7425.
(129) Papadopoulou, E.; Bell, S. E. J. *Angewandte Chemie-International Edition* **2011**, *50*, 9058.
(130) Xu, L.-J.; Lei, Z.-C.; Li, J.; Zong, C.; Yang, C. J.; Ren, B. *Journal of the American Chemical Society* **2015**, *137*, 5149.
(131) Graham, D.; Smith, W. E.; Linacre, A. M. T.; Munro, C. H.; Watson, N. D.; White, P. C. *Analytical Chemistry* **1997**, *69*, 4703.
(132) Torres-Nunez, A.; Faulds, K.; Graham, D.; Alvarez-Puebla, R. A.; Guerrini, L. *Analyst* **2016**.
(133) Gill, R.; Lucassen, G. W. *Analytical Methods* **2010**, *2*, 445.
(134) Thomas, M.; Klibanov, A. M. *Proceedings of the National Academy of Sciences* **2003**, *100*, 9138.
(135) Ma, Y.; Guo, Y.; Li, J.; Guan, J.; Xu, L.; Yang, W. *Chemistry – A European Journal* **2009**, *15*, 13135.
(136) van Lierop, D.; Krpetic, Z.; Guerrini, L.; Larmour, I. A.; Dougan, J. A.; Faulds, K.; Graham, D. *Chemical Communications* **2012**, *48*, 8192.
(137) Guerrini, L.; Krpetic, Z.; van Lierop, D.; Alvarez-Puebla, R. A.; Graham, D. *Angewandte Chemie-International Edition* **2015**, *54*, 1144.
(138) Masetti, M.; Xie, H.-n.; Krpetic, Z.; Recanatini, M.; Alvarez-Puebla, R. A.; Guerrini, L. *Journal of the American Chemical Society* **2015**, *137*, 469.
(139) Morla-Folch, J.; Xie, H. N.; Gisbert-Quilis, P.; Gomez-de Pedro, S.; Pazos-Perez, N.; Alvarez-Puebla, R. A.; Guerrini, L. *Angewandte Chemie-International Edition* **2015**, *54*, 13650.
(140) Morla-Folch, J.; Xie, H.-n.; Alvarez-Puebla, R. A.; Guerrini, L. *ACS Nano* **2016**, *10*, 2834.
(141) Gisbert-Quilis, P.; Masetti, M.; Morla-Folch, J.; Fitzgerald, J. M.; Pazos-Perez, N.; Garcia-Rico, E.; Giannini, V.; Alvarez-Puebla, R. A.; Guerrini, L. *Advanced Materials Interfaces* **2017**, *4*, 1700724.
(142) Ayesha Kabir, G. S. K. *PLoS ONE8* **2013**, *7*, e70510.

(143) Deng, H.; Bloomfield, V. A.; Benevides, J. M.; Thomas, G. J. *Nucleic Acids Research* **2000**, *28*, 3379.
(144) Cutler, J. I.; Auyeung, E.; Mirkin, C. A. *J. Am. Chem. Soc.* **2012**, *134*, 1376.
(145) Randeria, P. S.; Jones, M. R.; Kohlstedt, K. L.; Banga, R. J.; Olvera De La Cruz, M.; Schatz, G. C.; Mirkin, C. A. *J. Am. Chem. Soc.* **2015**, *137*, 3486.
(146) Ohta, S.; Glancy, D.; Chan, W. C. W. *Science* **2016**, *351*, 841.
(147) Carnerero, J. M.; Jimenez-Ruiz, A.; Castillo, P. M.; Prado-Gotor, R. *ChemPhysChem* **2017**, *18*, 17.
(148) Kim, S. T.; Saha, K.; Kim, C.; Rotello, V. M. *Acc. Chem. Res.* **2013**, *46*, 681.
(149) Chompoosor, A.; Saha, K.; Ghosh, P. S.; Macarthy, D. J.; Miranda, O. R.; Zhu, Z. J.; Arcaro, K. F.; Rotello, V. M. *Small* **2010**, *6*, 2246.
(150) Handy, R. D.; Von Der Kammer, F.; Lead, J. R.; Hassellöv, M.; Owen, R.; Crane, M. *Ecotoxicology* **2008**, *17*, 287.
(151) Paillusson, F.; Dahirel, V.; Jardat, M.; Victor, J.-M.; Barbi, M. *Phys. Chem. Chem. Phys.* **2011**, *13*, 12603.
(152) Liu, Y.; Li, W.; Lao, F.; Liu, Y.; Wang, L.; Bai, R.; Zhao, Y.; Chen, C. *Biomaterials* **2011**, *32*, 8291.
(153) Han, G.; Martin, C. T.; Rotello, V. M. *Chem. Biol. Drug Des.* **2006**, *67*, 78.
(154) Nash, J. A.; Kwansa, A. L.; Peerless, J. S.; Kim, H. S.; Yingling, Y. G. *Bioconjugate Chem.* **2017**, *28*, 3.
(155) McIntosh, C. M.; Esposito III, E. A.; Boal, A. K.; Simard, J. M.; Martin, C. T.; Rotello, V. M. *J. Am. Chem. Soc.* **2001**, *123*, 7626.
(156) Kang, B.; Mackey, M. A.; El-Sayed, M. A. *J. Am. Chem. Soc.* **2010**, *132*, 1517.
(157) Schaeublin, N. M.; Braydich-Stolle, L. K.; Schrand, A. M.; Miller, J. M.; Hutchison, J.; Schlager, J. J.; Hussain, S. M. *Nanoscale* **2011**, *3*, 410.
(158) Kamata, H.; Zinchenko, A.; Murata, S. *Colloid Polym. Sci.* **2011**, *289*, 1329.
(159) Railsback, J. G.; Singh, A.; Pearce, R. C.; McKnight, T. E.; Collazo, R.; Sitar, Z.; Yingling, Y. G.; Melechko, A. V. *Adv. Mater.* **2012**, *24*, 4261.
(160) Bera, S. C.; Sanyal, K.; Senapati, D.; Mishra, P. P. *The Journal of Physical Chemistry B* **2016**, *120*, 4213.
(161) Ferguson, L. R.; Denny, W. A. *Mutat. Res. Fund. Mol. Mech. Mut.* **2007**, *623*, 14.
(162) Aslan, K.; Gryczynski, I.; Malicka, J.; Matveeva, E.; Lakowicz, J. R.; Geddes, C. D. *Curr. Opin. Biotechnol.* **2005**, *16*, 55.
(163) Chen, S.; Cao, Z.; Jiang, S. *Biomaterials* **2009**, *30*, 5892.
(164) Nash, J. A.; Singh, A.; Li, N. K.; Yingling, Y. G. *ACS Nano* **2015**, *9*, 12374.
(165) Guerrini, L.; Krpetić, Ž.; van Lierop, D.; Alvarez-Puebla, R. A.; Graham, D. *Angew. Chem.-Int. Edit.* **2015**, *54*, 1144.
(166) Panikkanvalappil, S. R.; Hira, S. M.; Mahmoud, M. A.; El-Sayed, M. A. *J. Am. Chem. Soc.* **2014**, *136*, 15961.
(167) Panikkanvalappil, S. R.; Mahmoud, M. A.; Mackey, M. A.; El-Sayed, M. A. *ACS Nano* **2013**, *7*, 7524.
(168) Morla-Folch, J.; Gisbert-Quilis, P.; Masetti, M.; Garcia-Rico, E.; Alvarez-Puebla, R. A.; Guerrini, L. *Angewandte Chemie International Edition* **2017**, *56*, 2381.
(169) Wang, J.; Koo, K.; Wee, E. J. H.; Wang, Y.; Trau, M. *Nanoscale* **2017**.

Chapter 2

Cationic Ag nanoparticles, the sensing platform for direct SERS analysis of DNA

The analysis of genetic information contained in DNA has become an important topic of scientific research. However, despite of the efforts made, routine techniques (e.g., PCR) still suffer from significant drawbacks. In the burgeoning field of plasmonics, surface-enhanced Raman scattering (SERS) spectroscopy is emerging as a promising tool for the analysis of nucleic acids. Here, a simple strategy based on cationic Ag nanoparticles as plasmonic materials is presented for the ultrasensitive and label-free SERS detection of DNA. In addition, the vibrational assignment as well as the structural analysis of different DNAs is evaluated.

UNIVERSITAT ROVIRA I VIRGILI
OPTICAL DETECTION AND STRUCTURAL ANALYSIS OF DNA VIA DIRECT SURFACE-ENHANCED RAMAN SCATTERING
Patricia Gisbert Quilis

2.1. Introduction

In recent years, it has been seen an upsurge of interest in the direct SERS interrogation of nucleic acids in their native state using plasmonic colloidal solutions.[1-5] In particular, most of the scientific efforts have been devoted to overcome the lack of reproducibility that hampered the direct SERS sensing implementation.

Our group, Zeptonic, pioneered the use of spermine-coated positively charged silver colloids (AgSp NPs) as efficient substrates for the ultrasensitive direct SERS detection of DNA at the nanogram/picogram regime.[6] This approach demonstrated outstanding potential for biomedical applications.[4,6-12]

2.2. Materials and methods

Materials. Silver nitrate (99.9999%, $AgNO_3$), spermine tetrahydrochloride (≥99 %, $SpCl_4$), sodium borohydride (≥99%, $NaBH_4$), branched polyethylenimine (PEI, Mw: 25000), hydroxylamine hydrochloride ($HONH_2 \cdot HCl$) were purchased from Sigma-Aldrich. Short HPLC-purified oligonucleotides were purchased from Eurofins Genomics. $ssDNA_{21}$ and $ssDNA_{Compl.}$ were annealed for 15 min at 90 ºC in PBS 0.3 M solution (pH = 7.4) to yield the corresponding duplex $dsDNA_{21}$.

Preparation of positively-charged silver nanoparticles. Spermine-coated silver nanoparticles (AgSp NPs) were synthesized as previously described.[4] Briefly, 20 µL of a 0.5 M $AgNO_3$ solution and 7 µL of a 0.1 M spermine tetrahydrochloride solution were progressively added to 10 mL of Milli-Q water. Then, 250 µL of a freshly prepared 0.01 M $NaBH_4$ solution were quickly added under vigorous stirring to the mixture. The reaction medium rapidly turned to deep yellow, indicating the formation of silver nanoparticles. The mixture was gently stirred for another 5 min before being stored overnight in the dark. The visible sediment at the bottom of the vial was then eliminated from the sample. The so-prepared AgSp colloids normally provide a plasmonic response with excellent batch-to-batch reproducibility (only minor adjustments of the overall nanoparticle concentration may be required). Importantly, glass vials used for the reaction and storage of the particles were pre-coated with polyethyleneimine (PEI, average Mw ca. 25000 by LS) by immersion into an aqueous 0.4% v/v PEI solution

(usually overnight), followed by extensive rinsing with fresh Milli-Q water and N_2 drying. PEI infers a positive-charge to the glass surfaces preventing the deposition of the cationic silver nanoparticles. Final nanoparticle concentration (ca. 1.0 nM) was calculated according to the Lambert-Beer's law by using an extinction coefficient of 54.8×10^8 M^{-1} cm^{-1} obtained from the literature.[13]

Synthesis of hydroxylamine nanoparticles. Negatively charged silver nanoparticles (AgHX NPs) were synthesized by reduction of silver nitrate with hydroxylamine hydrochloride at room temperature following the method of Leopold and Lendl.[14] Briefly, 74.6 µL of a NaOH 1.0 M solution were added to 13.43 mL of a hydroxylamine hydrochloride 3.35 mM solution. Subsequently, 1.49 mL of a $AgNO_3$ 10.13 mM solution were quickly added to the mixture under vigorous stirring. The colloidal suspension is composed of quasi-spherical nanoparticles of an average diameter of 25 ± 5 nm, with an extinction maximum at 400 nm and a final bulk pH of ~7. NP concentration (1.26 nM) was estimated by UV-Vis spectroscopy using an extinction coefficient of 90.5×10^8 M^{-1} cm^{-1}. Nanoparticle sizes were calculated by measuring 100 NPs from different TEM images using the Java-based image processing software Image J.

SERS measurements. The samples for background SERS measurements were prepared by adding 10 µL $MgSO_4$ or $SpCl_4$ 0.1M to 150 µL of AgSp NPs 1.0 nM or AgHX NPs 1.26 nM. For the digital comparison of $dsDNA_{21}$ with the corresponding ssDNA strands, 15 µL of 10 µM ssDNAs or 15 µL $dsDNA_{21}$ 1 µM were mixed with 150 µL of AgSp NPs. SERS samples used for testing spectral reproducibility were prepared by adding 9.7 µL of 6 µM $dsDNA_{21}$ or 9.7 µL of 12 µM $ssDNA_{21}$ to 150 µL of AgSp NPs. Finally, for the concentration screening range different aliquots of $dsDNA_{21}$ ranging from 3 to 12 µL were added to 150 µL of AgSp NPs 1.0 nM (final DNA concentrations of 0.07, 0.2, 0.67, 2, 5 and 10 µg/mL, respectively).

SPR measurements. SPR samples were prepared as for SERS measurements. The samples from **Figure 2.11**, were prepared by mixing 150 µL of AgSp NPs with an aliquot of ssDNA or dsDNA at fixed initial concentration (0.31 and 0.26 mg/mL respectively) leading to a final oligonucleotide concentration of 0.02 mg/mL.

DLS and ζ potential measurements. Universal Dip cell was used for the measurements (working voltage of ζ potential 3V-5V). Each sample was left to stabilize inside the instrument at 25 ºC for 60 s before the measurement. In general, 14 runs were acquired per sample (each sample was measured 3 times).

Equipment and instrument settings. A Thermo Scientific Evolution 201 UV-visible spectrophotometer was employed to acquire the UV-vis spectra. ζ potential and DLS measurements were performed on a Malvern Nano Zetasizer. SERS experiments were performed with a Renishaw InVia Reflex confocal microscope equipped with a high-resolution grating consisting of 1800 grooves/mm for visible wavelengths, additional band-pass filters, and a CCD camera. A long-working distance objective (0.17 NA, working distance 30 mm) was used to focus a 532 nm laser onto the colloidal solutions. SERS spectra were acquired at room temperature with 20 accumulations, 15 s exposure time and a laser power at the sample of 6.9 mW. All SERS spectra were obtained by averaging 3 different replicates (per each sample).

2.3. Results and discussion

2.3.1 Cationic spermine coated Ag nanoparticles (AgSp NPs)

The wet-chemical synthesis of positively charged AgSp nanoparticles is performed by reducing silver ions with sodium borohydride in the presence of spermine tetrahydrochloride ($SpCl_4$).[7] Spermine molecules are linear quadrivalent cationic polyamines that remain bound to the nanoparticle surfaces via electrostatic interaction mediated by the chloride anions (**Figure 2.1**).[11] These chloride anions have a strong affinity for Ag and come from the $SpCl_4$ ligand.

For the synthesis of AgSp NPs, glass vials or Erlenmeyer flasks are previously coated with an aqueous solution of a positively charged polyelectrolyte, PEI 0.4% v/v. This pre-coating step, performed at least 2 h before the synthesis, is required to avoid nanoparticle deposition on the glass surfaces. In fact, silicate glass harbors a negative charge when immersed in water, mostly due to the dissociation of the ending silanol groups.

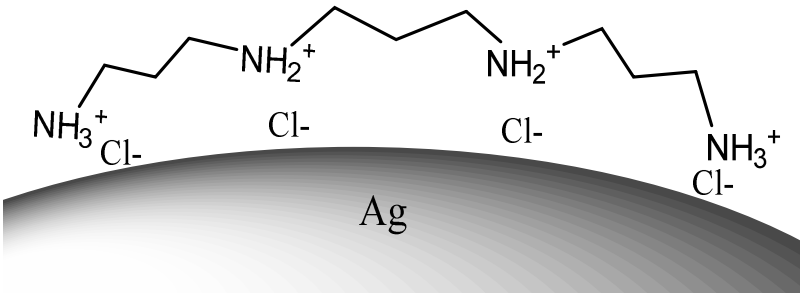

Figure 2. 1. Schematic representation of a spermine molecule electrostatically attached to the AgNP surface via chloride ions.

The extent of this dissociation and thus, the final charge at the walls relies on the equilibrium between free ions in the bulk solution and counterions at the glass walls. Then, by this pre-coating step, the deposition of the particles to the glass walls is avoided and their stability is ensured via short range electrostatic repulsions. After 2h, the glassware is rinsed extensively with Milli-Q water and dried with N_2.

2.3.1.1 Characterization of AgSp NPs

Localized surface plasmon resonance (LSPR) spectroscopy analysis

UV-visible spectroscopy is one of the most straightforward technique to characterize metallic nanomaterials. This technique enables the analysis of nanoparticles capable of supporting LSPRs. To measure the LSPR spectrum of the AgSp NPs (also referred to extinction spectrum, a combination of absorption and scattering), a white light excitation source is used and the light absorbed by the sample is measured as a function of the wavelength (**Figure 2.2**). As can be seen in **Figure 2.2**, the LSPR band of the so-synthesized AgSp NPs is centered at 392 nm.

From the spectrum, not only the concentration of the NPs can be estimated by means of the Beer-Lambert law, but also the characteristics of the substrate such as polydispersity or aggregation state can be semi-qualitatively evaluated.

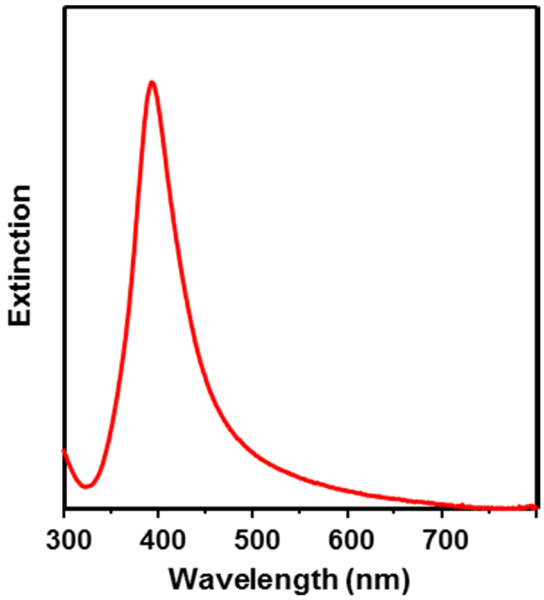

Figure 2. 2. Extinction spectrum of aqueous AgSp NPs.

Transmission Electron Microscopy (TEM)

Transmission electron microscopy is a well-established analytical tool for the study of NPs since their surface area can be projected according to the number of electrons that pass through them. In the case of AgSp NP synthesis, quasi-spherical NPs of ca. 22 nm are obtained (**Figure 2.3A,B**).This average NP size is calculated by measuring 100 AgSp NPs from different TEM images using the Java-based image processing software Image J (**Figure 2.3C**).

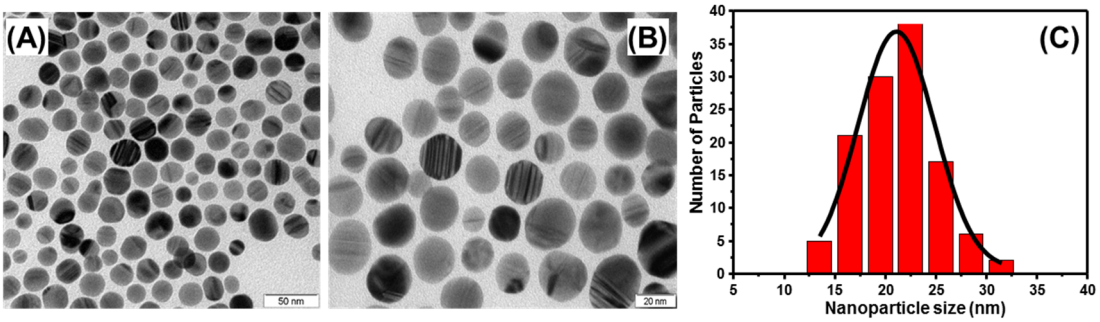

Figure 2. 3. (A), (B) Representative TEM images of the dried AgSp colloids. (C) Histogram of nanoparticle diameters (22 ± 4 nm).

ζ potential and Dynamic Light Scattering

Dynamic light scattering (DLS) and ζ potential parameters are measured with the same Malvern Zetasizer equipment. As briefly mentioned in **Chapter 1**, the electric potential measured at the slipping plane is known as ζ potential, which is

in turn indirectly related to the charge at the nanoparticle surface. Usually, ζ measurements range from -100 mV to +100 mV and are predictive of the colloidal stability. The minimum threshold for stable positive NPs is considered to be +30 mV and for negative NPs -30 mV. Positive NPs with a potential below +30 mV and negative NPs with a potential above -30 mV are predicted to be less stable. ζ potential is a good indicative of the surface charge since the direct potential at the surface cannot be measured.[15] **Figure 2.4** illustrates schematically the slipping plane where ζ potential is measured.

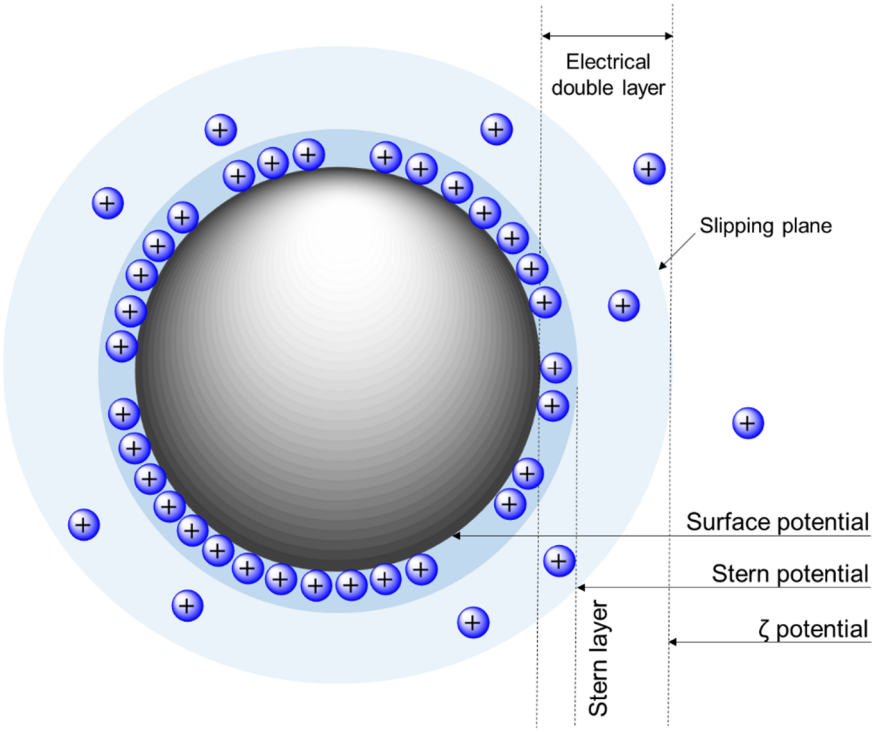

Figure 2. 4. Schematic representation illustrating where ζ potential is measured. The NP represented is negatively charged and it is surrounded by an electrical double layer of positive charges.

On the other hand, dynamic light scattering (DLS) enables the collection of the hydrodynamic diameter of the NPs, which is usually bigger than the obtained by TEM, because the samples are solvated in solution. DLS measures the fluctuations of intensity (over short periods of time) of the scattered incident light (from a laser source) by a colloidal dispersion. **Figure 2.5A** shows the ζ potential plot of AgSp NPs while in **Figure 2.5B** the hydrodynamic diameter of the NPs is

represented. AgSp NPs display an average ζ potential of +40 mV and a hydrodynamic diameter of 35.8 nm.

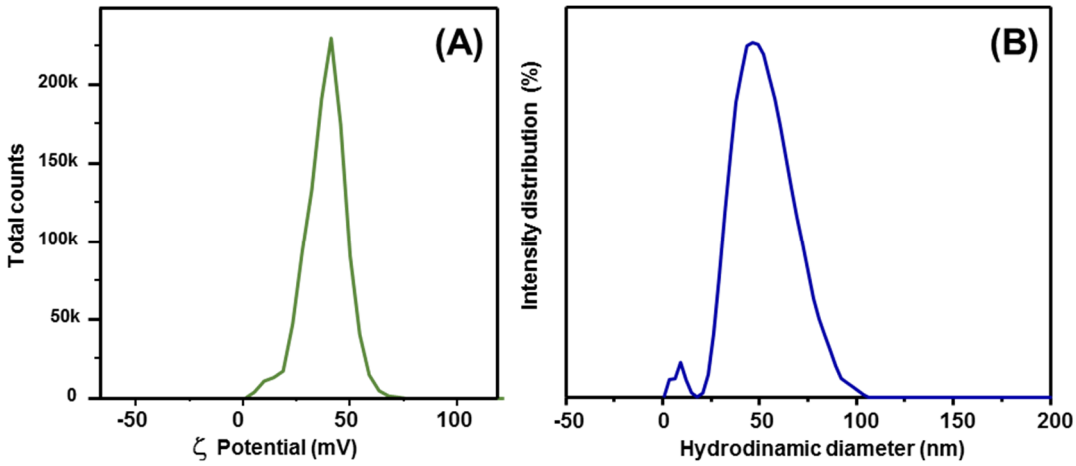

Figure 2. 5. (A) ζ Potential and (B) DLS plots of AgSp NPs (average of three replicates).

SERS background

The SERS background spectrum of AgSp NPs is acquired by aggregating the NPs with $MgSO_4$ in order to promote the formation of hot-spots (**Figure 2.6A-B**). $MgSO_4$ is a "passive" electrolyte that induces nanoparticle coagulation by simply increasing the ionic concentration without firmly adsorbing onto the silver surface. This means that it does not compete with the target molecule for the adsorptive sites. Spermine molecules provide an overall positive charge to the nanoparticles and, due to their aliphatic nature, the SERS background of the AgSp colloids shows only minimal contribution from the tetramine adlayer. **Figure 2.6B** shows more in detail the doublet at ca. 1450/1472 cm^{-1} assigned mainly to the CH_2 scissoring vibrations of spermine. These spermine spectral markers appear as weak bands in the SERS background spectrum of AgSp NPs aggregated with $MgSO_4$ while emerging much stronger when $SpCl_4$ is used as the aggregating agent. This band assignment is further confirmed when negatively charged hydroxylamine silver nanoparticles (AgHX) are used. In the case of AgHX, the CH_2 scissoring vibrations of spermine only arise in the spectrum upon aggregation with $SpCl_4$, as expected. Negatively charged silver nanoparticles (AgHX) were synthesized by reduction of silver nitrate with hydroxylamine hydrochloride at room temperature following the method of Leopold and Lendl.[14]

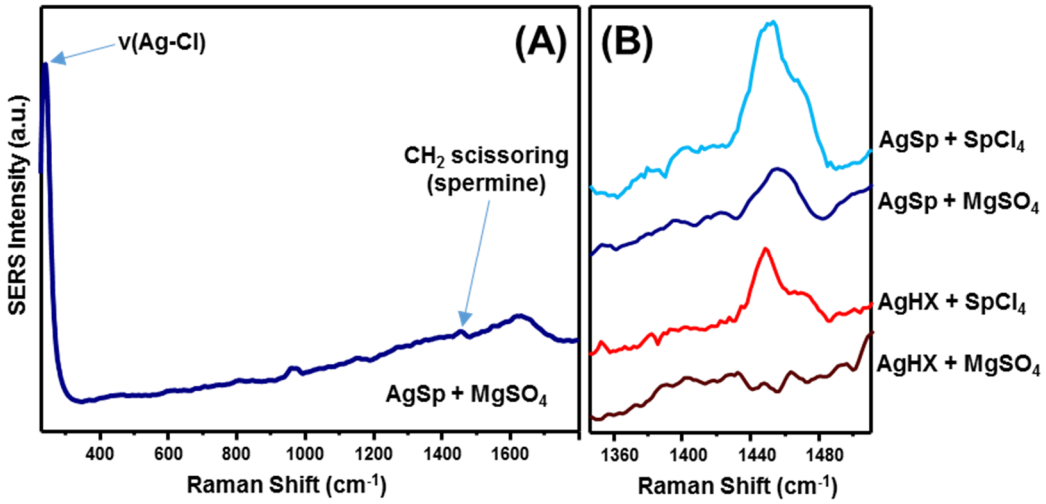

Figure 2. 6. (A) Background SERS spectrum of AgSp NPs. The spectrum was obtained by aggregating the colloids with $MgSO_4$ 0.1 M aqueous solution. (B) Detail of the 1350-1510 cm^{-1} SERS spectra of AgSp and AgHX NPs aggregated with either $MgSO_4$ 0.1 M or $SpCl_4$ 0.1 M.

2.3.2 Direct SERS analysis of DNA

Cationic AgSp NPs mediate the electrostatic adhesion of DNA, negatively charged at pH~6-7 due to the charge of the phosphate groups. This interaction yields SERS-active and long-term stable clusters in suspension, where DNA is entrapped at the interparticle junctions (i.e., hot spots). The scheme for the detection strategy is depicted in **Figure 2.7**. As discussed in **Chapter 1**, this adsorption is independent of the base composition and chain length. As a result, high quality and reproducible average SERS signals of DNA are obtained, which allow the identification and band assignment of the four canonical nucleobases (A,T,C and G) together with the phosphate backbone.[4,6] In general, the signal of the phosphate backbone is used as internal standard to normalize the SERS spectra, because is almost insensitive to structural changes, such as hybridization of DNA.[16]

Previous molecular dynamic simulations on short duplexes of 21 nucleotides (21-nt) have shown that the electrostatic adhesion of DNA on AgSp NPs takes place preferentially in three regimes within a time scale of nanoseconds.[4] The first and the second regime involve the first contact of dsDNA with the Sp molecules at the surface, followed by a relaxation stage where a more stable conformation is achieved. The final stage corresponds to the total adhesion of

DNA to the surface. In any case, the interaction takes place with minor bending of the double helix.

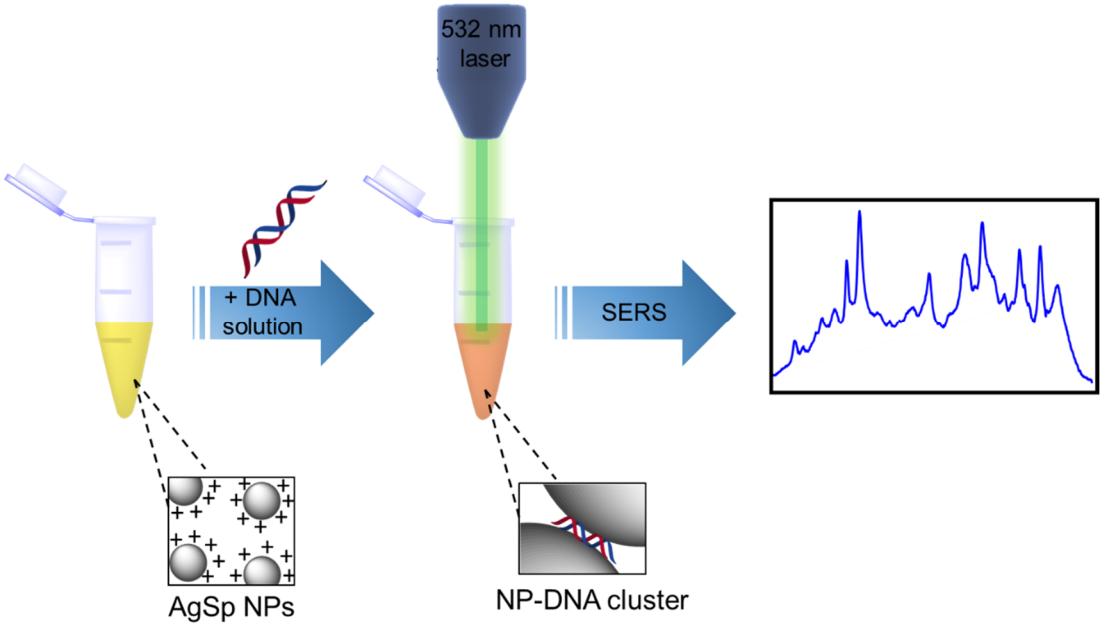

Figure 2. 7. Direct SERS sensing strategy of DNA by means of cationic AgSp NPs. The solution of isolated AgSp NPs (yellow solution) turns color to a more reddish solution due to the formation of stable NP-DNA clusters in suspension, which are finally interrogated by focusing a 532 nm laser with a long-working distance objective.

In contrast, single-stranded DNA (ssDNA) molecules are sufficiently flexible to favor the interaction through the phosphate backbone or exposing the nucleobases to the NP surface. Interestingly, it has been reported that when AgSp NPs are used, the interaction takes place preferentially through the direct coordination of the phosphate backbone onto AgSp NPs.[11] Anyway, in both cases DNA promotes the fast aggregation of AgSp NPs, without the need of aggregating agents and the SERS measurements can be performed after several hours, when the aggregation has reached the equilibrium. Under this equilibrium condition, the possible different local conformations of DNA onto the substrate leading to fluctuations in the SERS spectra are averaged out. Experimentally, it has been reported that the samples reach the equilibrium ~2 h after the initial addition of short DNAs to the colloids.[9] This was performed by measuring the spectral fluctuations of the SERS spectrum (almost entirely associated with changes in relative band intensities) upon the addition of DNA as a function of time. In the experiment, some degree of fluctuation was observed during the first hour of addition, whereas up to this threshold the SERS signal remained stable. For this

reason, 2h was established as the minimum aging time of the colloids with short DNAs prior the SERS analysis.

2.3.2.1 Vibrational band assignment of ssDNA and dsDNA

A tentative vibrational assignment of the Raman features emerging in the SERS spectra of DNA on AgSp colloids was firstly reported L. Guerrini et al. combining data from literature and direct SERS analysis of short homo- and self-complementary bi-polymeric DNA sequences.[7] This assignment also enabled better identification of the vibrational pattern of the nucleobases in heterogeneous ss and dsDNAs. **Figure 2.8** exemplifies the direct SERS vibrational analysis of two different heterogeneous DNA sequences of 21 nucleotides in single stranded ($ssDNA_{21}$) and duplex ($dsDNA_{21}$) form. Their corresponding sequences are listed in **Table 2.1**. The duplex sample was prepared by thermally annealing at 90 ^{o}C $ssDNA_{21}$ with its fully complementary strand ($ssDNA_{Compl.}$) at equimolar concentrations.

From the spectra, four main regions can be differentiated: 400-820 cm^{-1}, b820-1150 cm^{-1}, 1150-1600cm^{-1} and 1600-1800 cm^{-1}.

1) 400-820 cm^{-1}: The first spectral interval is dominated by purine and pyrimidine ring stretching vibrations of the nucleobases. These vibrations are often thought to be associated with the glycosidic bond stretching and the stretching of the bonds within the deoxyribose ring.[17]
2) 820-1150 cm^{-1}: The second region is mainly governed by the sugar group linked with the phosphodiester moiety. This last phosphate group dominates the spectral region at 1089 cm^{-1} and is originated from the symmetric stretching vibration of the PO_2^- moiety. The relatively high intensity of this band as compared to other nucleotide features suggests a close proximity of the phosphate groups to the metal surface, which is consistent with the DNA adsorption via electrostatic interactions of the negatively charged backbone.
3) 1150-1600 cm^{-1}: The third region contains different vibrational modes of the nucleobases that overlap, mostly in-plane ring vibrations.

4) 1600-1800 cm^{-1}: In this last spectral region, there is a superimposition of the carbonyl stretching modes of T, C, and G, yielding a dominant broad band in the range of 1640-1655 cm^{-1}.

Based on this analysis and from the data obtained from literature,[7,9] the tentative band assignment of ss and dsDNA is summarized in **Table 2.2**.

Table 2. 1. Single and double stranded DNA sequences.

Abbrev.	Base sequence (5'-3')
$ssDNA_{21}$	CAT CGC AGG TAC CTG TAA
$ssDNA_{Compl.}$	GTA GCG TCC ATG GAC ATT
$dsDNA_{21}$	CAT CGC AGG TAC CTG TAA GTA GCG TCC ATG GAC ATT

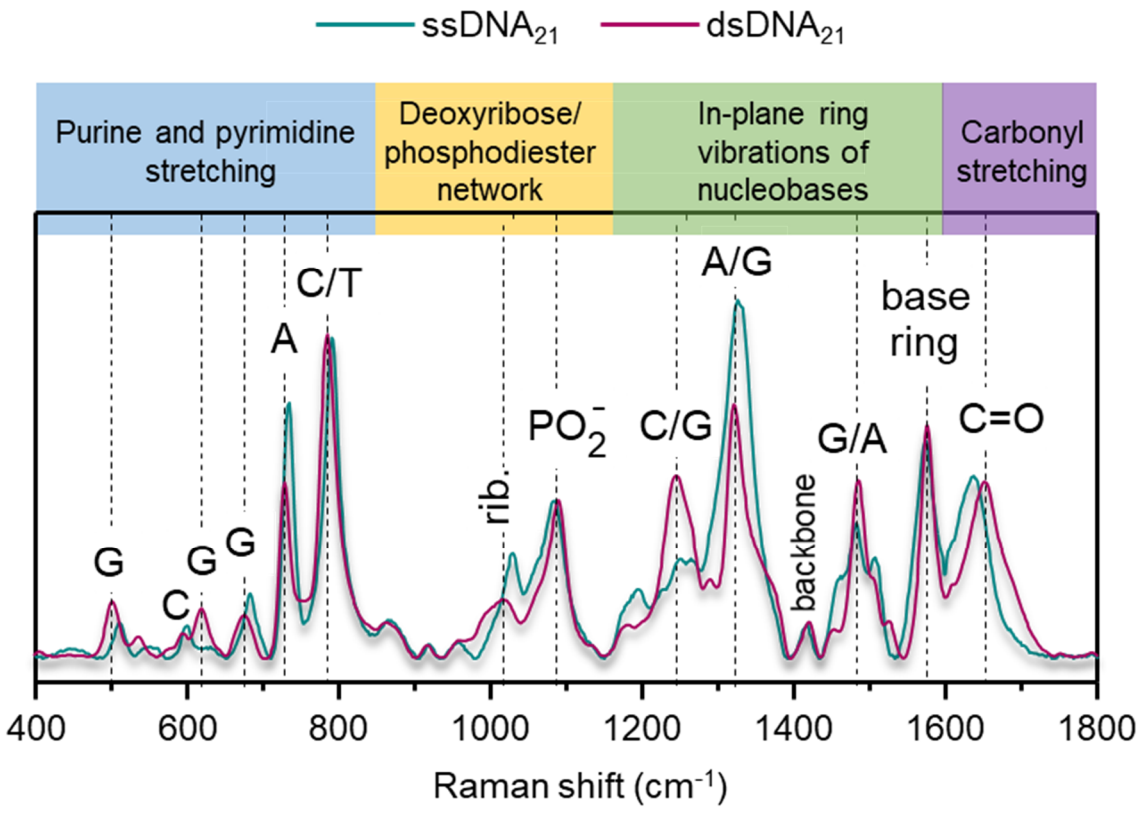

Figure 2. 8. Baseline corrected and normalized SERS spectra of $dsDNA_{21}$ and $ssDNA_{21}$ on AgSp NPs.

Table 2. 2. Band assignment of ss and dsDNA on AgSp NPs based on bibliography reports.

Raman shift of ssDNA (cm^{-1})	Band assignment	Raman shift of dsDNA (cm^{-1})	Band assignment
510	G, ring deformation	502	G
599	C, ring bending mode	620	G, ring deformation
660	G, ring breathing (C3'-endo/anti), A-form	676	G, ring breathing
684	G, ring breathing (C2'-endo/anti), B-form	729	A, ring breathing
733	A, ring breathing	785	C,T, ring breathing
792	C,T, ring breathing	1019	Deoxyribose, C
920	Deoxyribose, υ(C-C)	1089	$\upsilon(PO_2^-)$
959	Deoxyribose-phosphate	1178	T
1026	Deoxyribose, C	1244	C+G, (mainly C ring stretching)
1089	$\upsilon(PO_2^-)$	1322	A, G ring modes (mainly A)
1183	$G,\delta(C_8\text{-}H)$	1354	G
1246	C, ring stretching	1376	T
1290	A+C, ring stretching	1415	Backbone
1327	A+G, ring modes	1485	G+A, υ(C=N) imidazole ring (mainly G)
1390	A, ring mode	1506	A, υ(pyrimidine)
1415	Backbone	1528	C, ring
1460	C+T, ring modes. (A+G minor contributions)	1576	Base ring modes (mainly G+A)
1485	G+A, υ(C=N) imidazole ring (mainly G)	1628	C υ(C=O)
1509	A, υ(pyrimidine)	1653	T+C (mainly T, υ(C=O)
1574	Base ring modes (mainly G+A)	1684	T, υ(C=O)
1640	C mainly, υ(C=O)	1723	G, υ(C=O)

2.3.2.2 Spectral reshaping upon DNA hybridization

As shown in **Figure 2.8** and **Table 2.2**, the vibrational spectral profiles of ssDNA and dsDNA differ significantly, evidencing that the SERS spectrum of DNA is not only the mere contribution of the vibrational bands of the four bases but is also indicative of the base pairing by Watson–Crick hydrogen bonding, base-stacking, and chain folding. This fact provides the possibility to distinguish by SERS, DNAs on AgSp NPs with different structure (i.e., in single stranded and duplex form). To carefully examine the role of hydrogen bonding and base-stacking interactions on the final vibrational pattern of ssDNAs, two different spectra were analyzed and compared (**Figure 2.9**). First, the fully complementary

single stranded sequences ($ssDNA_{21}$ and $ssDNA_{Compl}$) were hybridized at 90 ºC resulting in the duplex $dsDNA_{21}$. Then, the SERS spectrum of this structure was compared with the digital sum of $ssDNA_{21}$ + $ssDNA_{Compl}$ spectra at equimolar concentrations. This last digitally calculated spectrum can be hypothetically considered as the "non-hybridized" mixture of $ssDNA_{21}$ and $ssDNA_{Compl,}$ based on the fact that the height of the phosphate band (1089 cm^{-1}) can be approximated, as proportional, to the number of the phosphate units within the sequences.[7] Therefore, it can be used as a reference spectrum to precisely analyze the final spectral reshaping, resulting from any structural rearrangement into the double stranded conformation.

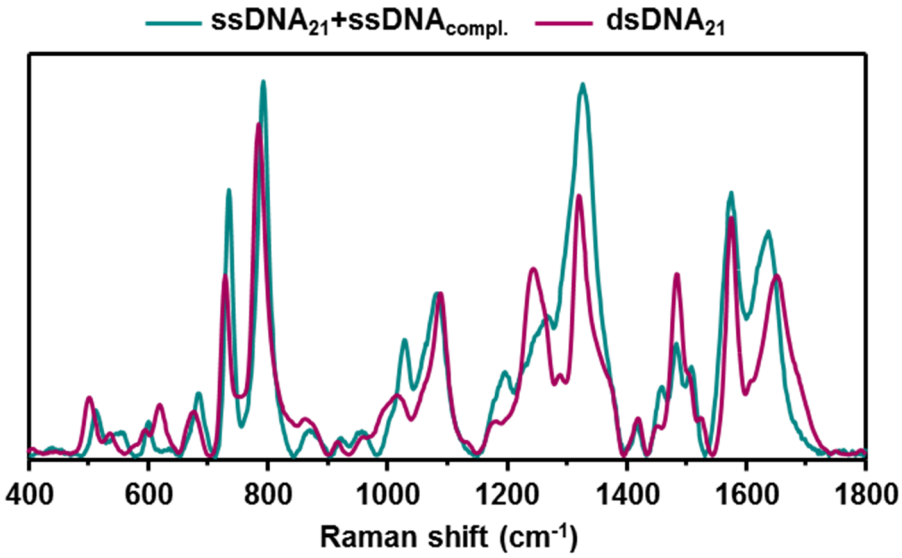

Figure 2. 9. Baseline corrected and normalized SERS spectra of $dsDNA_{21}$ (0.1 µM) and calculated $ssDNA_{21}$+$ssDNA_{Compl}$. Both spectra were normalized to the phosphate band at 1089 cm^{-1}.

From the large set of spectral differences that clearly emerge between ssDNA and dsDNA, the following can be highlighted:

1) Increase in intensity of G ring deformation in dsDNA at 620 cm^{-1}.
2) Marked peak-shifting of the ring breathing modes of A (from 733 cm^{-1} in ss to 729 cm^{-1} in ds) and C+T (from 792 cm^{-1} in ss to 785 cm^{-1} in ds) as a result of base-stacking interactions.
3) Narrowing of Raman spectral features, mostly overlapping in-plane vibrational modes of base residues, in the range 1150-1600 cm^{-1}.

4) Large blue-shift and intensity decrease of the cytosine + ribose vibration at 1019 cm^{-1} and intensity increase of the cytosine ring stretching at 1244 cm^{-1} in the duplex conformation.
5) The Watson-Crick hydrogen bonding promotes the red shift in frequency of the carbonyl stretching modes from the ss (1640 cm^{-1}) to ds (1653 cm^{-1}) form.

Therefore, AgSp colloids are potential candidates for the monitoring of hybridization or unwinding of the double helix by SERS. Further, it is important to stand out that this differentiation between ssDNA and dsDNA is only achieved with positively charged NPs since spectral irreproducibility and lack of differentiation has been reported when negatively charged are used, most probably due to denaturation of dsDNA or possible residual remaining non-hybridized sequences.[7]

2.3.2.3 Spectral reproducibility

The spectral reproducibility is a key factor in determining the successful application of label-free SERS in DNA analysis. From literature, it is well known that aggregated nanoparticle colloids yield clusters with high SERS activity but with limited control over their final geometry, size, and distribution. While this lack of control over the geometrical features of the ensemble of aggregates does affect the absolute SERS intensity, the impact on the final spectral profile can be minimized by measuring under the averaged bulk SERS regime.[18] This is the case of our study, where SERS spectra are acquired by interrogating colloidal suspensions with a long working distance lens, adopting an experimental set-up where a large number of DNA-mediated clusters, under continuous Brownian motion within the scattering volume of the objective, are simultaneously screened by the laser. **Figure 2.10** outlines the spectral reproducibility that can be achieved with the aforementioned set-up. The graph shows five stacked (A,C) and overlapped (B,D) SERS spectra replicates of short ssDNA and dsDNA sequences of 21-nt, prepared at equimolar concentrations.

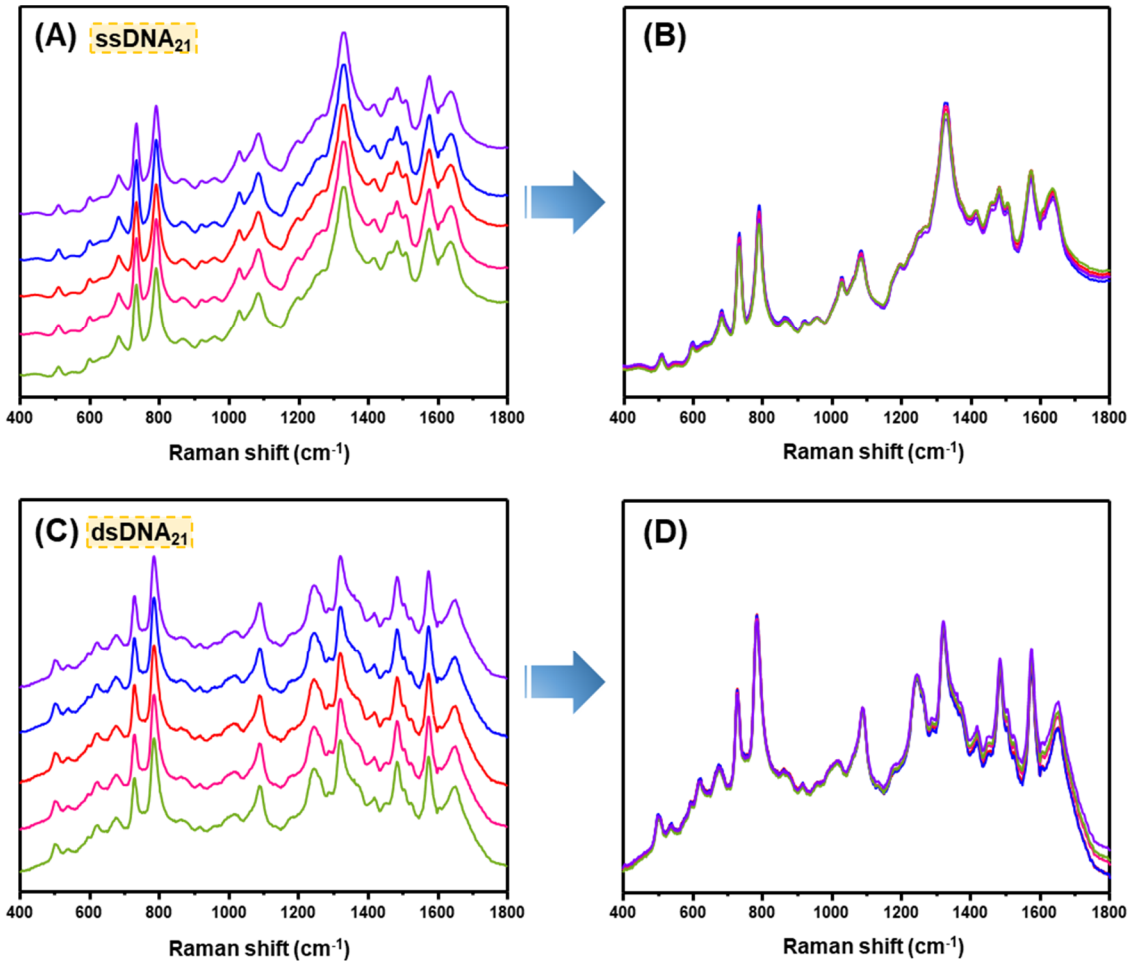

Figure 2. 10. Original non-baselined (A,C) stacked and (B,D) overlapped SERS spectra of ssDNA and dsDNA of 21-nt on AgSp NPs (4.6 µg/mL).

A second key feature that contributes to the high spectral reproducibility relies on the fact that DNA both acts as an aggregating agent of individual nanoparticles as well as a very effective stabilizing agent of the so-formed clusters. In fact, as shown for example in the extinction spectra of short single and double stranded DNA (**Figure 2.11**), upon reaching the aggregation equilibrium, the clustered colloids show a remarkable stability over relatively long periods of time with minimal spectral changes. This is particularly important since it allows us to measure the sample at equilibrium.

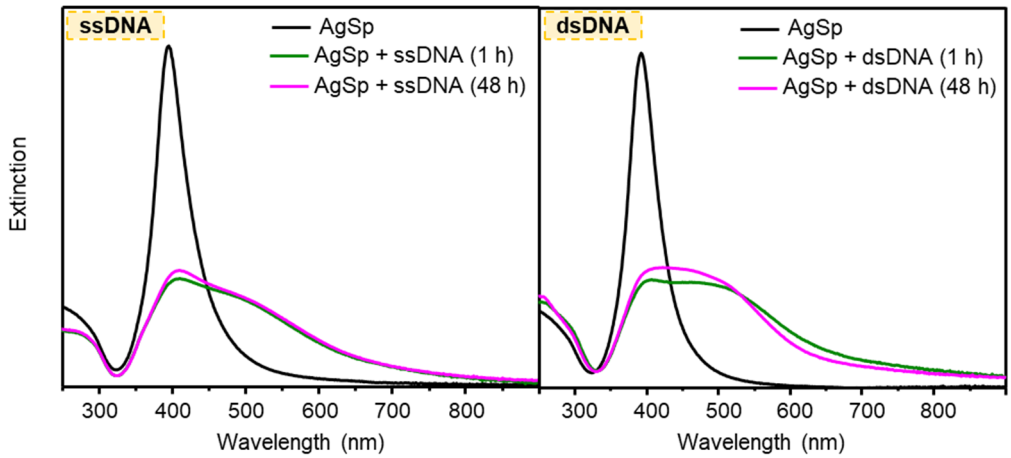

Figure 2. 11. Extinction spectra of short ssDNA and dsDNA on AgSp NPs 1h and 2 days after the initial addition of DNA to the colloids.

Therefore it is possible conclude that after 1-2h, the mixture has reached the equilibrium and the SERS measurements can be performed even 1 or 2 days after the preparation of the samples.

2.3.2.4 Optimization of DNA/NP ratio

In general, for direct SERS studies, the optimal DNA concentration has to be determined empirically in order to obtain intense SERS signals and long-term stable clusters in solution. Mainly because, as previously mentioned, DNA molecules act simultaneously as target analytes and aggregating agent. To this end, a screening study is performed by varying the DNA content while the nanoparticle concentration is kept fixed.

Figure 2.12A shows the stacked extinction spectra of short $dsDNA_{21}$ on AgSp colloids, 2 h after the addition of the initial aliquot of dsDNA. These spectra are correlated with the $dsDNA_{21}$ SERS spectra at this same concentration in **Figure 2.12B**. As can be seen in **Figure 2.12**, for the lowest dsDNA concentration (0.07 µg/mL) the SERS signal intensity is low, but still with discernible features. Over time, this sample is not stable since the NPs progressively stick to the walls of the Eppendorf. Most probably, because the positive charges of spermine are not fully screened by DNA. As the concentration is raised, a progressive increase in SERS signal intensity can be observed until a DNA concentration of 2 µg/mL. Up to this point, there is a progressive decrease of the SERS signal intensity. This fact suggests that the number of efficient hot spots in the medium decreases.

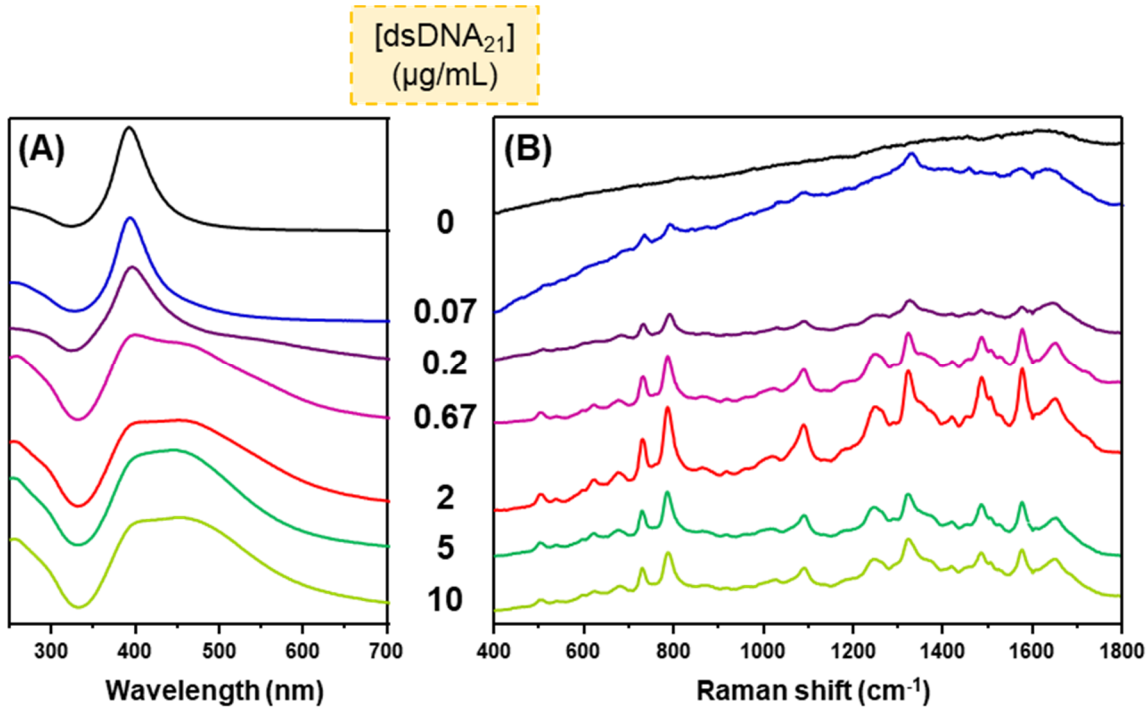

Figure 2. 12. (A) Stacked extinction spectra and (B) SERS spectra of $dsDNA_{21}$ at different concentrations on AgSp NPs, 2 h after the initial addition of DNA.

From this example, it can be observed that the vibrational profiles remain completely discernible with intense SERS signals in the ca. 0.67-10 μg/mL range of DNA concentration. It is worth noting, however, that outside this range, the SERS features may be subjected to variations in intensity, broadening or even shifts in frequency. The extent and impact of these changes on the DNA structure are fully discussed in **Chapter 4**. In addition, it is important to take into account that inherent bath-to-batch dissimilarities in the synthetized colloidal AgSp NPs may subtly affect the distribution of the DNA/NP ratios, although in the appropriate range such variations are alleviated and do not impact the reproducibility of the overall SERS response. Based on these results, 2 μg/mL has been selected as the optimal concentration of $dsDNA_{21}$. This optimization protocol can be identically applied to any sort of DNA (e.g. from single-stranded to genomic DNA).

2.3.2.5 Detection limit

Based on the previous concentration screening range (**Figure 2.12B**), the minute amount of $dsDNA_{21}$ that can be detected corresponds to ca. 70 ng/mL. This concentration corresponds to 10.5 ng in 150 μL of AgSp NPs. Considering

that the volume illuminated by the laser is smaller than the 150 µL contained in the Eppendorf tube, the real illuminated volume can be calculated as follows[19]:

$$V = 3.21\lambda^3 \left(\frac{f}{D}\right)^4 \quad (2.1)$$

Where, V is the illuminated volume, λ the excitation wavelength (532 nm), f the focal distance (30 mm) and D the lens diameter (10 mm).

By this approximation (**Equation 2.1**), V is ca. 40 μm^3 (4×10^{-9} µL). However, a range of experimental factors contribute to enlarge the scattering volume respect the theoretical calculations.[20] Among them, the continuous diffusion of NP/DNA clusters in and out the focal volume contributes to increase the actual number of illuminated DNA sequences and NPs. This fact is, in turn, dependent on the size of the cluster, number of accumulations, exposure time etc. To include these experimental factors, it is possible to conservatively calculate the illuminated volume as a cylinder of 1 mm of diameter with a depth of 6 mm. Then taking into account that for a cylinder $V= \pi r^2 h$, the illuminated volume can be estimated to be 4.7 µL and in consequence the minimum amount of $dsDNA_{21}$ that can be detected in this case is 0.329 ng.

2.4. Conclusions

In summary, cationic AgSp NPs are extremely efficient substrates to be employed in the direct label-free SERS analysis of unmodified DNA. Firstly, the rapid adsorption of DNA on the NPs takes place via non-specific electrostatic interactions with the negatively charged phosphate backbone of DNA, rather than nucleobase-specific binding. This fact simplifies the detection scheme, because DNA drives the NP aggregation removing the need of external aggregating agents (and consequently the optimization of concentration of aggregating agent, time, order of addition etc.). Secondly, DNAs are entrapped at the interparticle junctions, where the largest intensification of the Raman signal takes place. Further, the limited control on the size distribution and geometrical organization of nanoparticles into aggregates is alleviated by measuring under average SERS regime. Overall, high-quality and intense SERS spectra are yielded by long-term SERS active clusters in solution, enabling the ultrasensitive detection of DNA at the nanogram scale with outstanding batch-to-batch reproducibility. Notably, the SERS spectra obtained are truly representative of the base composition within the DNA structures.

2.5. References

(1) Panikkanvalappil, S. R.; Mahmoud, M. A.; Mackey, M. A.; El-Sayed, M. A. *ACS Nano* **2013**, *7*, 7524.
(2) Xu, L.-J.; Lei, Z.-C.; Li, J.; Zong, C.; Yang, C. J.; Ren, B. *Journal of the American Chemical Society* **2015**, *137*, 5149.
(3) Papadopoulou, E.; Bell, S. E. J. *Angewandte Chemie-International Edition* **2011**, *50*, 9058.
(4) Masetti, M.; Xie, H.-n.; Krpetic, Z.; Recanatini, M.; Alvarez-Puebla, R. A.; Guerrini, L. *Journal of the American Chemical Society* **2015**, *137*, 469.
(5) Papadopoulou, E.; Bell, S. E. J. *Chemistry – A European Journal* **2012**, *18*, 5394.
(6) Morla-Folch, J.; Xie, H. N.; Gisbert-Quilis, P.; Gomez-de Pedro, S.; Pazos-Perez, N.; Alvarez-Puebla, R. A.; Guerrini, L. *Angewandte Chemie-International Edition* **2015**, *54*, 13650.
(7) Guerrini, L.; Krpetic, Z.; van Lierop, D.; Alvarez-Puebla, R. A.; Graham, D. *Angewandte Chemie-International Edition* **2015**, *54*, 1144.
(8) Morla-Folch, J.; Xie, H.-n.; Alvarez-Puebla, R. A.; Guerrini, L. *ACS Nano* **2016**, *10*, 2834.
(9) Morla-Folch, J.; Alvarez-Puebla, R. A.; Guerrini, L. *The Journal of Physical Chemistry Letters* **2016**, *7*, 3037.
(10) Morla-Folch, J.; Gisbert-Quilis, P.; Masetti, M.; Garcia-Rico, E.; Alvarez-Puebla, R. A.; Guerrini, L. *Angewandte Chemie International Edition* **2017**, *56*, 2381.
(11) Torres-Nunez, A.; Faulds, K.; Graham, D.; Alvarez-Puebla, R. A.; Guerrini, L. *Analyst* **2016**.
(12) Gisbert-Quilis, P.; Masetti, M.; Morla-Folch, J.; Fitzgerald, J. M.; Pazos-Perez, N.; Garcia-Rico, E.; Giannini, V.; Alvarez-Puebla, R. A.; Guerrini, L. *Advanced Materials Interfaces* **2017**, *4*, 1700724.
(13) Yguerabide, J.; Yguerabide, E. E. *Anal. Biochem.* **1998**, *262*, 157.
(14) Leopold, N.; Lendl, B. *Journal of Physical Chemistry B* **2003**, *107*, 5723.
(15) Brown, M. A.; Goel, A.; Abbas, Z. *Angewandte Chemie - International Edition* **2016**, *55*, 3790.
(16) Duguid, J. G.; Bloomfield, V. A.; Benevides, J. M.; Thomas, G. J. *Biophysical Journal* **1996**, *71*, 3350.
(17) Deng, H.; Bloomfield, V. A.; Benevides, J. M.; Thomas, G. J. *Biopolymers* **1999**, *50*, 656.
(18) Aroca, R. *Surface-Enhanced Vibrational Spectroscopy*; Wiley, March 2006.
(19) Alvarez-Puebla, R. A. *Journal of Physical Chemistry Letters* **2012**, *3*, 857.
(20) Everall, N. J. *Analyst* **2010**, *135*, 2512.

UNIVERSITAT ROVIRA I VIRGILI
OPTICAL DETECTION AND STRUCTURAL ANALYSIS OF DNA VIA DIRECT SURFACE-ENHANCED RAMAN SCATTERING
Patricia Gisbert Quilis

Chapter 3

Conformational SERS classification of *K-Ras* point mutations for cancer diagnostics

Point mutations in *Ras* oncogenes are routinely screened for diagnostics and treatment of tumors (especially in colorectal cancer). Here, an optical approach based on direct SERS coupled with chemometrics is developed for the study of the specific conformations that single-point mutations impose on a relatively large fragment of the *K-Ras* gene (141 nucleobases). Results obtained offer the unambiguous classification of different mutations providing a potentially useful insight for diagnostics and treatment of cancer in a sensitive, fast, direct and inexpensive manner.

UNIVERSITAT ROVIRA I VIRGILI
OPTICAL DETECTION AND STRUCTURAL ANALYSIS OF DNA VIA DIRECT SURFACE-ENHANCED RAMAN SCATTERING
Patricia Gisbert Quilis

3.1. Introduction

Herein, the concept of single strand conformation polymorphism (SSCP) is exploited to develop a fast, simple and label-free method, combining direct SERS with partial least square discriminant analysis (PLS-DA), for discriminating long ssDNA fragments with single-base sensitivity. Such "SSCP-derived" label-free SERS approach classifies ssDNAs based on the unique strand conformations imposed by different point mutations, rather than by changes in the base composition. This allows overcoming the intrinsic limitations of previously reported direct SERS methods which were restricted to the detection of point mutations in very short strands, thus hampering their implementation into real-life applications. As a proof-of-concept, the potential of this technique is illustrated by using long fragments (141-nt) of the *K-Ras*[1] gene containing clinically relevant point mutations (with codon 12 and 13 of exon 2 as the most frequently mutated sites, and codon 17 as an infrequent but clinically relevant mutated site)[2,3] and supporting the experimental results with theoretical calculations.[4] These single nucleotide mutations are the triggers for highly oncogenic responses with the largest incidence of colorectal, lung and pancreatic cancer.[5] Currently, specific treatments are applied according to the different disorders associated with the distinct *K-Ras* mutation.[6] Therefore, the determination of the *K-Ras* punctual mutations is essential for diagnosis and prognosis.[6]

3.2. Materials and methods

Materials. All materials were of highest purity available and obtained from Sigma Aldrich (St. Louis, United States). HPLC-purified 20-nt and 35-nt ssDNA oligonucleotides were purchased from Eurofins Genomics (Esbjerg, Denmark). HPLC-purified 141-nt ssDNA were purchased from ATDBio (Southampton, UK). 200 µM stock solutions of each ssDNA fragment were prepared dissolving them in Milli-Q water (18.2 MΩ·cm at 25 °C), and stored at - 20 °C.

SERS measurements. SERS samples were prepared by mixing 150 µL of Asp NPs 1.0 nM with different aliquots of ssDNA at fixed initial concentrations (0.31, 0.54 and 4.37 mg/mL for 20-, 35-, and 141-nt respectively) leading to a final ssDNA concentration of 0.02 mg/mL for all the sequences. Thermal treated aqueous

solutions of 141-nt sequences were heated at 60 °C for 15 min before their addition to the colloids. By this gentle treatment, the extension of the chain is promoted and the ssDNAs tend to adopt a more linear conformation as previously described by Halas et al.[7] In the case of samples prepared using cold AgSp NPs, the colloids were kept for 1 h in the fridge (4°C) before the addition of 141-nt sequences.[8] All samples were left to equilibrate at least 3 hours prior to the SERS measurements (as previously reported,[9] SERS bands show some degree of fluctuations in terms of relative intensities within the first ca. 60 min upon the addition of DNA to the colloids). Upon reaching the aggregation equilibrium, the DNA-mediated clustered colloids show an impressive stability over a long time with minimal spectral changes. A total of 18 replicates were prepared and measured three times each (i.e., 54 spectra per each ssDNA sample were acquired). Multiple batches of nanoparticles were tested, observing consistently reproducible findings.

SSCP analysis. Single-strand conformation polymorphism (SSCP) was applied to the detection of genetic polymorphisms on 141-nt ssDNA mutant sequences. Eight percent acrylamide/bis gel (8.6 × 6.7 × 0.1 cm gel format) was prepared as previously described.[10] In brief, 2.6 mL 40% acrylamide/bis (37.5:1) solution, 1.3 mL 10× TBE, 0.91 mL 100% glycerol, 8 mL Milli-Q water, 130 µL 10% ammonium persulfate and 13 µL TEMED were blended and poured into the sandwich. The gel was allowed to polymerize for about 3 hours. In the case of the first three set of measurements (**Figure 3.13A-C**), the ssDNA was previously denatured at 95ºC for 7 minutes and then put on ice for about 5 minutes. For the last experiment (**Figure 3.13D**), the DNA was not thermally treated. Next, 5 µL of mutant DNA (60, 40 and 20 ng/µL) were mixed with 10 µL of a solution containing 95% formamide and 20 mM EDTA (pH = 8). The same protocol was repeated for the wild-type ssDNA. The samples were then electrophoresed with 1× TBE at 4 ºC for 3 and 6 hours, at 150 and 62 V, respectively. After the run was completed, the gel was stained with SyBr Gold (Molecular Probes – 1:10,0000 dilution) in 1× TBE buffer solution for about 20 minutes. Visualization and photographs of the staining results were taken by placing the gel inside the UV transilluminator.

Instrumentation. A Renishaw InVia Reflex confocal microscope equipped with a 532 nm laser was employed for SERS measurements. The laser was focused

onto the colloidal sample in suspension by using a macro lens (30 mm focal length, laser power at the sample of 6.9 mW). All SERS spectra illustrated in this chapter were obtained by averaging the SERS responses of 3 different replications per each sample (20 accumulations, 10 s exposure time). UV–Vis spectra were recorded using a Thermo Scientific Evolution 201 UV–visible spectrophotometer. TEM images were acquired with a JEOL JEM-1011 transmission electron microscope. TEM samples were prepared by drying 100 μL of colloid suspension on carbon-Formvar-coated 200-mesh copper grids. The ζ-potential measurements were performed with a Malvern Nano Zetasizer. The digital images of the electrophoresis gel were taken with a Chemi XL1.4 Camera (Syngene, Cambridge, UK).

Computational methods. Principal Component Analysis (PCA) and Partial Least Squares Analysis (PLS-DA) were performed using the PLS Toolbox (Eigenvector Research, Inc., Wenatchee, WA) for MATLAB (Mathworks, Inc., Natick MA). Both PCA and PLS-DA were preceded by a preprocessing step including Smoothing (SavGol, Filter Width 7), baseline subtraction (Automatic weighted Least Squares, order 3), normalization (MSC mean) and mean-centering. All the spectra were analyzed in the 400–1700 cm^{-1} range.

Data analysis. Multivariate analysis of the SERS spectral data for all ssDNA sequences was firstly performed by PCA, as a reference unsupervised classification technique. PCA enables the reduction of the number of variables into a fewer number of uncorrelated key features known as Principal Components (PCs).[11] These PCs account for the greatest difference of the entire dataset and therefore the first PC implies the greatest variance of the data, the second involves the maximal variance remaining and progressively. The maximum difference between classes of data was obtained by rotating the PCA components. Then, PLS-DA was used to further enhance the differences between ssDNA classes. This supervised classification tool is based on PLS regression method where sets of observed variables are modeled by means of Latent Variables (LV). As PCA, it comprises a dimensional alleviation of variables although there is a prior knowledge of the data.[12] All PLS-DA models were cross-validated by the Venetian Blinds method (w/ 10 splits and 1 sample per split) generally used if there are a large

number of objects randomly distributed. Quality and robustness of the PLS-DA models were assessed by R^2 (calibrated and cross-validated) values which ranged from 0.7-0.9 in PLS-DA, as well as PCA. Sensitivity and specificity of the classified SERS spectra were measured as follows;

Sensitivity = *N* samples assigned to class / actual *N* samples belonging to class

Specificity = *N* samples not classified as a member of the class / actual *N* samples not belonging to class

Molecular dynamics simulations. Molecular dynamics (MD) simulations were performed to investigate the adsorption of single stranded DNA on a positively charged nanoparticle. The SIRAH force field was used to model a completely flexible ssDNA sequence through a coarse-grained (CG) representation and explicit electrostatics.[13] A hollow nanoparticle of about 20 nm of diameter was modeled by evenly arranging mildly repulsive interaction sites on the sphere surface (internal layer, ε = 0.2 kcal mol^{-1}, $r^0/2$ = 3 Å), while adsorbed spermine molecules were approximated through a mobile distribution of positively charged beads (external layer, ε = 0.2 kcal mol^{-1}, $r^0/2$ = 2.5 Å). The surface charge density was chosen so to match a ζ potential of +40 mV at a 0.15 M monovalent salt concentration and the temperature of 298 K (1 charged group per 4.52 nm^2). The mass assigned to the nanoparticle beads was 323.6040 for uncharged particles, mimicking a three to one CG mapping (i.e. three times the mass of a silver atom), and 50.5875 for charged particles (that is a fourth of the mass of a spermine molecule). To ensure that a spherical shape was preserved during simulations, the internal layer of the nanoparticle was kept fixed during simulations, while full radial flexibility was allowed to the external layer, with the only restraint being the distance of each charged bead from the nanoparticle center (k = 10 kcal mol^{-1} Å^{-2}). This double-layered setup allowed to take into account dynamical changes in local charge distribution which are essential to properly describe the electrostatic interactions between cationic nanoparticles and phosphate groups of the DNA. Note in this case that this framework is similar in spirit, albeit different in implementation, to previously reported CG models of environmentally-responsive nanoparticles.[14]

MD simulations were performed using Amber14.[15] An implicit generalized-Born model was employed to describe the solvent,[16,17] and either high or low salt concentration was considered through a Debye-Huckel screening parameter. Langevin dynamics was performed at the target temperature of 298 K, using a frictional coefficient of 50 ps^{-1}, which mimics the collision frequency of explicit water. Equations of motions were integrated each 20 fs.

A model of the 141-nt ssDNA sequence, starting in a helical conformation, was placed at a distance of 50 Å from the surface of a nanoparticle initially located at the center of the sequence (system WT_{141}/AgSp NPs, offset = 0 Å). Then, five alternative configurations of the same system were built by shifting the centre of the nanoparticle along the ssDNA axis with a step-size of 50 Å, leading to offsets ranging from 50 to 250 Å. All the six starting geometries were simulated at low salt concentration, while only arrangements corresponding to an offset of 0 (three replicated independent simulations), 100, and 200 Å were studied at high salt concentration. All the simulations were continued until the ssDNA was completely wrapped around the nanoparticle within a total simulation time of 10 μs (see **Figure 3.2 and 3.3**). The adsorption process of short ssDNA (system 20-nts/AgSp NPs) was instead studied by placing 18 strands at a distance comprised between 50 and 200 Å from the nanoparticle at random orientations and positions. Results of simulations performed at low salt concentration are reported in **Figure 3.4**.

3.3. Results and discussion

Long ssDNA consists of a linear chain of nucleotides with thin diameter and high flexibility that, under physiological conditions, normally form stacked domains interspaced with other domains with random-coiled configuration.[18] However, at low salt solution (≤ 2 mM NaCl), the dominant electrostatic repulsions between the negatively-charged phosphates in the backbone largely prevent the nucleobases of ssDNA with relatively random sequence from approaching and pairing by hydrogen bonding.[19] This structural reorganization is clearly reflected in the SERS spectra of a 141-nt strand (wild-type, WT_{141}; **Figure 3.1**), obtained by adding equimolar amounts of ssDNA, either dissolved in Milli-Q water or in phosphate buffered saline (PBS; 0.1 M), to AgSp colloids.[20,21]

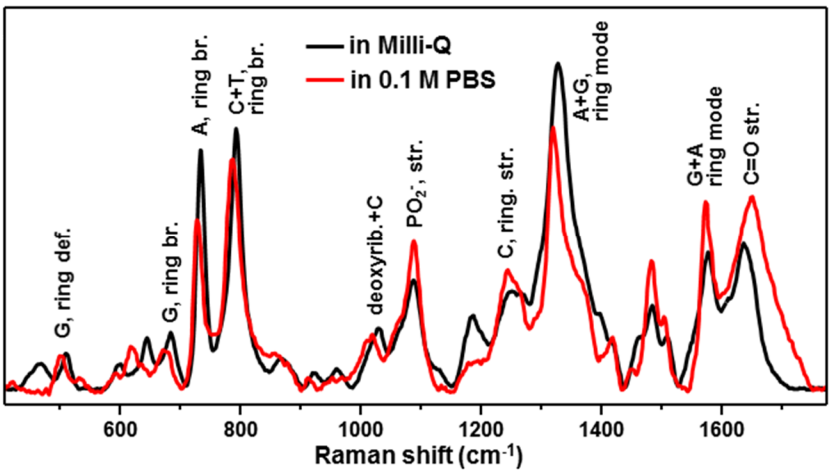

Figure 3.1. SERS spectra of the 141-nt ssDNA (WT_{141}) in low salt and high salt solutions. DNA concentration was kept constant to 2 µg per 100 µL of colloids. The SERS samples were prepared by adding an aliquot of ssDNA solution to colloids (both solutions were at 25 ºC).

The transition from low to high salt concentration determines an extended spectral reshaping consisting of a set of changes which matches those observed when individual single-strand units are hybridized into the corresponding duplex.[20] These include, among others, the large redshift of the carbonyl stretching modes at 1650 cm^{-1}, which is informative of the formation of Watson-Crick hydrogen bonds, as well as the blue-shifts of the ring-breathing modes at 680, 730 and 790 cm^{-1} (corresponding to the guanine, adenine and cytosine+thymine residues, respectively) which are associated with base stacking.[20] Thus, when ssDNA fragments are dissolved in the AgSp NPs low salt solution ([NaCl] < 1 mM), they initially exist in the bulk mainly in an elongated form,[19] then followed by their rapid adsorption and wrapping around the cationic nanospheres that act as compaction agents.[22]

The relative chain-per-nanoparticle size is expected to play a major role in determining the final DNA conformation on the 3D nanoscale object. This is well reflected by molecular dynamics (MD) simulations of the binding of long 141-nt and short 20-nt segments to cationic nanoparticles of about 23 nm in diameter. **Figure 3.2** shows the electrostatic energy of the 141-nt strand/AgSp NPs systems at low salt concentration plotted against time. A total of six starting geometries were studied, differing by the position of the nanoparticle with respect to the axis of the single-strand sequence (offset 0–250 Å from the center to the end). As it can be seen, the electrostatic energy rapidly decreases in time with an approximately

exponential decay for all the investigated geometries. Representative configurations extracted from one trajectory demonstrate that the energy plateau corresponds to states where the whole single strand was completely wrapped on the nanosphere surface.

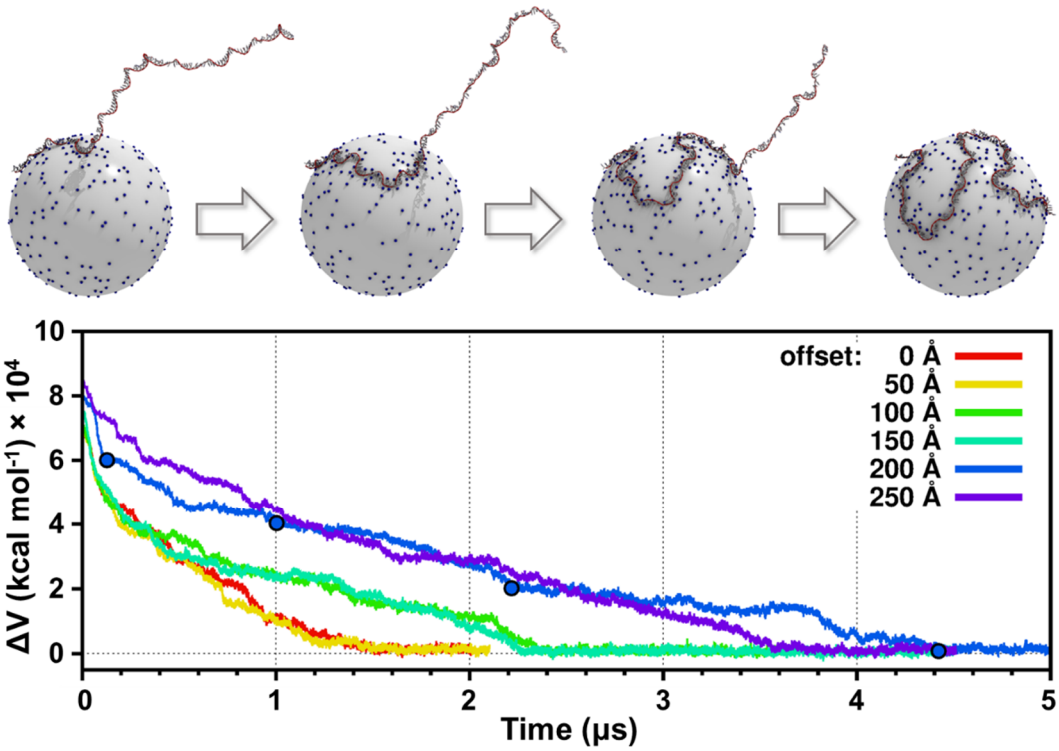

Figure 3.2. Molecular dynamics simulation of the adsorption and wrapping process of 141-nt ssDNA at low salt concentration. The difference in electrostatic energy is plotted against time for six different starting geometries (offset between the nanoparticle and the center of the single-strand sequence ranging from 0 to 250 Å). Representative configurations are reported for the starting geometry with an offset of 200 Å (blue circles in the plot). In the simulation snapshots, the DNA backbone is shown as a red tube, while positive charges on the nanoparticle are displayed as blue spheres. For clarity, the nanoparticle model is rendered as a single white sphere.

This behavior should be compared with equivalent simulations performed at high salt concentrations (**Figure 3.3**), showing that much longer times are required to converge the energy. In one case (offset = 200 Å), the wrapping process was not even completed within the total simulation time (10 μs), mirroring a substantially less efficient adsorption process.

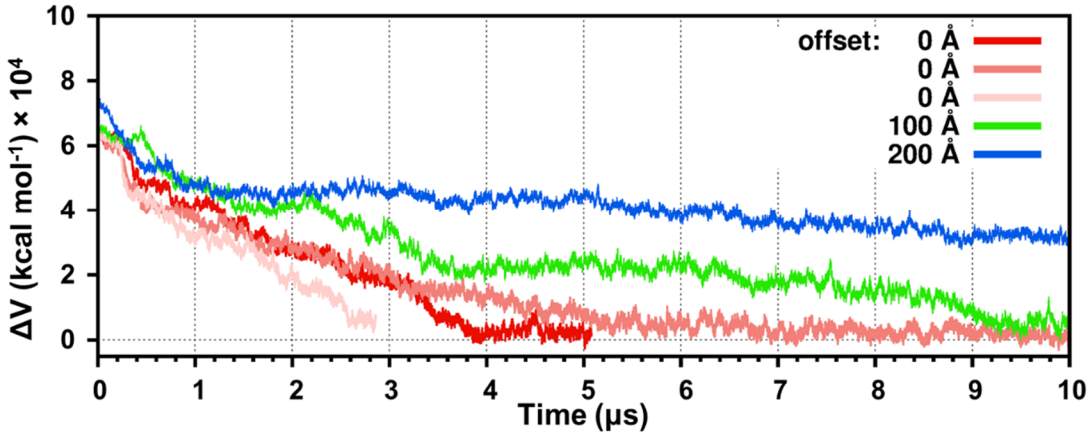

Figure 3.3. Molecular dynamics simulation of the adsorption and wrapping process of 141-nt ssDNA at high salt concentration. The difference in electrostatic energy is plotted against time for three different starting geometries. The simulation corresponding to an offset of 0 Å was repeated three times (reddish curves).

Conversely, the binding process of 20-nt ssDNA at low salt concentration turned out to be straightforward, with the short strands rapidly relaxing over the surface right after establishing favorable interactions with the surface positive charges (**Figure 3.4**).

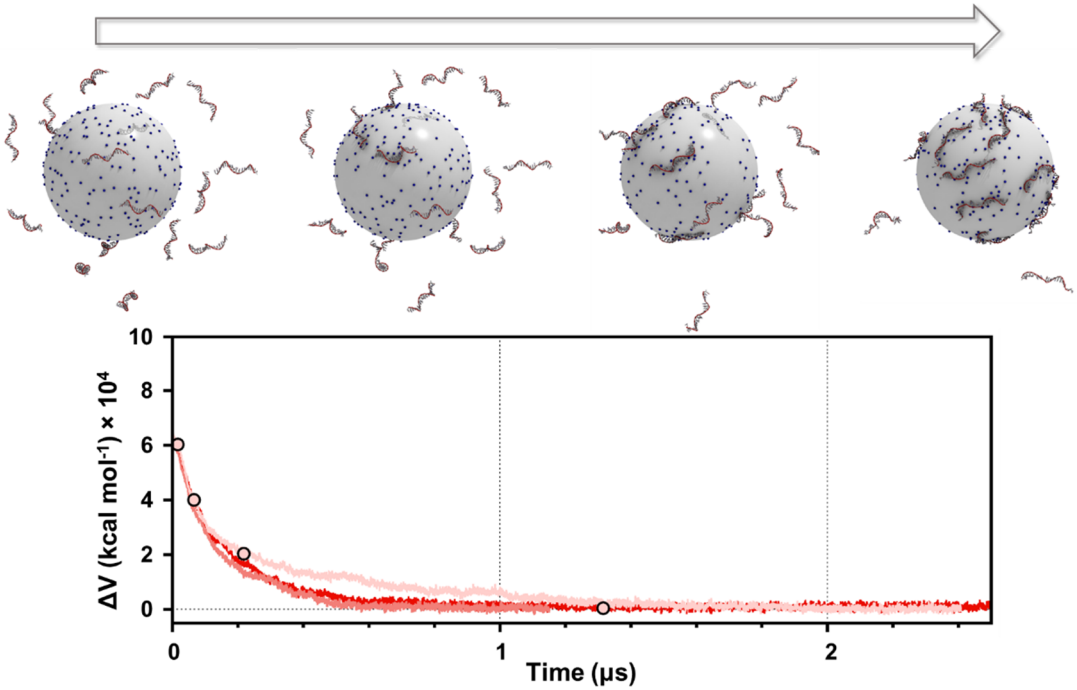

Figure 3.4. Molecular dynamics simulation of the adsorption and wrapping process of 20-nt ssDNA at low salt concentration. Representative configurations are reported for run number 3.

Direct SERS classification of long ssDNAs with point mutations was performed on 141-nt segments of *K-Ras* gene, extending from the end of intron 1 to exon 2 of chromosome 12 (**Figure 3.5**).

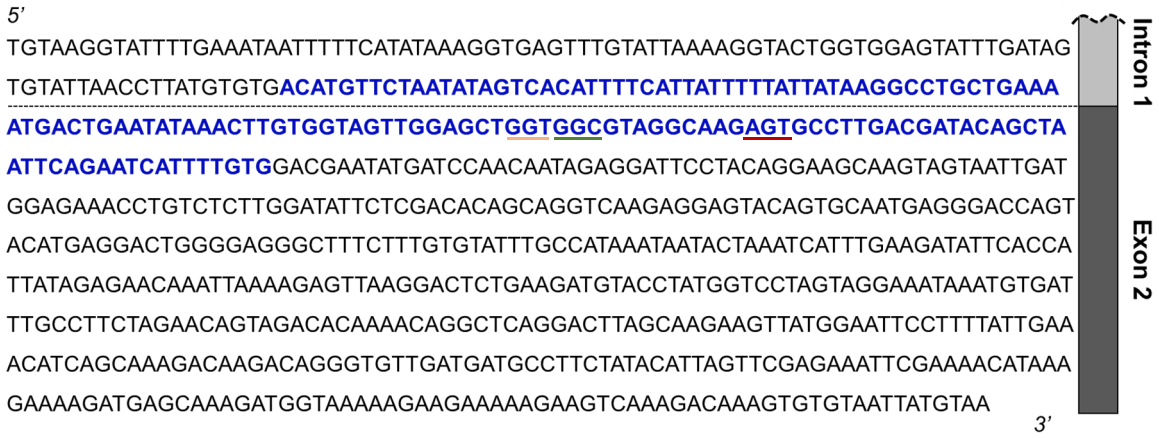

Figure 3. 5. *K-Ras* gene sequence (Intron 1 end/exon 2) of chromosome 12. In blue, the 141-nt fragment carrying points of mutation at the codons 12, 13 and 17 (G12, G13 and S17, respectively) which was investigated by SERS.

All 141-nt sequences were designed considering the recognition sites for different restriction endonuclease enzymes, such as CviAII and Hpy166II. Point mutations were selected among those for which testing should be performed in patients.[23] The first sample (WT_{141}) corresponds to the wild-type sequence while the remaining four (MTx_{141}, where x = 1 to 4) contain from one to three mutations spread at the codons 12, 13 and 17 (**Table 3.1**).

Table 3.1. Single-stranded 20- and 141-nt DNA base sequences.

ssDNA	Base sequence (5'-3')
WT_{20}	T **GGT GGC** GTA GGC AAG **AGT** G
$MT1_{20}$	T **GAT** GGC GTA GGC AAG AGT G
$MT2_{20}$	T **GAT GAC** GTA GGC AAG AGT G
$MT3_{20}$	T **GAT** GGC GTA GGC AAG **AAT** G
$MT4_{20}$	T **GAT GAC** GTA GGC AAG **AAT** G
WT_{141}	┌┌┌┌┌┌T GGT GGC GTA GGC AAG AGT G┐┐┐┐┐┐
$MT1_{141}$	┌┌┌┌┌┌T **GAT** GGC GTA GGC AAG AGT G┐┐┐┐┐┐
$MT2_{141}$	┌┌┌┌┌┌T **GAT GAC** GTA GGC AAG AGT G┐┐┐┐┐┐
$MT3_{141}$	┌┌┌┌┌┌T **GAT** GGC GTA GGC AAG **AAT** G┐┐┐┐┐┐
$MT4_{141}$	┌┌┌┌┌┌T **GAT GAC** GTA GGC AAG **AAT** G┐┐┐┐┐┐
$MT5_{141}$	┌┌┌┌┌┌T **TGT** GGC GTA GGC AAG AGT G┐┐┐┐┐┐
$MT6_{141}$	┌┌┌┌┌┌T **CGT** GGC GTA GGC AAG AGT G┐┐┐┐┐┐
	86 nt C12 C13 C17 35 nt

On the other hand, two sets of shorter homologous ssDNA fragments (20-nt and 35-nt) including the codon 12-17 region (**Tables 3.1 and 3.2**) were similarly analyzed by SERS to evaluate the impact of the strand length on the ability to discriminate base substitutions.

Table 3.2. Single-stranded 35-nt DNA base sequences.

ssDNA	Base sequence (5'-3')
WT_{35}	CT **GGT** GGC GTA GGC AAG AGT GCC TTG ACG ATA CAG
$MT1_{35}$	CT **GAT** GGC GTA GGC AAG AGT GCC TTG ACG ATA CAG
$MT2_{35}$	CT **GTT** GGC GTA GGC AAG AGT GCC TTG ACG ATA CAG
$MT3_{35}$	CT GGT **GAC** GTA GGC AAG AGT GCC TTG ACG ATA CAG
$MT4_{35}$	CT **AGT** GGC GTA GGC AAG AGT GCC TTG ACG ATA CAG
$MT5_{35}$	CT **TGT** GGC GTA GGC AAG AGT GCC TTG ACG ATA CAG
$MT6_{35}$	CT **CGT** GGC GTA GGC AAG AGT GCC TTG ACG ATA CAG
$MT7_{35}$	CT **GCT** GGC GTA GGC AAG AGT GCC TTG ACG ATA CAG
$MT8_{35}$	CT GGT GGC GTA GGC AAG **AAT** GCC TTG ACG ATA CAG

Notably, the efficient electrostatic interaction between the negatively-charged phosphate backbone of DNA and the spermine ligands, bound at the metal surface, enables the rapid nanoparticle aggregation into highly-SERS active and stable clusters in suspension yielding intense, well-defined and reproducible SERS spectra, independently of the chain length.[20,21]

Figure 3.6A shows the resulting SERS spectra of 20-nt ssDNA samples. The spectra were baseline corrected and normalized to the phosphate stretching band at 1089 cm^{-1}, which is largely insensitive to base stacking or temperature.[24] The SERS signatures of these short strands exhibit evident differences, which are mostly dominated by alterations of the relative intensities attributable to the heterogeneous base composition. Direct comparison of the SERS data by difference SERS spectroscopy (**Figure 3.7**) helps to visualize these changes, generating SERS difference spectra containing positive and negative features, respectively associated with the introduced and the replaced nucleobases. Identification of single-base sensitivity is achieved as previously described in the literature.[25]

However, new light can be shone on the discrimination capabilities of direct SERS when partial least-squares discriminant analysis (PLS-DA), a well-established and statistically robust classification method, is performed on the SERS datasets from 20-nt ssDNA samples.

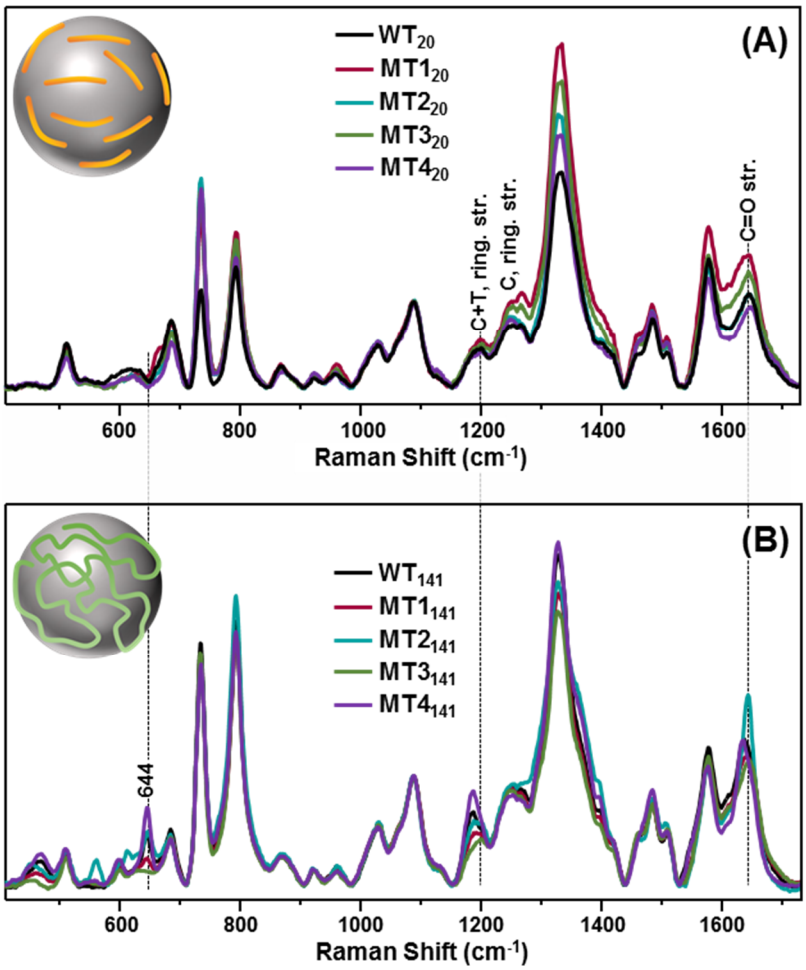

Figure 3.6. SERS spectra of A) 20-nt and B) 141-nt ssDNA. All spectra were normalized to the vPO_2^- band at 1089 cm^{-1}. The illustrated spectra are obtained by averaging 54 spectra from 18 independent replicas per sample (three measurements per each replica). The DNA concentration was kept constant to 2 µg per 100 µL of colloids. SERS samples were prepared by adding an aliquot of ssDNA solution to colloids (both solutions were at 25 ºC).

In fact, class predictions calculated by the PLS-DA supervised model and encompassing 54 spectra per sample (**Figure 3.8**) show that not only sample groups of 20-nt ssDNA with different base composition (WT_{20}, $MT1_{20}$, $MT2_{20}$, and $MT4_{20}$) can be distinguished with 100% sensitivity and specificity but also for strands which differ only in their base sequence ($MT3_{20}$ and $MT4_{20}$). In this latter case, the spectral differences are subtler than for samples with different base composition; nonetheless, PLS-DA assigns the samples into two statistically close but still differentiable classes. This is consistent with normal Raman studies that showed how base-sequence can potentially add a further layer of spectral differentiation among Raman signatures of DNA with identical base composition but different primary structure.[26]

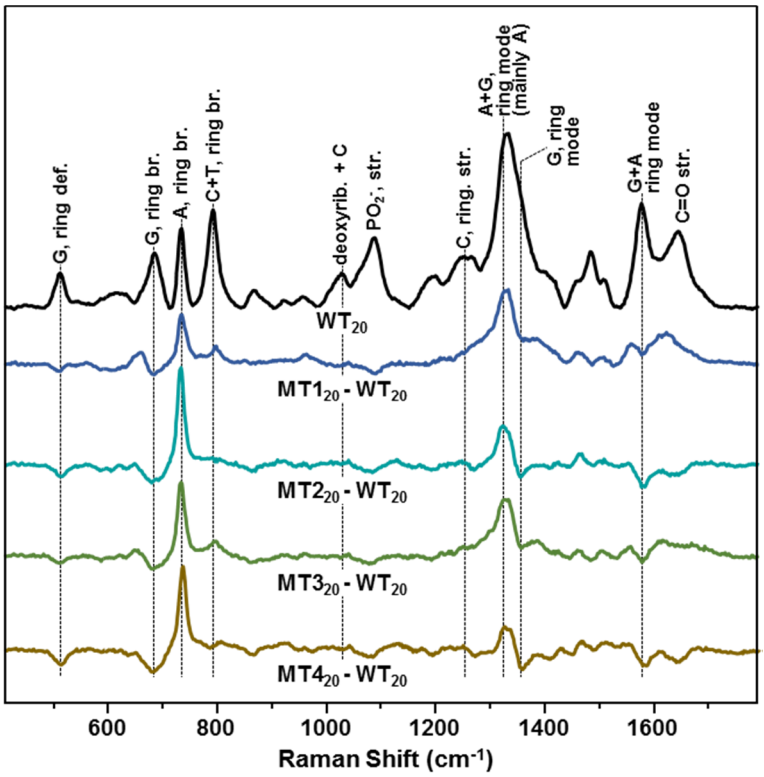

Figure 3.7. SERS spectra of WT_{20} and digitally subtracted SERS spectra $MT1_{20}$-WT_{20}, $MT2_{20}$-WT_{20}, $MT3_{20}$-WT_{20} and $MT4_{20}$-WT_{20}. Prior to the subtraction, all spectra were normalized to the vPO_2^- band at ca. 1089 cm^{-1}. The illustrated spectra are obtained by averaging 54 spectra from 18 independent replicas per sample (3 measurements per each replica). DNA concentration was kept constant to 2 µg per 100 µL of colloids. The figure includes a tentative vibrational assignment of the main SERS bands of WT_{20} on AgSp colloids based on previous works [20,21,27-29] and the data reported in the literature.[26,30-34]

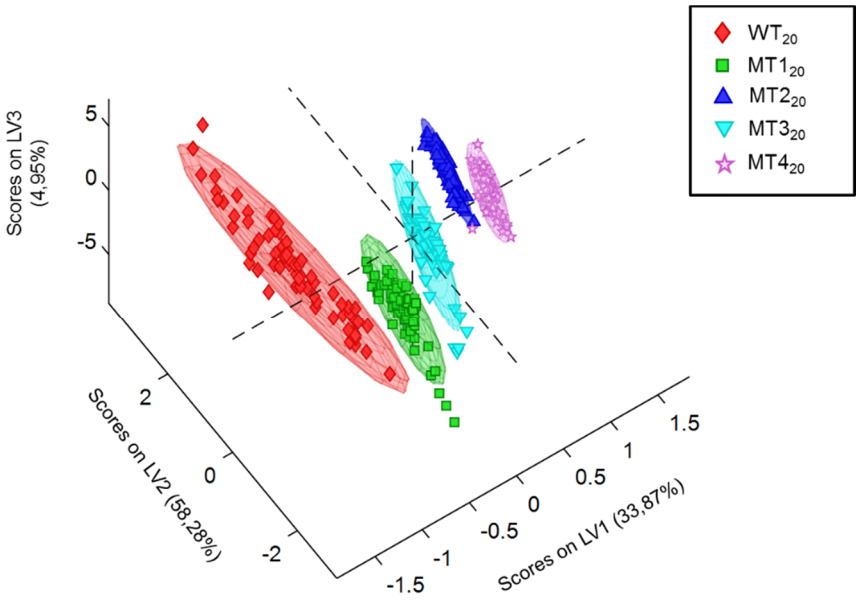

Figure 3.8. PLS-DA latent variable (LV) scores plot of the first three LV obtained from SERS spectral data of 20- nt ssDNA samples (54 replicates per sample), each spectrum is represented by a data point.

Extension of the ssDNA from 20-nt to 35-nt yielded very different results. Dilution of the single-base mutations over such chain length suppresses the capability of the direct SERS method at detecting base substitution, independently of the type and position of the mutation (**Figure 3.9A**).

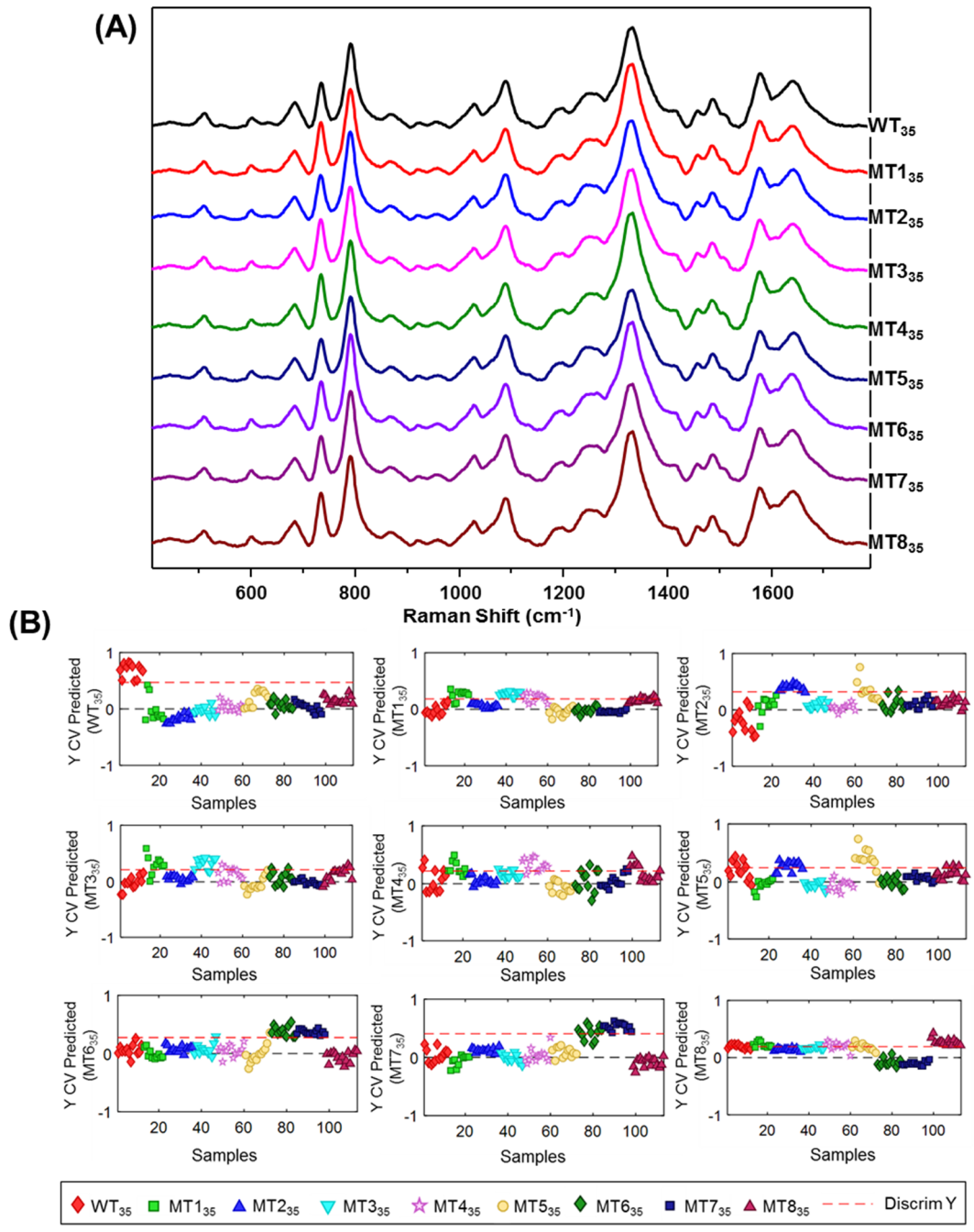

Figure 3.9. (A) SERS spectra of 35-nt ssDNA. All spectra were normalized to the vPO_2^- band at ca. 1089 cm^{-1}. The illustrated spectra are obtained by averaging 15 spectra. DNA concentration was kept constant to 2 µg per 100 µL of colloids. (B) Analysis of spectral data by PLS-DA Y predicted plots. Each plot predicts if a sample (15 SERS spectra) belongs to or not belongs to the specified class. The horizontal red line corresponds to the calculated class prediction threshold level.

Accordingly, PLS-DA model no longer classifies the samples into statistically different classes (**Figure 3.9B**). Outstandingly, when point mutations are otherwise included in 141-nt fragments, SERS spectra consistently reveal well-distinguishable vibrational profiles (**Figure 3.6B** and **Figure 3.10**), yielding full discriminatory power with single-base sensitivity (**Figure 3.14A**).

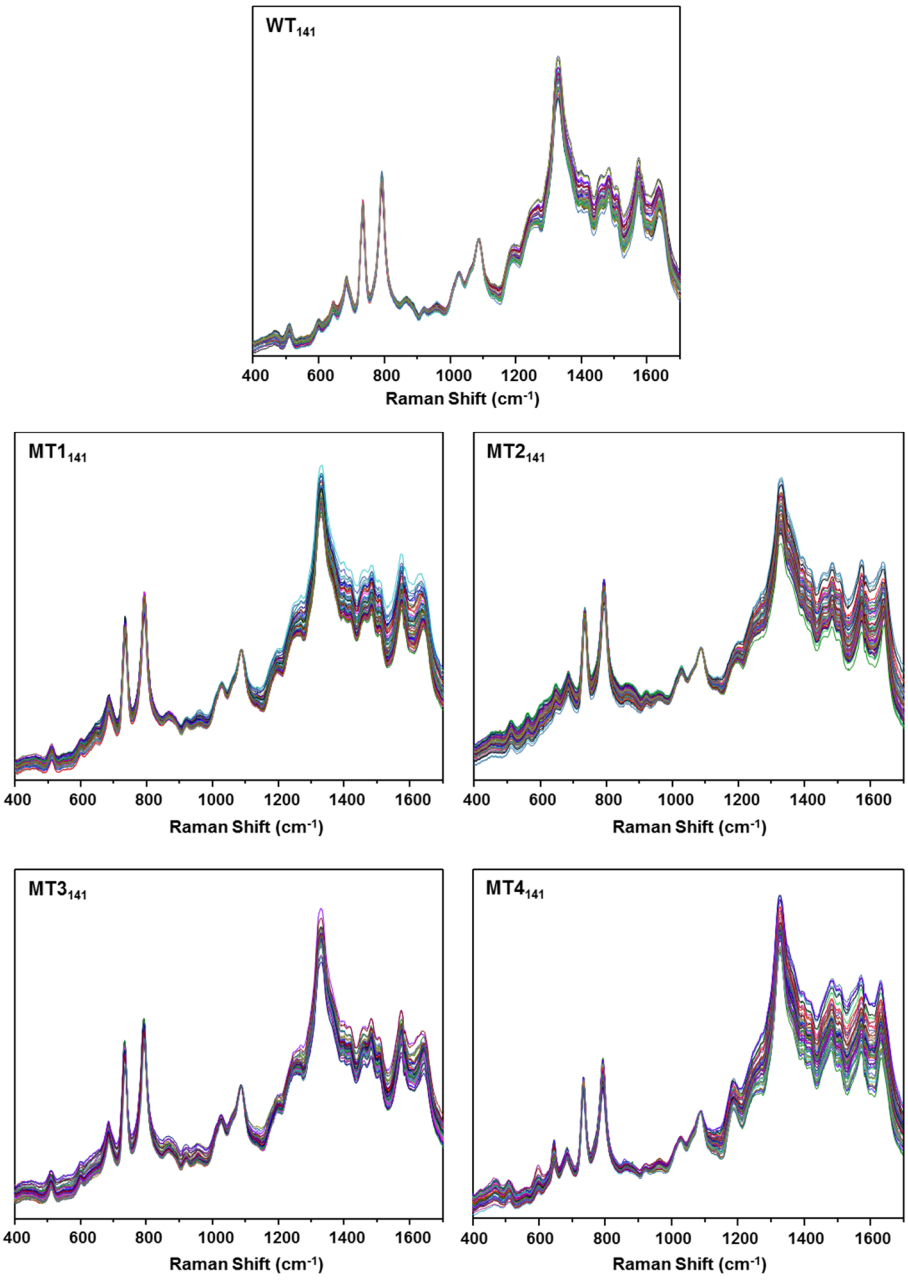

Figure 3. 10. SERS spectra of 141-nt ssDNA (WT, MT1-4). The measurements were performed by adding an aliquot of ssDNA solution to colloids both at 25 ºC. DNA concentration was kept constant to 2 µg per 100 µL of colloids.

In particular, SERS spectra of long ssDNA display a new feature at 644 cm^{-1} which has been ascribed to A+G ring stretching weakly coupled with deoxyribose

vibrations.[24] This band is diagnostic of a *C3'-endo/anti*-nucleoside conformation, a spectral marker associated to an A-form of the DNA backbone,[31] which nonetheless still co-exists with the intense G ring breathing band at 684 cm^{-1}, characteristic of the *C2'-endo/anti* conformation of the B-form backbone.[31,35] This result shows a transition from regularly ordered backbone geometry of type B, as revealed in short 20-nt and 35-nt ssDNA (**Figure 3.6A** and **Figure 3.9A**), to a broader set of different conformations for 141-nt fragments. A similar shift in conformation was determined by normal Raman studies when the protein-free single-stranded genome of bacteriophage ΦX174 in solution was packed into the viral capsid.[24] Likewise, it is reasonable to suggest that geometrical constraints imposed by the interaction with cationic nanoparticles may possibly reduce the degree of secondary structure order in long ssDNAs. Moreover, differently to what observed for short strands, the spectral changes of the 141-nt ssDNA SERS signatures are not uniquely associated with alterations of relative band intensities but significant peak shifts are also observed, such as those of the C+T ring stretching at 1180 cm^{-1} and the ensemble of carboxyl vibrations approximately centered at 1640 cm^{-1} (**Figure 3.6B**). PLS-DA was performed on the 141-nt DNA SERS spectra allowing classification of the five different fragments (**Figure 3.14A**).

The role of the specific nucleobase substitution on the discriminatory capability was further investigated by direct SERS analysis of 141-nt fragments with different single base variants in codon 12 (specifically: G→A, G→T and G→C, **Figure 3.11**).

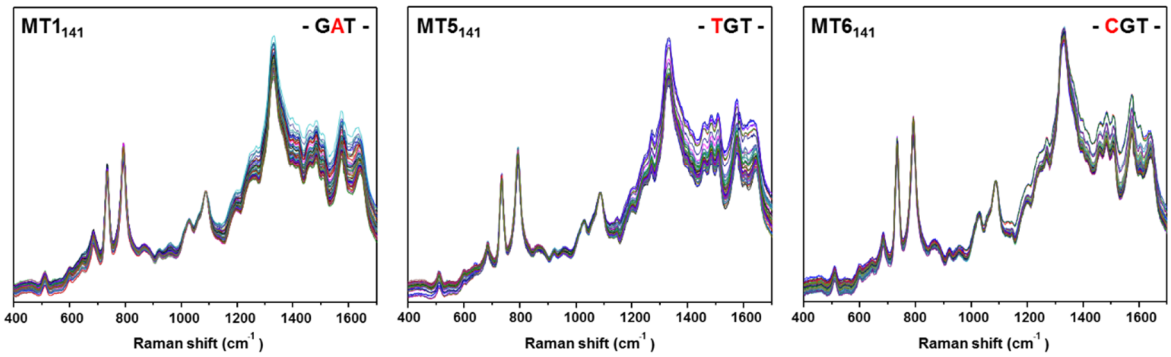

Figure 3.11. SERS spectra of 141-nt ssDNA (WT, MT1, MT5 and MT6). The measurements were performed by adding an aliquot of ssDNA solution to colloids both at 25 ºC. DNA concentration was kept constant to 2 µg per 100 µL of colloids. Point mutations at codon 12 are highlighted in red.

Similarly, PLS-DA was used to establish statistically significant differences between SERS spectra and, even for sequences with single-base substitution, the results showed 100% sensitivity and specificity (**Figure 3.12**). The outcome of the vibrational analysis is consistent with the picture provided by MD simulations. There, short strands extend over the nanoparticle in a linear fashion, sensing the metallic surface as almost flat. Under this scenario, conformational differences between strands are minimized and the discrimination between their corresponding SERS profiles largely relies on the weighted contributions of individual nucleobases. Differently, when ssDNA length is enlarged to the point where the sequence is forced to bend and fold around the nanobject, that strand-to-strand geometrical homogeneity is lost, as also reflected in the spectral changes in the SERS spectra of long fragments.

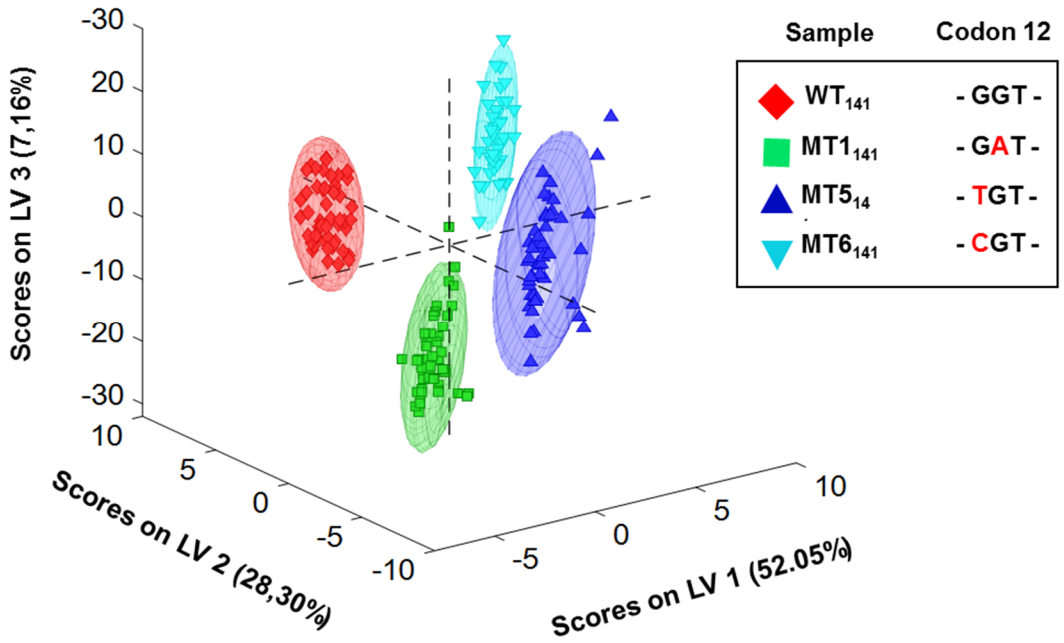

Figure 3. 12. PLS-DA latent variable (LV) scores plot obtained from SERS spectral data of WT_{141} and 141-nt sequences containing a single-point mutation at codon 12: $MT1_{141}$ (G→A), $MT5_{141}$ (G→T) and $MT6_{141}$ (G→C). The score plots are represented by the first three latent variables (LV) and each spectrum is denoted by a data point within 95% confidence ellipses, their position is characteristic for each spectrum features. The analyzed SERS spectra were acquired from samples prepared by mixing an aliquot of ssDNA solution to colloids both at 25 ºC. A total of 54 replicates per sample were acquired.

For comparison, single-strand conformation polymorphism (SSCP) analysis was also carried out on the 141-nt fragments (**Figure 3.13**). SSCP electrophoresis of DNA strands is extremely sensitive to a large set of experimental parameters

which are routinely optimized in an empirical fashion.[36-39] Accordingly, several SSCP measurements were conducted under different conditions, which allowed to finally resolve double- and triple-point mutations from wild type but not single-base substitution (**Figure 3.13D**).

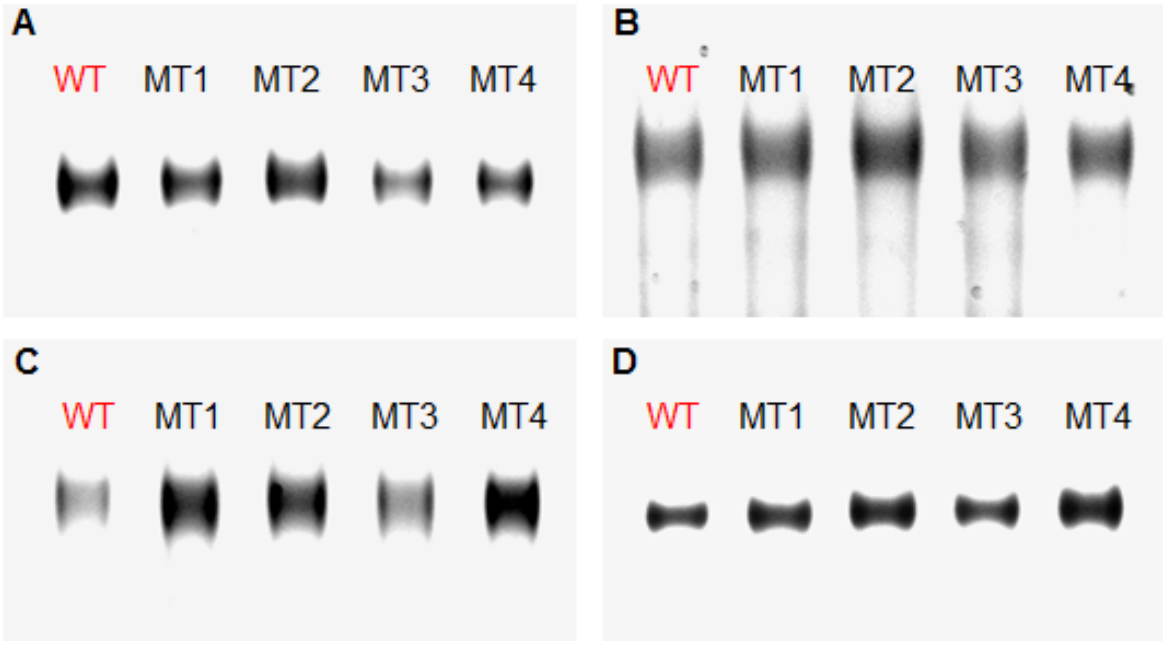

Figure 3.13. SSCP analysis of 141-nt ssDNA fragments WT_{141}, $MT1_{141}$, $MT2_{141}$, $MT3_{141}$, and $MT4_{141}$ under different experimental conditions. (A) 60 ng/µL thermally treated DNA, 3 hours at 150 V; (B) 40 ng/µL thermally treated DNA, 3 hours at 150 V; (C) 20 ng/µL thermally treated DNA, 3 hours at 150 V; and (D) 20 ng/µL non-thermally treated DNA, 10 minutes at 34 V and the next 6 hours at 62 V.

While it is not possible to rule out that a more extended optimization process would enable the identification of a specific set of experimental conditions more suitable for the successful SSCP discrimination of all investigated sequences, these results clearly demonstrate the efficiency of our SERS method at differentiating point mutations in a much simpler and reproducible fashion. To this aim, the dependence of the discrimination sensitivity of the direct SERS method from key experimental variables was examined. Specifically, as the compacting agent (nanoparticles) and ionic strength are fixed parameters in the SERS experiments, temperature (T) was selected as the experimental variable since T is well-known to affect the high ordered structure of long ssDNA.[40,41] SERS spectra illustrated in **Figure 3.6B** and statistically classified in **Figure 3.14A**, were obtained by mixing aliquots of ssDNA solutions and colloids both at 25 ºC.

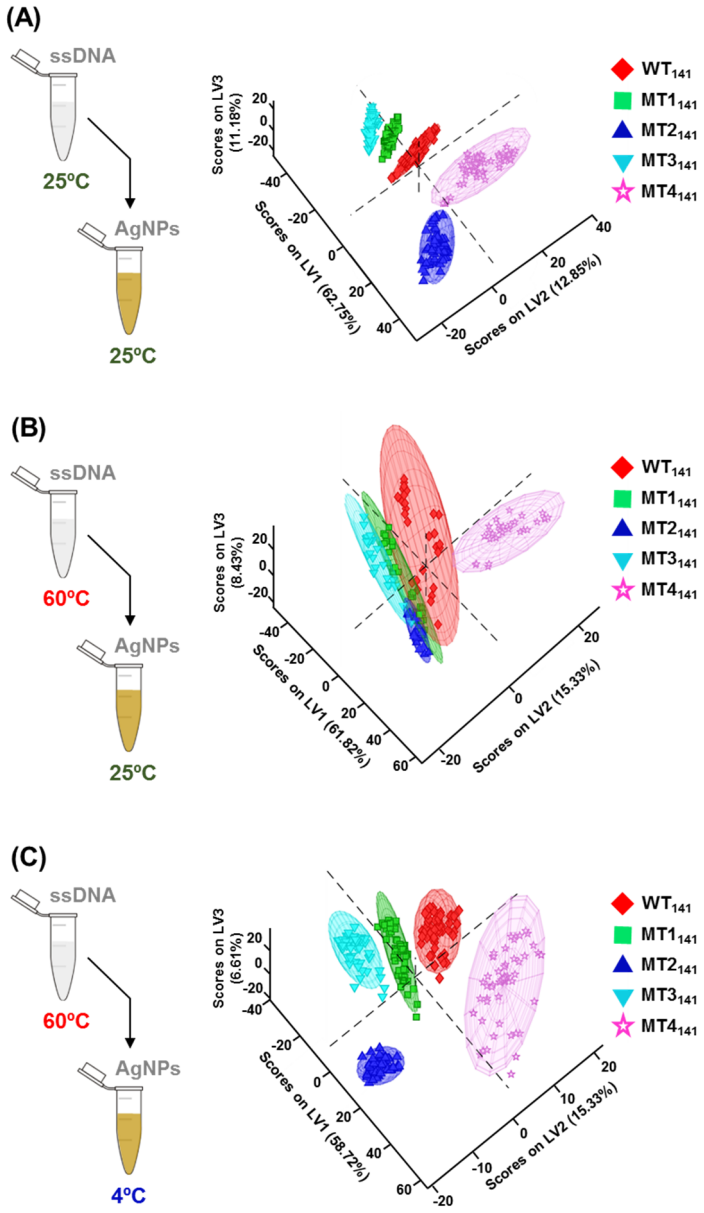

Figure 3.14. Partial least-squares discriminant analysis (PLS-DA) of SERS spectra from 141-nt ssDNA. The score plots are represented by the first three latent variables (LV) and each spectrum is denoted by a data point within 95% confidence ellipses, their position is characteristic for each spectrum features. The analyzed SERS spectra were acquired from samples prepared by mixing an aliquot of ssDNA solution to colloids at different temperature: A) both at 25 ºC; B) thermally treated ssDNA solution at 60 ºC to colloids at 25 ºC; and C) thermally treated ssDNA solution at 60 ºC to colloids at 4 ºC.

On the other hand, when ssDNA solutions were previously thermally treated at 60 ºC for 15 minutes and then directly added to cationic colloids (kept at 25 ºC), a general decrease of discrimination efficiency was observed (**Figure 3.14B**). This result is consistent with the homogeneous chain extension that a thermal pre-treatment imposes on ssDNA strands,[7] thus removing any residual intramolecular interactions. Accordingly, the sensitivity is largely recovered when thermally treated

fragments are instead mixed with colloids at 4 ºC (**Figure 3.14C**). In fact, low temperatures are expected to favor the efficient compaction of the DNA fragment[40,41] onto the metallic surface. In any case, it is worth stressing that SERS spectral profiles did not undergo major alterations upon such large temperature changes (**Figure 3.15**). This indicates that the electrostatic interaction of the flexible ssDNA chain with cationic nanoparticles remains the main driving force leading to the final higher-order structure, therefore providing the SERS method with high robustness against the intrinsic variability of normal test conditions.

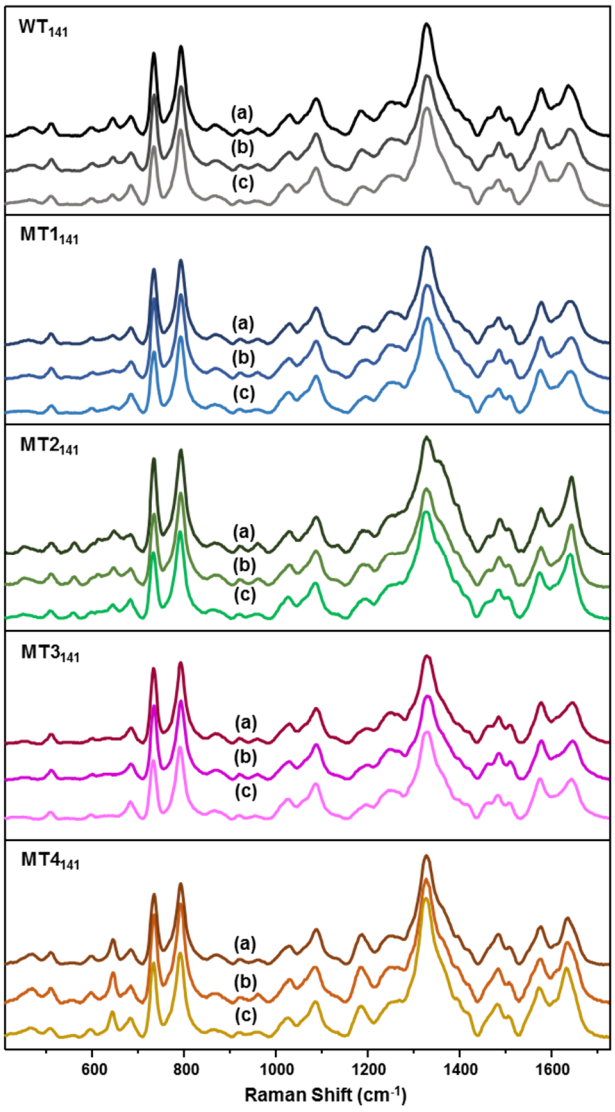

Figure 3. 15. Averaged SERS spectra of 141-nt ssDNA. All spectra were normalized to the vPO_2^- band at ca. 1089 cm^{-1}. SERS analysis was performed on different experimental conditions: (a) no thermal treated ssDNA solution was added to colloids at room temperature, (b) ssDNA solution at 60 ºC was added to colloids at room temperature, and (c) ssDNA solution at 60 ºC was added to colloids at 4 ºC. The illustrated spectra are obtained by averaging 54 spectra from 18 independent replicas per sample (3 measurements per each replica). DNA concentration was kept constant to 2 µg per 100 µL of colloids.

3.4. Conclusions

In summary, a novel label-free SERS approach for the detection of point mutations in large DNA fragments was described. This methodology mimics the concept of the single-strand conformation polymorphism technique, by exploiting the large conformational changes that single- and multiple-base substitutions impose on long single-stranded chains. The potential of this sensitive, fast, direct and inexpensive technique for diagnostics was demonstrated in the unambiguous classification of relevantly clinical mutations in *K-Ras* oncogene.

3.5. References

(1) NCBI *https://www.ncbi.nlm.nih.gov/CCDS/CcdsBrowse.cgi?REQUEST=CCDS&DATA=CCDS8702*.
(2) Bos, J. L. *Cancer Res.* **1989**, *49*, 4682.
(3) Macaluso, M.; Russo, G.; Cinti, C.; Bazan, V.; Gebbia, N.; Russo, A. *J. Cell. Physio.* **2002**, *192*, 125.
(4) COSMIC *https://cancer.sanger.ac.uk/cosmic*.
(5) Karnoub, A. E.; Weinberg, R. A. *Nat. Rev. Mol. Cell Biol.* **2008**, *9*, 517.
(6) Xu, J.-M.; Liu, X.-J.; Ge, F.-J.; Lin, L.; Wang, Y.; Sharma, M. R.; Liu, Z.-Y.; Tommasi, S.; Paradiso, A. *Journal of Experimental & Clinical Cancer Research* **2014**, *33*, 1.
(7) Barhoumi, A.; Zhang, D.; Tam, F.; Halas, N. J. *J. Am. Chem. Soc.* **2008**, *130*, 5523.
(8) Haidong, Z. In *Hypertension: Methods and Protocols*; Fennell, J. P., Baker, A. H., Eds.; Humana Press: Totowa, NJ, 2005, p 149.
(9) Morla-Folch, J.; Alvarez-Puebla, R. A.; Guerrini, L. *J. Phys. Chem. Lett.* **2016**.
(10) Orita, M.; Iwahana, H.; Kanazawa, H.; Hayashi, K.; Sekiya, T. *Proc. Natl. Acad. Sci. U. S. A.* **1989**, *86*, 2766.
(11) Abdi, H. a. W., L. J. *WIREs Comp Stat* **2010**, *2*, 433.
(12) Barker, M.; Rayens, W. *Journal of Chemometrics* **2003**, *17*, 166.
(13) Zeida, A.; Machado, M. R.; Dans, P. D.; Pantano, S. *Physical Review E* **2012**, *86*, 021903.
(14) Van Lehn, R. C.; Alexander-Katz, A. *Soft Matter* **2011**, *7*, 11392.
(15) D.A. Case; V. Babin; J.T. Berryman; R.M. Betz; Q. Cai; D.S. Cerutti; T.E. Cheatham, I.; T.A. Darden; R.E. Duke; H. Gohlke; A.W. Goetz; S. Gusarov; N. Homeyer; P. Janowski; J. Kaus; I. Kolossváry; A. Kovalenko; T.S. Lee; S. LeGrand; T. Luchko; R. Luo; B. Madej; K.M. Merz; F. Paesani; D.R. Roe; A. Roitberg; C. Sagui; R. Salomon-Ferrer; G. Seabra; C.L. Simmerling; W. Smith; J. Swails; R.C. Walker; J. Wang; R.M. Wolf; X. Wu; Kollman, P. A. *University of California, San Francisco.* **2014**.
(16) Götz, A. W.; Williamson, M. J.; Xu, D.; Poole, D.; Le Grand, S.; Walker, R. C. *Journal of Chemical Theory and Computation* **2012**, *8*, 1542.
(17) Onufriev, A.; Bashford, D.; Case, D. A. *The Journal of Physical Chemistry B* **2000**, *104*, 3712.
(18) Buhot, A.; Halperin, A. *Physical Review E* **2004**, *70*, 020902.
(19) Zhang, Y.; Zhou, H.; Ou-Yang, Z. C. *Biophys. J.* **2001**, *81*, 1133.
(20) Guerrini, L.; Krpetić, Ž.; van Lierop, D.; Alvarez-Puebla, R. A.; Graham, D. *Angew. Chem.-Int. Edit.* **2015**, *54*, 1144.
(21) Morla-Folch, J.; Xie, H.-n.; Gisbert-Quilis, P.; Gómez-de Pedro, S.; Pazos-Perez, N.; Alvarez-Puebla, R. A.; Guerrini, L. *Angew. Chem.-Int. Edit.* **2015**, *54*, 13650.
(22) Estevez-Torres, A.; Baigl, D. *Soft Matter* **2011**, *7*, 6746.
(23) Allegra, C. J.; Rumble, R. B.; Hamilton, S. R.; Mangu, P. B.; Roach, N.; Hantel, A.; Schilsky, R. L. *J. Clin. Oncol.* **2016**, *34*, 179.
(24) Benevides, J. M.; Stow, P. L.; Ilag, L. L.; Incardona, N. L.; Thomas, G. J. *Biochemistry* **1991**, *30*, 4855.
(25) Papadopoulou, E.; Bell, S. E. J. *Angew. Chem.-Int. Edit.* **2011**, *50*, 9058.

(26) Deng, H.; Bloomfield, V. A.; Benevides, J. M.; Thomas, G. J. *Biopolymers* **1999**, *50*, 656.
(27) Morla-Folch, J.; Xie, H.-n.; Alvarez-Puebla, R. A.; Guerrini, L. *ACS Nano* **2016**, *10*, 2834.
(28) Torres-Nunez, A.; Faulds, K.; Graham, D.; Alvarez-Puebla, R. A.; Guerrini, L. *Analyst* **2016**.
(29) Masetti, M.; Xie, H.-n.; Krpetic, Z.; Recanatini, M.; Alvarez-Puebla, R. A.; Guerrini, L. *Journal of the American Chemical Society* **2015**, *137*, 469.
(30) Taillandier, E.; Liquier, J.; Ghomi, M. *J. Mol. Struct.* **1989**, *214*, 185.
(31) Benevides, J. M.; Overman, S. A.; Thomas, G. J. *J. Raman Spectrosc.* **2005**, *36*, 279.
(32) Benevides, J. M.; Wang, A. H. J.; Van der Marel, G. A.; Van Boom, J. H.; Thomas, G. J. *Biochemistry* **1989**, *28*, 304.
(33) Movileanu, L.; Benevides, J. M.; Thomas, G. J. *Biopolymers* **2002**, *63*, 181.
(34) Turpin, P. Y.; Chinsky, L.; Laigle, A.; Jolles, B. *J. Mol. Struct.* **1989**, *214*, 43.
(35) Hayashi, K.; Yandell, D. W. *Hum. Mutat.* **1993**, *2*, 338.
(36) Hayashi, K. *PCR Meth. Appl.* **1991**, *1*, 34.
(37) Kusakabe, T.; Maekawa, K.; Ichikawa, A.; Uesugi, M.; Sugiura, Y. *Biochemistry* **1993**, *32*, 11669.
(38) Kakavas, V. K.; Konstantinos, K. V.; Plageras, P.; Panagiotis, P.; Vlachos, T. A.; Antonios, V. T.; Papaioannou, A.; Agelos, P.; Noulas, V. A.; Argiris, N. V. *Mol. Biotechnol.* **2008**, *38*, 155.
(39) Nataraj, A. J.; Olivos-Glander, I.; Kusukawa, N.; Highsmith, W. E. *Electrophoresis* **1999**, *20*, 1177.
(40) Orita, M.; Suzuki, Y.; Sekiya, T.; Hayashi, K. *Genomics* **1989**, *5*, 874.
(41) Suzuki, Y.; Orita, M.; Shiraishi, M.; Hayashi, K.; Sekiya, T. *Oncogene* **1990**, *5*, 1037.

UNIVERSITAT ROVIRA I VIRGILI
OPTICAL DETECTION AND STRUCTURAL ANALYSIS OF DNA VIA DIRECT SURFACE-ENHANCED RAMAN SCATTERING
Patricia Gisbert Quilis

Chapter 4

The structure of short and genomic DNA at the interparticle junctions of cationic nanoparticles

Current understanding of the mechanisms underlying noncovalent interactions between native DNA and nanoparticles, as well as their impact on the double-helix structure, is far from providing a comprehensive view. It is known that these interactions are largely defined by the physicochemical properties of the metal/liquid interface, in particular by the nanoparticle surface charge. Remarkably, while DNA unzipping upon binding with cationic nanoparticles is reported, the exact determinants of this structural perturbation remain unclear. Herein, this chapter provides new fundamental insights into the interaction between nucleic acids and nanoparticles, addressing key questions regarding the role played by multiple variables such as the nanoparticle surface charge, the DNA-mediated cluster size and geometry, and nucleic acid length, composition, and conformational properties.

UNIVERSITAT ROVIRA I VIRGILI
OPTICAL DETECTION AND STRUCTURAL ANALYSIS OF DNA VIA DIRECT SURFACE-ENHANCED RAMAN SCATTERING
Patricia Gisbert Quilis

4.1. Introduction

In this chapter, optical methods (SERS and surface-plasmon resonance, SPR, spectroscopies) and theoretical simulations (MD and FDTD) are combined to directly investigate the structural perturbation on nucleic acids imposed by the binding with cationic silver nanoparticles (ca. 22 nm diameter) with tuned ζ potential. Remarkably, the intrinsic nature of the SERS effect unlocked the possibility to selectively examine the impact of nanoparticle clustering on the double-helix integrity over a wide degree of aggregation (i.e., DNA/NP ratios) and without the need of exogenous fluorescence reporters. On the other hand, SPR analysis and molecular simulations (MS) integrated critical complementary information to the in-depth characterization of the DNA/NP interactions and the underlying mechanisms. A large set of different duplex structures with different lengths (from short segments to long genomic chain), base composition, sequence and form, were investigated. The results show that, when the nanoparticle ζ potential is lowered below a certain threshold, the double-helixes trapped at the interparticle gaps undergo major unzipping, which is largely independent of the investigated nucleic acids properties (i.e., the final outcome of the interaction is mostly determined by the electrostatic binding between phosphate groups and surface positive charges). On the other hand, for colloids with fixed ζ potentials, strand separation preferably occurs in the case of small DNA-mediated clusters (i.e., for very low DNA/NP ratios) and, to a lesser extent, in the presence of a large excess of duplexes (i.e., for very high DNA/NP ratios). In this case, however, the length of the duplex does play a relevant role in determining the pattern of the duplex structural reshaping, as the biomolecular size directly affects the features of the colloidal aggregation. These results are complemented and confirmed by MD-based simulations performed on model systems representing cluster aggregates of realistic size.

4.2. Materials and methods

Materials. All reagents were of analytical grade and used as received. All chemicals were obtained from Sigma-Aldrich except for short ssDNA and ssRNA oligonucleotides (**Table 4.1**), which were purchased from Eurofins Genomics.

Table 4. 1. Single-stranded oligonucleotide sequences

Abbrev.	Sequences
$ssDNA_{21}$	CAT CGC AGG TAC CTG TAA GAG
$ssDNA_{compl.}$	GTA GCG TCC ATG GAC ATT CTC
$ssRNA_{21}$	CUA ACA UGA CUC UCU GUC CGA
$ssRNA_{compl.}$	GAU UGU ACU GAG AGA CAG GCU
ssAT	AAT ATA ATA TAT ATA TTA TATT
ssCG	CCG CGC CGC GCG CGC GGC GCGG

Complementary single-stranded oligonucleotides ($ssDNA_{21}$ and $ssDNA_{compl.}$; $ssRNA_{21}$ and $ssRNA_{compl.}$) or self-complementary strands (ssAT and ssCG) were annealed for 15 min at 90 ºC in PBS 0.3 M solution (pH = 7.4) to yield the corresponding duplexes $dsDNA_{21}$, $dsRNA_{21}$, dsAT and dsCG. The final concentration of the resulting double-stranded oligonucleotides in solution was 50 µM. The stock solutions were stored at -20 ºC.

Cationic silver nanoparticles (AgSp). Synthesis of positively-charged colloids was carried as described in **Chapter 2**.[1] ζ potential measurements were performed by diluting the nanoparticles with either the colloidal supernatant or Milli-Q water. The supernatant was obtained by removing the nanoparticles from colloids via centrifugation at 13400 rpm for 40 min.

SERS measurements. SERS spectra at a fixed ctDNA concentration in differently diluted AgSp colloids (**Figure 4.4**) were obtained by adding 10.2 µL of ctDNA 117.2 mg/L to 150 µL of colloids. The data illustrated in **Figure 4.7** and **4.9** were extracted from the SERS spectra of $ctDNA_{21}$ and short ss- and ds-oligonucleotides ($ssDNA_{21}$, $dsDNA_{21}$, dsCG and dsAT) for different DNA/NP ratios (and fixed AgSp ζ potential). DNA/NP ratio (R) was expressed in mg of DNA per nanomoles of NP. In each case, the ratios were expressed as follows: For R = 3.6; 5.4; 10.8; 27; 54; 107.9; and 186 mg $nmol^{-1}$. For $ssDNA_{21}$, R = 0.21; 0.32; 0.64; 1.61; 3.21; 6.43; and 11.10 mg $nmol^{-1}$ and finally for $dsDNA_{21}$, R = 0.43; 0.64; 1.29; 3.21; 6.43; 12.85; and 22.16 mg $nmol^{-1}$ (identical values were used for dsCG and dsAT analysis). These samples were prepared by adding

different aliquots of DNA solutions, obtained upon proper dilution of the stock solutions, to 150 µL of colloids. The volume of such aliquots ranged between 3 to 10 µL in order to avoid significant alteration of the final nanoparticle concentration. Data reported in **Figure 4.16** were extracted from SERS spectra of DNA/RNA in AgSp at different ζ potential and fixed DNA(RNA)/NP ratios (R = 19 mg $nmol^{-1}$ for ctDNA, 3.2 mg $nmol^{-1}$ for $dsDNA_{21}$ and $dsRNA_{21}$, and 1.6 mg $nmol^{-1}$ for $ssDNA_{21}$). These samples were also prepared according to the previously described procedure. All samples were prepared and left to equilibrate overnight at 4 ºC. The samples were quickly redispersed before the SERS measurements.

ζ Potential and DLS measurements. ζ potential and dynamic light scattering (DLS) measurements were performed on a Malvern Nano Zetasizer Nano-ZS (Malvern Instruments Inc.,UK) equipped with a 4 mW He-Ne 633 nm laser. ζ potential measurements were acquired under Smoluchowski model, used for most aqueous solutions. All samples were measured by triplicate at 25 °C and constant pH (6.2). A universal dip cell (containing the electrodes) was inserted into the samples, previously placed in disposable cuvettes. Hydrodynamic size measurements were acquired with a 173° backscatter angle and calculated via the Stokes-Einstein equation. In this case, all samples were diluted 6 times in Milli-Q water, in order to avoid issues related with absorption and multiple scattering events from the sample. As for ζ potential measurements, the samples were measured by triplicate at 25 °C, using disposable cuvettes.

Equipment and instrument settings. A Thermo Scientific Evolution 201 UV-visible spectrophotometer was employed to acquire UV-vis spectra. ζ potential and DLS measurements were performed on a Malvern Nano Zetasizer. SEM images were acquired with an environmental scanning electron microscope (JEOL 6400). SERS experiments were performed with a Renishaw InVia Reflex confocal microscope equipped with a high-resolution grating consisting of 1800 grooves/mm for visible wavelengths, additional band-pass filters, and a CCD camera. A long-working distance objective (0.17 NA, working distance 30 mm) was used to focus a 532 nm laser onto the colloidal solutions. SERS spectra were acquired at room temperature with 20 accumulations, 15 s exposure time and a laser power at the sample of 6.9 mW. All SERS spectra illustrated in this chapter

were obtained by averaging the 3 different replications (per each sample). DLS samples were prepared by diluting 6 times the SERS samples in Milli-Q water prior to the measurements.

Molecular dynamics simulations. Molecular dynamics simulations were performed on two DNA-mediated cluster models, hereafter referred to as 2NP and 3NP (**Figure 4.14A**). The systems contained two and three positively charged nanoparticles, respectively. A model of $dsDNA_{21}$ was placed between each nanoparticle pair to simulate a stationary cluster aggregate. To efficiently treat nanoscopic-sized systems, a coarse-grained (CG) representation was required.[2,3] Accordingly, the SIRAH force field was chosen to model a completely flexible dsDNA with explicit electrostatics (**Figure 4.14B**).[4,5] To reduce the computational cost, in analogy to previous calculations,[6,7] hollow nanoparticles of 10 nm of radius were built using ProNOI.[8] A simple repulsive potential was used to model the surface of the nanoparticles (internal layer, ε = 0.2 kcal mol^{-1}, $r^0/2$ = 3 Å), while the positive charges provided by bound spermine molecules were simulated through a mobile density of charges (+1 e) evenly arranged on the nanoparticle surface (external layer, ε = 0.2 kcal mol^{-1}, $r^0/2$ = 2.5 Å). The surface charge density was chosen so to match a ζ potential of +40 mV at a 0.15 M monovalent salt concentration and the temperature of 298 K (1 charged group per 4.52 nm^2).The mass assigned to the nanoparticle beads was 323.6040 for uncharged particles, mimicking a three to one CG mapping (e.g. three times the mass of a silver atom), and 50.5875 for charged particles (that is a fourth of the mass of a spermine molecule). To ensure that a spherical shape was preserved during simulations, the internal layer of the hollow nanoparticle was restrained on the RMSD (Root-Mean-Squared Deviation) calculated from its initial configuration through a force constant of 15 kcal mol^{-1} $Å^{-2}$ $bead^{-1}$. Conversely, full radial flexibility was allowed to the external layer, with the only restraint being the distance of each charged bead from the nanoparticle center (k = 10 kcal mol^{-1} $Å^{-2}$). This double-layered setup allowed to take into account dynamical changes in local charge distribution which are essential to properly describe the electrostatic interactions between cationic nanoparticles and phosphate groups of the duplex. It was noted that this framework is similar in spirit, albeit different in implementation, to previously reported CG models of

environmentally-responsive nanoparticles.[9] Well-tempered metadynamics was performed to accelerate the sampling along the chosen collective variables and to reconstruct the underlying free energy surface.[10] The employed collective variables were defined as the interparticle distance between nanoparticles, and the average distance between complementary bases of the $dsDNA_{21}$ model (**Figure 4.14B**). A bias potential of the initial height of 0.05 kcal mol^{-1} was released on the collective variable space each 500 integration steps, and a bias factor of 10 units was used. The adaptive Gaussians formalism was adopted.[11] All simulations were performed using NAMD2.9[12] patched with PLUMED2.1.[13] An implicit generalized-Born model was employed to describe the solvent,[14-16] and high salt concentration was considered. Non-bonded interactions were evaluated using a cutoff and a pair-list distance of 24 and 26 Å, respectively, with a smoothing function acting at distances larger than 20 Å. Langevin dynamics was performed at the target temperature of 300 K, using a frictional coefficient of 50 ps^{-1}, which mimics the collision frequency of explicit water.[17] The CG representation allowed to increase the time-step up to 20 fs. The multiple walkers variant of metadynamics was used.[18] In particular, three walkers per system were employed, each of which was evolved for about 300 ns.

4.3. Results and discussion

The 'results and discussion' section is organized as follows. Firstly, the chemico-physical properties of the cationic nanoparticles are discussed. Then, the experimental scenario under which the direct SERS analysis of DNA takes place is described and, by means of computational tools, the spatial origin of the SERS signal is qualitatively predicted. This is propaedeutic to the interpretation of the SERS spectra revealing strand separation of both short and genomic DNA duplexes upon interaction with silver cationic nanoparticles. Two main variables of the nanoparticle-induced unzipping process were identified (degree of nanoparticle aggregation and nanoparticle surface charge) and investigated separately by SERS and SPR spectroscopies, as well as via molecular dynamic simulations.

4.3.1. Cationic silver nanoparticles

In **Chapter 2**, the wet-chemical synthesis of positively charged silver nanoparticles (AgSp) was described. The colloidal synthesis yields nanoparticles of ca. 22 nm diameter, with a LSPR band centered at ca. 392 nm and a ζ potential of ca. +40 mV (**Figure 2.2-2.6**, **Chapter 2**). ζ measurements provide the potential at the start of the diffuse layer which is indirectly related to the surface charge at the nanoparticle surface.[19] Nanoparticle concentration (ca. 1.00 nM) was determined by UV-Vis spectroscopy using an extinction coefficient of 54.8×10^8 $M^{-1} \cdot cm^{-1}$ at 392 nm, as obtained from the literature.[20,21] Dilution of the AgSp colloids with Milli-Q water promotes a progressive reduction in plasmon intensity (**Figure 4.1A**) with null or minimal perturbation of the colloidal stability (**Figure 4.1B**). From the figures, the top curve to the bottom curve, the estimated nanoparticle concentrations are the following: 1.00 nM, 0.91 nM, 0.79 nM, 0.70 nM, 0.55 nM, 0.44 nM, 0.34 nM, 0.24 nM, 0.20 nM, 0.16 nM and 0.12 nM. A representative TEM image of the dried nanoparticles is also included (the scale bar represents a length of 20 nm).

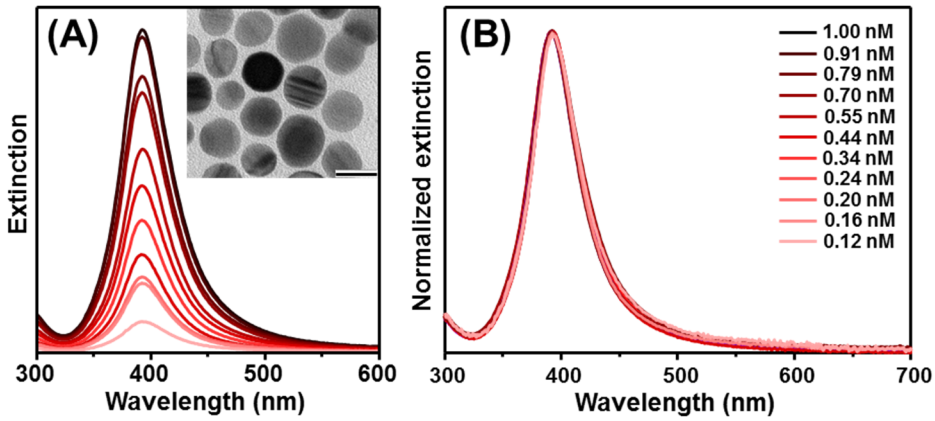

Figure 4. 1. (A) Extinction spectra of AgSp colloids at different concentration upon dilution with Milli-Q water. (B) Normalized extinction spectra of AgSp colloids at different concentration upon dilution with Milli-Q water. The lack of relevant broadening of the plasmonic profile indicates that no significant colloidal aggregation occurs upon dilution.

At the same time, a decrease of ζ potential (**Figure 4.2**) was observed, which is consistent with the partial desorption of spermine molecules from the metallic surface upon dilution with Milli-Q water. This is further confirmed by the fact that ζ potential value remains unchanged when nanoparticles are diluted with the colloidal supernatant (**Figure 4.2**).

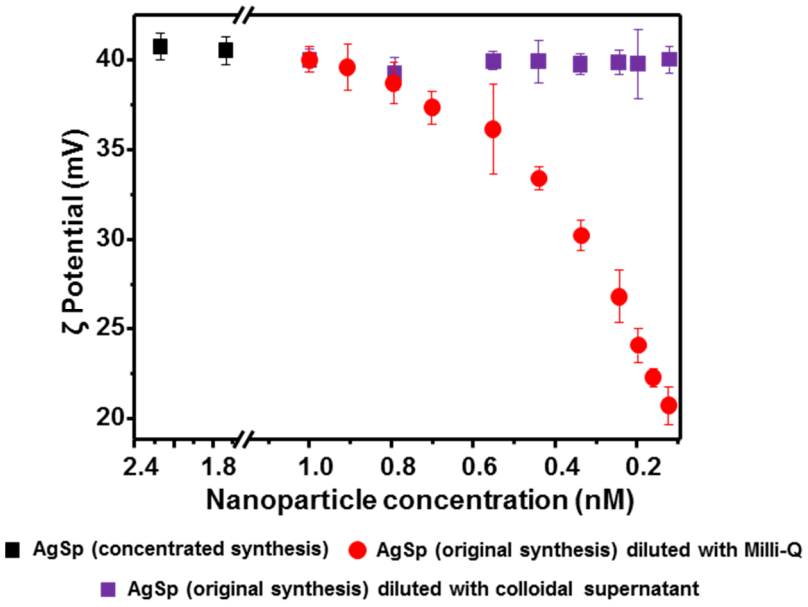

Figure 4. 2. ζ potential values (mV) for AgSp colloids at different concentration upon dilution with Milli-Q water (red dots) and colloidal supernatant (purple dots). The nanoparticle-free colloidal supernatant was separated from AgSp colloids by centrifugation at 13k rpm, 40 min. Contrary to the dilution with Milli-Q water, no relevant changes in ζ potential are observed upon dilution with the colloidal supernatant (i.e., metal surfaces are saturated with spermine molecules independently of the nanoparticle concentration). Black points refer to AgSp colloids prepared by proportionally increasing the concentration of the reagents ($AgNO_3$, $SpCl_4$ and $NaBH_4$) in the mixture as compared to the original synthesis described in the experimental section.

4.3.2. The dominant contribution of DNA molecules at the interparticle gaps to the final SERS spectrum

In previous works, it was shown that short DNA duplexes of 21 base pairs ($dsDNA_{21}$) mediate AgSp nanoparticle aggregation acting as electrostatic molecular linkers.[22] This interaction takes place through the spermine molecules on the Ag surface, which provide an overall positive charge to the nanoparticles and electrostatically interact with the negatively-charged phosphate backbone of DNA/RNA.[23]

Under physiological conditions, double-stranded DNA persistence length (i.e. local stiffness) is of approximately 150 bp, corresponding to ca. 50 nm.[24] As a result, $dsDNA_{21}$ behaves as a rigid rod of ca. 7 nm length and 2 nm diameter, which is collected at the surface of individual quasi-spherical nanoparticles of around 22 nm diameter with minimal bending of the double helix.[25] Molecular dynamics simulations of $dsDNA_{21}$ adsorption on AgSp nanoparticles previously

indicated that the duplex rapidly adheres onto the metal surface adopting an elongated conformation (for low surface coverage).[23] Consequently, interparticle gaps of approximately 2.5 nm are generated in $dsDNA_{21}$-mediated clusters (i.e., the diameter of the duplex rod-like structure sandwiched between spermine molecules bound to the metallic surfaces). It is also worth noting that, in addition to their physical size, DNA molecules coordinated at the metallic surfaces screen further adsorption of unbound duplexes by electrostatic repulsion.[26] The extent of this electrostatic repulsion is larger at low salt concentrations such as for the investigated AgSp colloids (ca. 1-2 mM NaCl resulting from chemicals employed in the nanoparticle synthesis and the PBS buffer of DNA solutions).[26] Thus, the formation of a hypothetical compact monolayer of $dsDNA_{21}$, corresponding to ca. 100 molecules per particle (based on the average NP diameter and $dsDNA_{21}$ footprint), is disfavored and duplexes are expected, on the contrary, to be rather scattered over the nanoparticle surfaces even for high DNA concentrations in the bulk.[26]

Direct SERS analysis was performed on the colloidal suspension by focusing a 532 nm laser with a long working distance lens so as to acquire averaged bulk SERS spectra with reproducible and well-defined spectral profiles.[1,22,27] Under this scenario - relatively small gaps and nanoparticle radius (i.e., large curvature at the interparticle junctions), combined with an excitation wavelength that matches the red-shifted gap plasmon resonances[1] - the SERS intensity of aggregated colloidal systems is largely dominated by those few molecules located at the gap volume (hot spot).[28-30] In support of this claim, a finite difference time domain (FDTD) method was used to calculate the electromagnetic field distribution around a silver nanoparticle dimer in water (particle diameter = 22 nm; gap distance = 2.5 nm, such as that generated by a $dsDNA_{21}$ duplex extended over the metallic surface) illuminated by a 532 nm laser. In **Figure 4.3A** a horizontal and a vertical cut of the field intensity (*xy*- and *xz*-plane, respectively) are shown. From the figure, it can be appreciated that the EM field is strongly confined in the gap. Knowing how the electric field decays, the volume of the hot spot can be estimated considering the full width at half maximum (fwhm) of the electric intensity, $|E|^2$ (**Figure 4.3B**), in each direction.

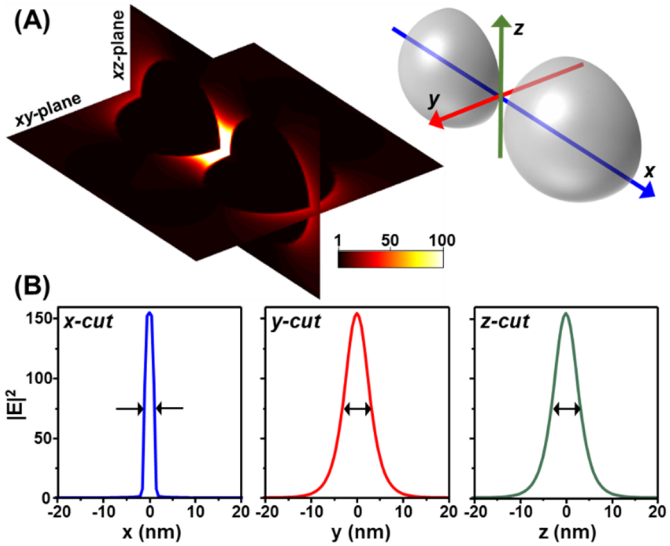

Figure 4. 3. Electromagnetic near field intensity calculations showing the volume size of the hot-spot. (A) Spatial near field map of $|E|^2$ along the xy and xz planes (black color is zero while white represent a value of 100). The values of $|E|^2$ along each axis are also shown in (B), where it can be appreciated that the x-cut has the gap width while the field along the other two directions has a half-width at half-height around 3 nm.

Approximating the hot-spot volume, V, as a cylinder whose height is given by the gap distance (i.e., 2.5 nm) and the radius is ca. 3 nm (i.e., fwhm), a value of V = 70 nm^3 can be estimated. Based on the intrinsic size of the adsorbed $dsDNA_{21}$ surface complex (ca. 30-35 nm^3) and the sparse surface coverage imposed by electrostatic repulsions between duplexes, it can be safely inferred that no more than one $dsDNA_{21}$ molecule is located at the hot-spot. This means that one individual duplex placed at the gap is responsible for the vast majority of the SERS signal arising from the dimer. Such conclusion can be qualitatively extended to the large ensembles of DNA-mediated clusters in suspension (i.e., the acquired SERS spectra specifically inform about the fraction of duplex molecules bridging cationic nanoparticles into aggregates, even for high DNA concentration).

4.3.3. SERS spectra reveal DNA strand separation

While AgSp colloids immediately aggregate upon addition of a short duplex, the complexation process between long genomic calf thymus DNA (ctDNA) and nanoparticles is slower and requires a longer time to reach its final equilibrium state.[26,31] For this reason, SERS analysis was performed on samples in suspension after overnight incubation to reach binding equilibrium[26] (aggregates

sitting at the bottom of the Eppendorf were resuspended just before the optical measurement). Salt concentration was maintained low (millimolar of NaCl) throughout the whole study to minimize unspecific salt-induced aggregation of the nanoparticles (however, it is worth reminding that ion concentration at the nanoparticle surfaces differs from the bulk).[32] **Figure 4.4** illustrates the SERS spectra of ctDNA at a fixed concentration on AgSp colloids with different ζ potential and nanoparticle concentration.

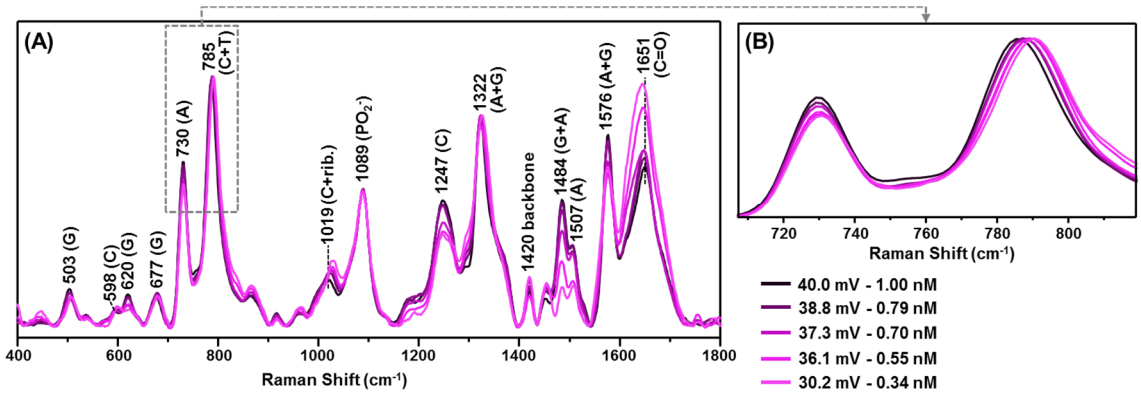

Figure 4. 4. (A) SERS spectra of ctDNA (final concentration 7.96 μg mL^{-1}) in AgSp colloids at different nanoparticle concentration and ζ potential. (B) Detail of the 710-820 cm^{-1} spectral region. The spectra were normalized to the phosphate band at ca. 1089 cm^{-1}. A general vibrational band assignment is also reported.[22,33] A = adenine, C = cytosine, T = thymine, G = guanine, Rib. = ribose, PO_2^- = phosphate group, (C=O) = carbonyl group.

The spectra were normalized to the phosphate stretching band at ca. 1089 cm^{-1}, whose large insensitivity to changes in DNA structure makes it an ideal candidate for an internal standard.[1,22,23,34,35] The spectral profile of ctDNA undergoes a progressive reshaping upon addition to gradually diluted colloids. Among others, it is worth highlighting the drop in intensity of the guanine ring deformation band at ca. 620 cm^{-1}, the red-shifts of the ring-breathing modes of adenine (ca. 730 cm^{-1}) and cytosine+thymine (785 cm^{-1}, main contribution from cytosine[33]), the intensity increase and large red-shift of the cytosine+ribose vibration at ca. 1019 cm^{-1} and the remarkable weakening of the cytosine ring stretching at ca. 1247 cm^{-1}. All these changes are fully consistent with the DNA base unstacking and unpairing transition.[1,22,36] Additionally, the broad composite carbonyl stretching band at ca. 1651 cm^{-1} (mainly ascribed to thymine) suffers a large shift to lower frequency as also observed during thermal denaturation of B-form DNA.[35] On the other hand, changes in ν(CO) band intensity are largely affected by the increasing relevance of the SERS background when the DNA

signal drops as a result of the nanoparticle dilution and, thus, such spectral alterations cannot be reliably associated with perturbations of the DNA structure. Similar spectral changes are registered in the SERS spectra of the short $dsDNA_{21}$ duplex (**Figure 4.5**).

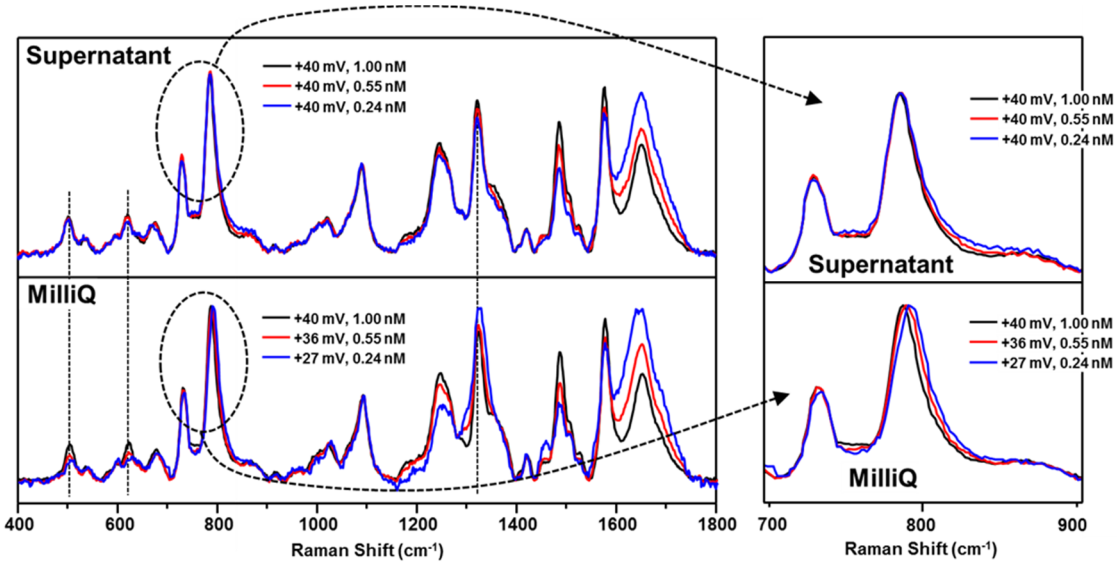

Figure 4. 5. SERS spectra of $dsDNA_{21}$ (final concentration 200 nM) in AgSp colloids at different nanoparticle concentration upon dilution with Milli-Q water or colloidal supernatant. Details of the corresponding 700-900 cm^{-1} spectral regions are illustrated on the right side of the figure.

Due to the particle size (ca. 22 nm diameter), the insertion of AgSp nanoparticles into the DNA grooves is hindered,[37,38] thus this process can be safely discarded as a possible driving cause of the strand separation. Contrarily, minor spectral changes were observed when the colloidal supernatant was employed to similarly dilute AgSp NPs (**Figure 4.5**) demonstrating the key role of the surface charge in determining the extension of the duplex unzipping.

It is also important to stress that the SERS profile of DNA-spermine complexes, formed by the interaction of the duplex with freely-spermine molecules in the bulk solution, differs drastically from that of DNA on AgSp colloids (**Figure 4.6**),[39] where the spermine molecules are restrained at the metal surface. This demonstrates that unbound spermine molecules in AgSp colloids do not play a significant role in shaping the final DNA SERS spectra and, thus, the spectral changes illustrated in **Figure 4.4** can be safely associated with strand separation.

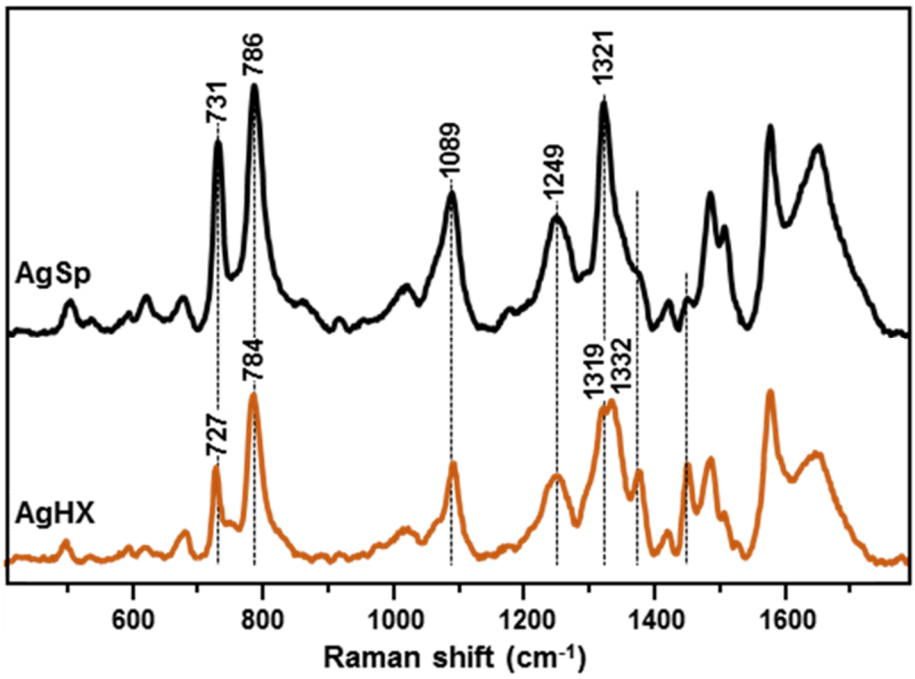

Figure 4. 6. SERS spectra of ctDNA (final concentration 7.5 μg mL^{-1}) on AgSp colloids and hydroxylamine-reduced silver colloids (AgHX).

As for AgSp, AgHX nanoparticles have a residual layer of chloride anions onto their surface that imparts particle stability via electrostatic repulsion (in this case, AgHX nanoparticles are negatively charged due to the lack of the extra spermine layer).[40] Contrary to AgSp colloids, negatively charged colloids such as AgHX do not clusterize upon DNA addition. Thus, SERS analysis of DNA with AgHX requires the use of an aggregating agent.[40,41] Spermine tetrahydrochloride ($SpCl_4$) can be employed as both DNA backbone neutralizer and aggregating agent for direct SERS detection of DNA in combination with AgHX colloids.[40,42] The illustrated SERS spectrum of ctDNA on AgHX is obtained by using $SpCl_4$ as the aggregating agent. Thus, it can be considered as the vibrational signature of the ctDNA-Sp complex formed in the bulk solution between the duplex and free-spermine molecules, while in the case of AgSp the duplex coordinates with spermine molecules restrained at the metal surface.[40] These results show striking differences in the final SERS spectral profiles, such as the blue-shifts of both A and C(+T) ring-breathing modes and the remarkable spectral reshaping observed in the 1300-1500 cm^{-1} spectral region.

The SERS spectra shown in **Figure 4.4** were obtained by adding a fixed amount of ctDNA to differently diluted AgSp colloids. This means that both

surface charge (correlated with the ζ potential) and DNA/NP ratios, which affects the degree of nanoparticle clustering, were modified at the same time. To isolate these variables and separately investigate their role in the duplex unzipping, two different SERS studies were performed: in the first one, the DNA/NP ratio was progressively varied while keeping the colloidal ζ potential constant; in the second study the effect of the nanoparticle surface charge on the spectral profile was monitored at fixed DNA/NP ratios. A short 21-mer single-stranded DNA ($ssDNA_{21}$) was included as probe molecule besides the long (ctDNA) and short ($dsDNA_{21}$) duplexes. Peak positions of the narrow and intense ring breathing bands at ca. 730 cm^{-1} and 785 cm^{-1}, ascribed to A and C+T nucleobases, respectively, were selected as spectral markers of the state of the DNA tertiary structure (**Figure 4.4B**).

4.3.4. The role of nanoparticle clustering

SERS and SPR analysis

In **Figure 4.7**, the peak frequencies of the spectral markers observed at different DNA/NP ratios (mg of DNA per nmol of NPs, in logarithmic scale) were plotted for four set of colloids at fixed surface charges (ζ potential equals to ca. 40.0 mV, 38.6 mV, 33.2 mV and 26.8 mV, respectively).

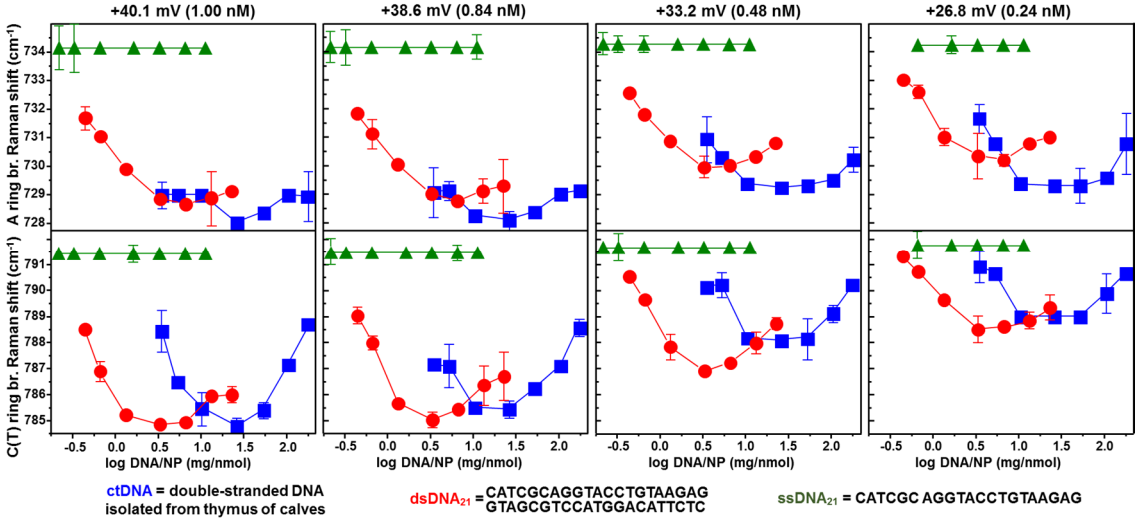

Figure 4. 7. Frequency shifts of adenine and cytosine (+thymine) ring breathing bands for SERS spectra of ctDNA, $dsDNA_{21}$ and $ssDNA_{21}$ acquired in AgSp colloids at fixed ζ potentials. For each batch of colloids, the DNA concentration, expressed as mg of analyte per nmol of nanoparticles (logarithmic scale), was progressively increased up to values that still yield detectable signals. Error bars equal to two standard deviations (N = 3).

The extension of the investigated ranges of DNA/NP ratios was defined by the acquisition of sufficiently intense and well-defined SERS spectra. At low DNA concentrations, restrictions are imposed by the overall number of scattering molecules in the sample. On the other hand, in the presence of an excess of analyte, DNA saturation of the nanoparticle surfaces prevents the formation of efficient hot spots (i.e., small number of hot spots in the sample). The results show that no spectral shifts were observed for $ssDNA_{21}$, whereas both short and genomic duplexes reveal notable changes in their spectral profiles (**Figure 4.8**), with the appearance of a frequency minimum at intermediate DNA/NP ratios, corresponding to the minimal perturbation of the double-helix stability by cationic nanoparticles of a specific ζ potential value. Overall, the position of such frequency minima moves to larger Raman shifts when the nanoparticle surface charge is decreased. It is also worth of noting that the peak frequencies of both A and C+T ring breathing bands consistently remain far below those of $ssDNA_{21}$, except when very low DNA/NP ratios are investigated in colloids with lowest surface charge (**Figure 4.7**, AgSp with ζ potential of +26.8 mV). These general observations are valid for both short and genomic DNA duplexes. On the contrary, for AgSp colloids at a given ζ potential, it was observed that minimal duplex separation (corresponding to the most blue-shifted ring breathing bands) always takes place at lower DNA/NP ratios for $dsDNA_{21}$ than ctDNA (**Figure 4.7**).

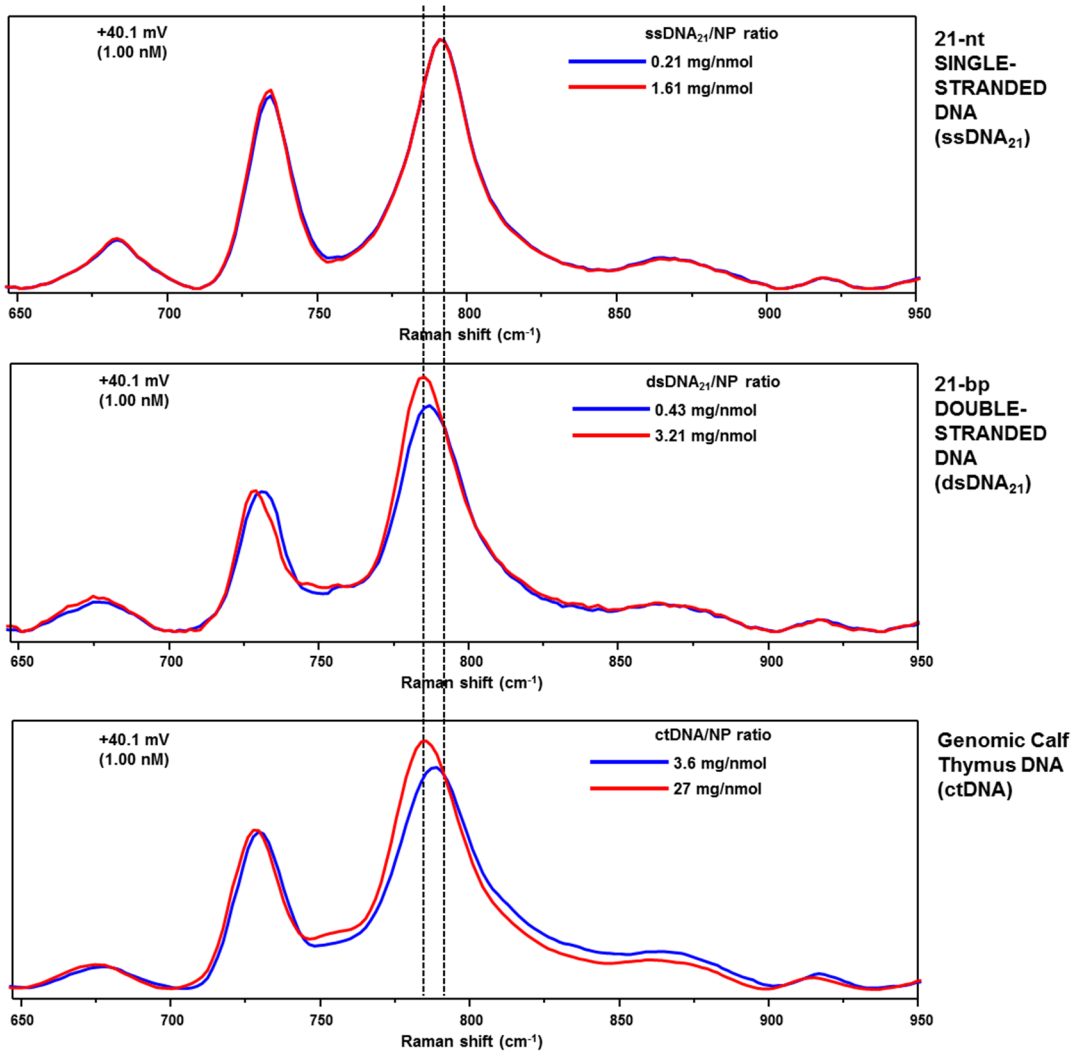

Figure 4. 8. Detail of SERS spectra of $ssDNA_{21}$ and $dsDNA_{21}$ in AgSp colloids at different DNA/NP ratios and fixed ζ potential (spectral region 645-950 cm^{-1}). The spectra were normalized to the phosphate band at ca. 1089 cm^{-1}.

Besides the obvious difference in length, $dsDNA_{21}$ and ctDNA deviate in nucleobase sequence and composition (GC-content of ca. 52.4% for short and ca. 41.9% for genomic DNA). To examine the role of these latter variables, the identical spectral analysis described in **Figure 4.7** was performed, but for two 22-bp duplexes either composed of CG or AT nucleobases (dsCG and dsAT, respectively, see **Figure 4.9**). Overall, the trends of peak frequency shifts for dsCG and dsAT largely match those of $dsDNA_{21}$ (**Figure 4.9**) indicating that, rather than base sequence and composition, the strand length parameter is likely to play the major role in determining the marked offset in double-strand unzipping for $dsDNA_{21}$ and ctDNA at different DNA/NP ratios (**Figure 4.7**). Given these results, questions arise as to which mechanisms lie behind the connection

between DNA/NP ratio factor and the characteristic changes in the tertiary structure of DNA duplexes electrostatically trapped at the interparticle junctions. To gain insights on this intriguing issue, detailed studies on the evolution of the optical properties of nanoparticle clusters in suspension as well as performed molecular dynamics (MD) simulations on model DNA-mediated clusters were undertaken.

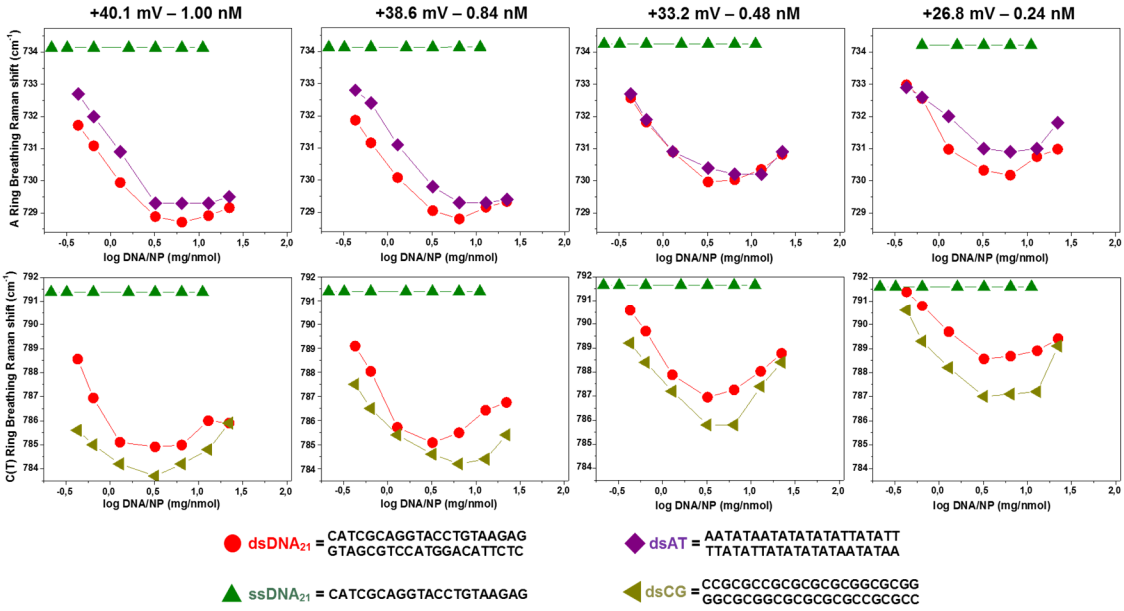

Figure 4. 9. Frequency shifts of adenine and cytosine (thymine) ring breathing bands for SERS spectra of $dsDNA_{21}$, $ssDNA_{21}$ and the base self-complementary double-stranded sequences dsCG and dsAT, acquired on AgSp colloids at different concentration/ ζ potential upon dilution with Milli-Q water. For each colloids, the DNA concentration, expressed as mg of analyte per nmol of nanoparticles (logarithmic scale), was progressively increased up to values that still yielded detectable SERS signals.

In addition to the large SERS enhancements localized at the interparticle gaps, the plasmonic coupling of interacting silver nanoparticles is responsible for the reshaping of the colloidal extinction profile with the appearance of new gap plasmon resonances red-shifted with respect to the LSPR.[43] However, the SERS enhancement distribution and far-field SPR responses from large ensembles of nanoparticle clusters have different spatial averaging properties, due to the different spatial localization of the plasmon resonances.[44,45] Thus, UV/Vis/NIR spectroscopy analysis of DNA-mediated aggregates can provide important complementary information on the correlation between strand separation, as revealed by SERS, and general geometrical features of nanoparticle clusters (i.e., gaps separation, size and shape).[29,43] **Figure 4.10A** displays the extinction

spectra of AgSp colloids ([NP] ca. 1.00 nM, ζ potential ca. + 40 mV) registered 60 min (red line) or 1 day (pink line) after the addition of increasing amounts of $dsDNA_{21}$.

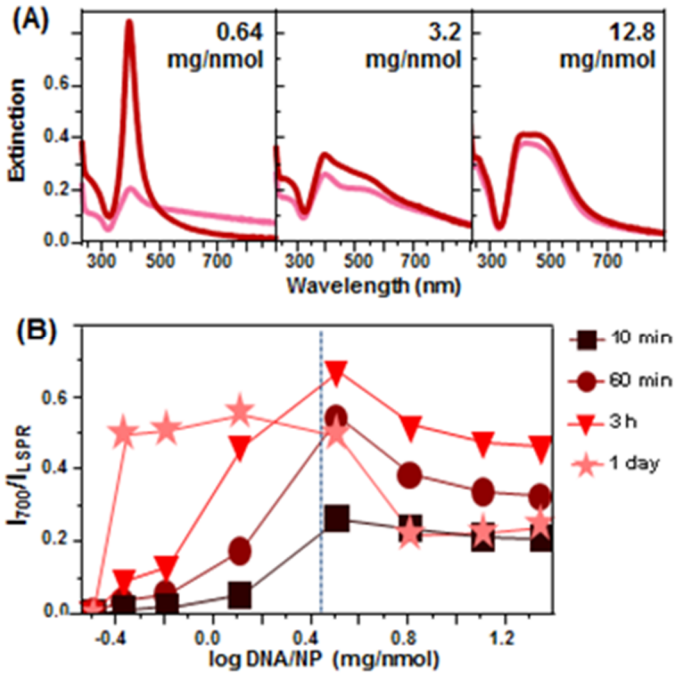

Figure 4. 10. (A) Extinction spectra of AgSp colloids ([NP] ca. 1.00 nM, ζ potential ca. + 40 mV) after the addition of different amounts of analyte, corresponding to ca. 0.64, 3.2 and 12.8 mg of $dsDNA_{21}$ per nmol of nanoparticles. The spectra were acquired 60 min and 1 day after the addition of $dsDNA_{21}$ to the colloids (red and pink curves, respectively). (B) Ratio of the extinction intensities at 700 nm over the intensity at the LSPR maximum (I_{700}/I_{LSPR}) against DNA/NP ratios (mg of $dsDNA_{21}$ per nmol of NP, in logarithmic scale). The intensity ratios were recorded at different time after the addition of the $dsDNA_{21}$ in the as-synthesized AgSp colloids. Aggregates sitting at the bottom of the Eppendorfs were briefly resuspended just before the optical measurement. The blue dotted lines broadly separate the lower and upper DNA/NP ratio ranges corresponding to the formation of unstable and stable clusters in suspension, respectively.

At low DNA/NP ratios (0.64 mg/nmol), a very mild nanoparticle aggregation after 60 min was observed, consistently with the small number of duplexes per nanoparticle that limits the extensive formation of DNA-mediated clusters. However, the perturbation introduced in the colloidal system eventually triggers further aggregation events that yield larger features with broader and weaker plasmonic contributions.[45] In fact, after one day, the particles undergo an irreversible coalescence which also leads to the visible deposition of films of silver nanoparticles at the Eppendorf tube surfaces. Differently, for higher $dsDNA_{21}$ concentrations, the colloidal system rapidly aggregates into stable clusters that can be easily redispersed after sedimentation. Notably, when DNA concentration

is further increased as much as to start saturating metallic surfaces, the extent of interparticle coupling decreases as revealed by the overall blue-shift of the gap plasmon resonances for DNA/NP ratio of 12.8 mg/nmol as compared to 3.2 mg/nmol (**Figure 4.10A**). The absorbance ratio at 700 nm and 391 nm (I_{700}/I_{LSPR}) was selected to better visualize the effect of time and DNA/NP ratio on the ensemble of gap-plasmon resonances (**Figure 4.10B**). Here, it was observed that, for DNA/NP ratios below ca. 2 mg/nmol (ca. 0.3 in the logarithmic scale), the duplex coverage of the silver surface is not sufficient to either induce extensive nanoparticle aggregation or impart long-term colloidal stability. In this regard, SERS analysis was also performed on each sample at 10 min, 60 min and 1 day, showing neither appreciable peak shifts of the spectral markers nor significant changes in absolute intensity over time. This suggests that the unspecific colloidal aggregation that follows the initial DNA-mediate cluster formation does not affect in a tangible way the final SERS profile. On the other hand, for DNA/NP ratios above ca. 3 mg/nmol (ca. 0.5 in the logarithmic scale), the rapid formation of stable clusters in suspension was observed. The extent of respective plasmon coupling appears to gradually decrease as the DNA/NP ratio is progressively raised (up to the largest DNA/NP value presented in this study).

The 60 min aged mixtures were also analyzed by DLS to extract the corresponding hydrodynamic size and size distribution of the DNA-mediated aggregates (**Figure 4.11A**). These samples were selected as they provide a close picture of the colloidal system at the equilibrium while largely avoiding the unspecific colloidal aggregation observed for low DNA/NP at longer time. Differently to what observed for the extinction ratio, the average hydrodynamic diameter of the aggregates shows a continuous increment with the increasing of the DNA content. On a purely qualitative basis, such trend can also be captured in SEM images of spin-coated samples (**Figure 4.11B-D**). This result directly entails that the decrease of the I_{700}/I_{LSPR} value observed for DNA/NP ratios larger than ca. 3 mg/nmol cannot be ascribed to a reduction of the cluster size but to an enlargement of the average gaps within nanoparticle aggregates. Here, when a large number of DNA molecules compete for adhesion on few surface sites, the surface crowding and the electrostatic repulsion between neighboring duplexes

hamper the necessary conformational changes required to maximize the number of contacting points with the surface.[26]

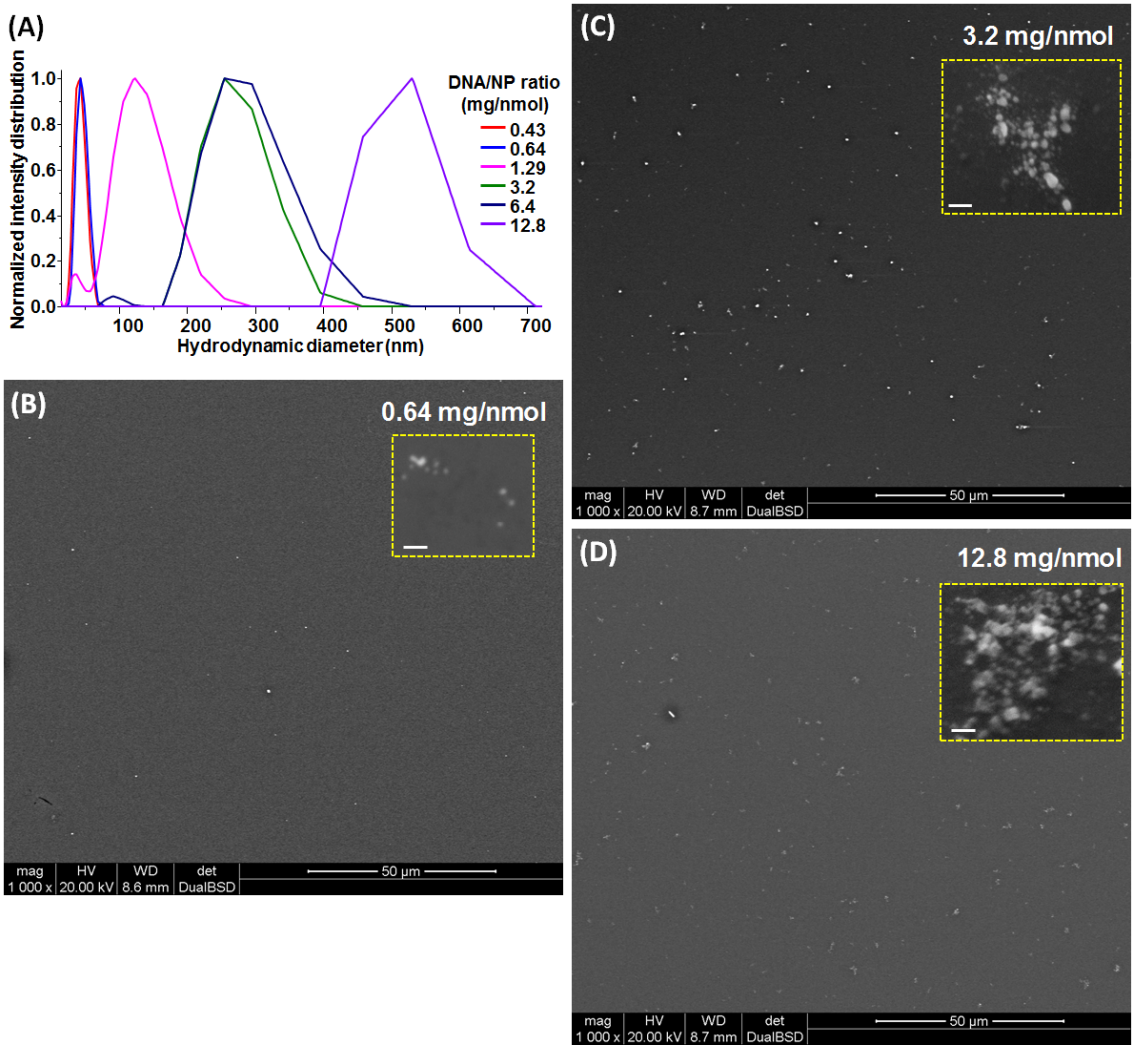

Figure 4. 11. (A) Size distribution (hydrodynamic diameter) of nanoparticle aggregates upon addition of increasing amount of $dsDNA_{21}$ corresponding to ca. 0.43, 0.64, 1.29, 3.2, 6.4 and 12.8 mg of $dsDNA_{21}$ per nmol of nanoparticles. (B, C, D) Representative ESEM images of colloidal samples 0.64, 3.2 and 12.8 mg of $dsDNA_{21}$ per nmol of nanoparticles deposited on silicon wafers via spin-coating to minimize drying-induced aggregation. Silicon wafers (1 cm ×1 cm) were cleaned by standard RCA-1 to remove any possible organic residue. In order to achieve a low particle density, 80 µL of each sample were spin coated at different speeds. A 1st ramp at 500 rpm during 10 s and a 2nd ramp at 3000 rpm for 30 s were used (the acceleration rate used for both ramps was 500 rpm s^{-1}). Insets: high magnification ESEM images of representative colloidal aggregates. The scale bar represents 200 nm.

Thus, it can be reasonably expected that, instead of homogeneously extending over the metallic surface, DNA molecules bind the silver surface adopting a broad set of tilted conformations which lead to larger interparticle separations in aggregates. This picture is fully consistent with previous molecular dynamic simulations which described the DNA adsorption on a spermine-bound

silver surface as a multistep process.[23] According to this mechanism, after a fast recognition phase, the total adhesion of short DNA strands is achieved by conformational changes triggered by electrostatic interactions with spermine molecules adsorbed on the surface. This second step can be hindered by an overcrowded silver surface and/or without the necessary amount of free spermine molecules, thus leading to aggregates characterized by properly adsorbed duplexes coexisting with partly bound DNA molecules.

The evolution of the DNA-driven nanoparticle clusterization was also investigated for ctDNA (**Figure 4.12**). The semi-quantitative analysis of the extinction spectra did reveal minimal interparticle plasmonic coupling at very low or very high ctDNA concentrations, but it was not possible to discern any further distinctive pattern. Most likely, this is the consequence of the coexistence of many additional aggregation routes. Oppositely to what happens for the adsorption of ca. 7 nm rod-like duplexes on AgSp nanoparticles, in the case of long genomic DNA the silver particles are the nanoscale objects that accumulate at the duplex chain, leading to the progressive compaction of the elongated coil which can also involve the wrapping of the chain around individual nanospheres.[46,47] Such compaction process consists of several intermediate states with uneven distributions of nanoparticles along the chain.[46,47] Furthermore, nanoparticles in suspension tend to agglomerate at the surfaces of other nanoparticles previously coordinated to the genomic strand.[46]

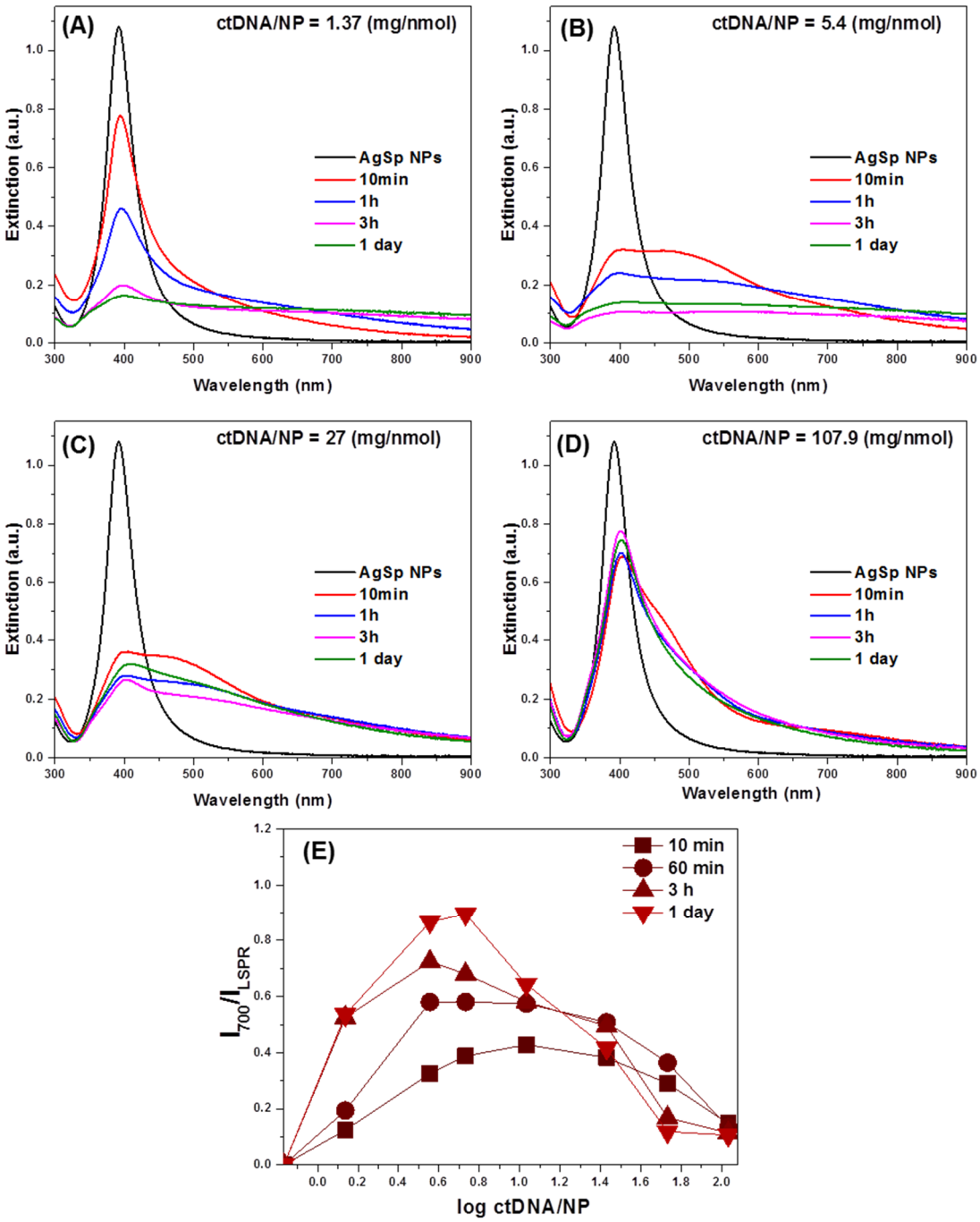

Figure 4. 12. (A-D) Extinction spectra of AgSp colloids ([NP] ca. 1.00 nM, ζ potential ca. + 40 mV) before and after the addition of different amounts of analytes, corresponding to ca. (A) 1.37, (B) 5.4 and (C) 27 and (D) 107.9 mg of ctDNA per nmol of nanoparticles. The spectra were acquired 10 min, 60 min, 3 hours and 1 day after the addition of ctDNA to the colloids (E) Ratio of the extinction intensities at 700 nm over the intensity at the LSPR maximum (I_{700}/I_{LSPR}) against DNA/NP ratios (mg of ctDNA per nmol of NP, in logarithmic scale). The intensity ratios were recorded at different time after the addition of the ctDNA in the undiluted AgSp colloids. Aggregates sitting at the bottom of the Eppendorfs were briefly resuspended just before the optical measurement. Extinction spectra of AgSp colloids at a different time upon addition of increasing amounts of ctDNA were acquired for samples prepared in the same way as for SERS analysis.

The antithetical role played by DNA of different chain lengths on the nanoparticle aggregation pattern (i.e.; nanoparticles collect short dsDNA$_{21}$ at their surfaces vs. long genomic ctDNA collects nanoparticles at the duplex chain) is also well-reflected in the UV-Vis analysis of the colloidal supernatants upon removal of DNA-mediated clusters (**Figure 4.13**).

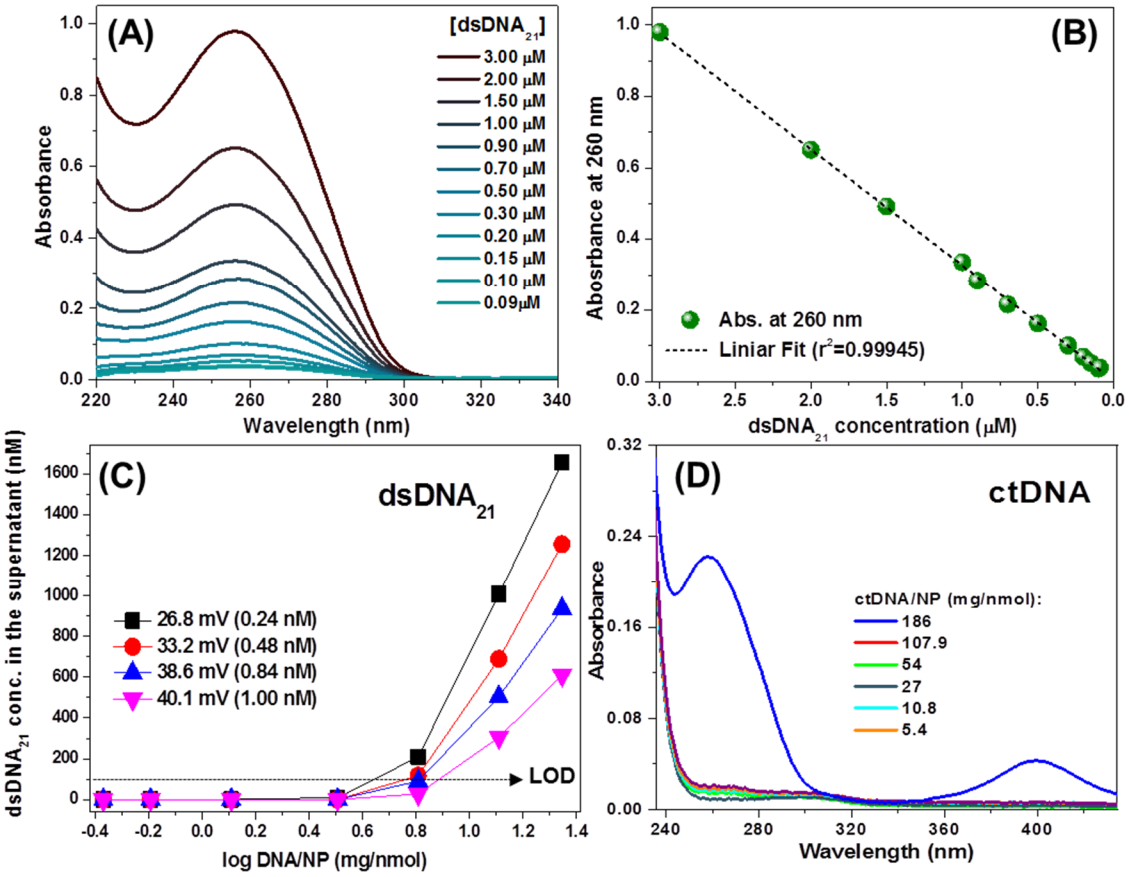

Figure 4. 13. (A) Absorption spectra of dsDNA$_{21}$ buffer solutions at different concentrations. (B) Absorbance at 260 nm vs. dsDNA$_{21}$ concentration. The values correspond to the data illustrated in (A). (C) dsDNA$_{21}$ concentration in the supernatants of AgSp colloids at different ζ potential and dsDNA$_{21}$/NP ratios (logarithmic scale). The dsDNA-induced aggregates were left to deposit overnight before separating the supernatant. In the case of the samples with log dsDNA$_{21}$/NPs ratios below 0, an additional centrifugation step (13K rpm, 40 min) was necessary prior to the analysis to remove large amounts of suspended nanoparticles that remained in the supernatant. (D) Absorption spectra of ctDNA+NPs mixture supernatants for different ctDNA/NP ratios on non-diluted AgSp colloids (+40.1 mV; 1.00 nM). Only the sample with the highest ratio (i.e., the lowest number of nanoparticles per strand) shows residual ctDNA in suspension (see absorbance at 260 nm) with additional contribution from silver nanoparticles (see weak plasmon band at ca. 398 nm).

Monitoring of the optical absorption of DNA at 260 nm reveals that a progressively higher concentration of unbound dsDNA$_{21}$ is present in the supernatant for DNA/NP ratio above ca. 3 mg/nmol (ca. 0.5 in the logarithmic scale, see **Figure 4.13C**), which precisely corresponds to the stability threshold

for $dsDNA_{21}$-driven nanoparticle assemblies (i.e.; when the metallic surfaces are largely saturated with short duplexes that act in this situation also as stabilizing ligands). Notably, unbound $dsDNA_{21}$ in the supernatant are observed for AgSp colloids with higher ζ potential, which indicates that duplex surface density increases with the nanoparticle surface charge. On the other hand, in the case of ctDNA, residual duplexes in the supernatant are only detected for the largest DNA/NP ratio (**Figure 4.13D**) together with a weak additional band at ca. 398 nm ascribable to very sparse individual nanoparticles attached to the chain. For all ctDNA/NP ratio below that value, the relatively high weight of the ctDNA-nanoparticle complexes leads to sedimentation. In all cases, the DNA concentration in the sample was calculated according to the traditional equation:

$$\text{DNA conc. } (\mu g/mL) = (A_{260} - A_{320}) \times 50 \times \text{dilution factor} \qquad (4.1)$$

Molecular dynamic simulations

The illustrated SERS and far-field SPR data are the highly averaged responses of very complex samples containing a large number of polydispersed aggregates. Modelling systems of such size and complexity is, at present, unfeasible. Nonetheless, MD-based simulations of model DNA-mediated clusters may give a hint of the potential connection between the cluster geometrical features and the perturbation of the interacting DNA at the junctions. In particular, two model systems were envisioned: a dimer (2NP) and a trimer (3NP) with a compact geometry (see **Figure 4.14A**), as the simplest prototypes of small and larger aggregates, respectively. Both models included a single $dsDNA_{21}$ molecule adopting an extended conformation at the interface of each gap.

In **Figure 4.15**, the free energy surfaces calculated as function of the separation between nanoparticles and the average distance between base pairs belonging to different DNA strands are shown. In both 2NP and 3NP systems, the deepest minima corresponded to states showing the double-helix of DNA in the B-form. Specifically, in the 2NP cluster model, the global minimum was found at the relatively large interparticle distance of about 29 Å (**Figure 4.15A**). Conversely, in the trimer model the most stable state was located at much narrower separations (24 – 25 Å, **Figure 4.15B**). This finding clearly indicates a

trend, whereby smaller aggregates tend to stretch, or at least to easily interconvert between states of different contraction, while more compact clusters are highly preferred in the case of larger aggregates. This effect can be explained through a DNA-mediated binding cooperativity between the three nanoparticles that is missing in the 2NP model.

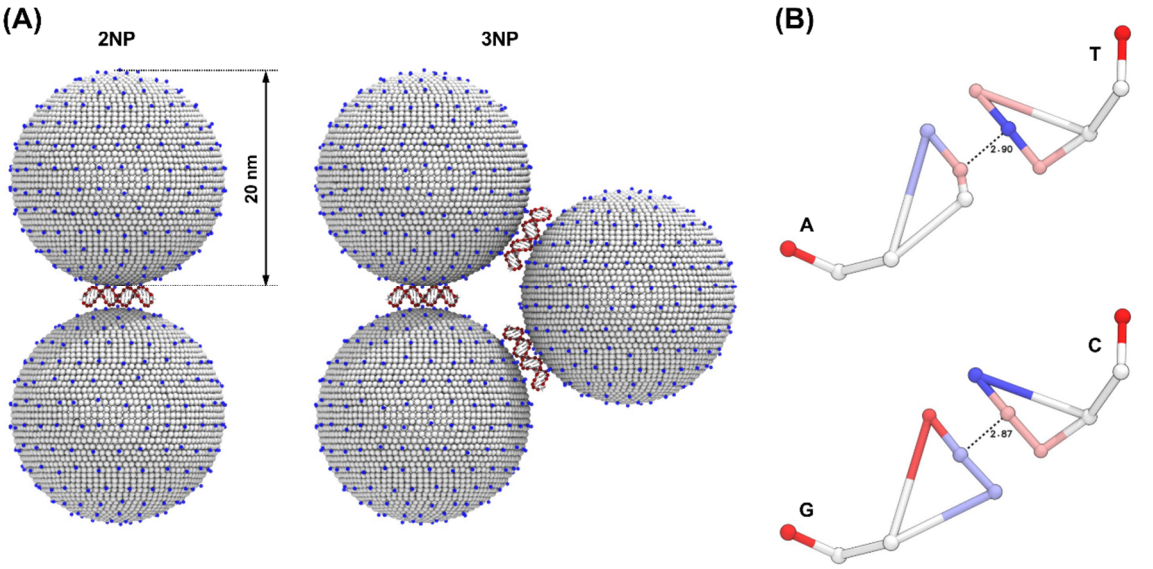

Figure 4. 14. (A) 2NP and 3NP systems employed in MD-based simulations to model smaller and larger DNA-NP cluster aggregates, respectively. The positively charged nanoparticle is described with a two-layered sphere. Positively charged beads mimicking the headgroups of spermine molecules are represented as blue spheres that are evenly distributed over a spherical surface of uncharged beads (white spheres). A coarse-grained model of $dsDNA_{21}$ is also shown at each interparticle junction (red strands). (B) Coarse-grained representation of complementary base pairs (Adenine/Thymine, top, and Guanine/Cytosine, bottom) according to the force-field employed in this work. The beads are color coded according to their partial charge (red: negative, and blue: positive). The equilibrium distance between the central beads of paired nucleobases is also shown. Notably, these distances were also used to describe the strand separation of the DNA duplex in metadynamics simulations.

Most importantly, however, is that the investigated systems show a remarkably different behavior along the reaction coordinate describing the separation between the two strands of the duplex. Indeed, an incipient unzipping could be observed in the 2NP system, as it can be assessed by the multiple minima located in the free energy surface at strand separations greater than 5 Å. This behavior is only marginally found in the 3NP model, most likely as a consequence of the cluster aggregate compaction that hinders the double strand unzipping.

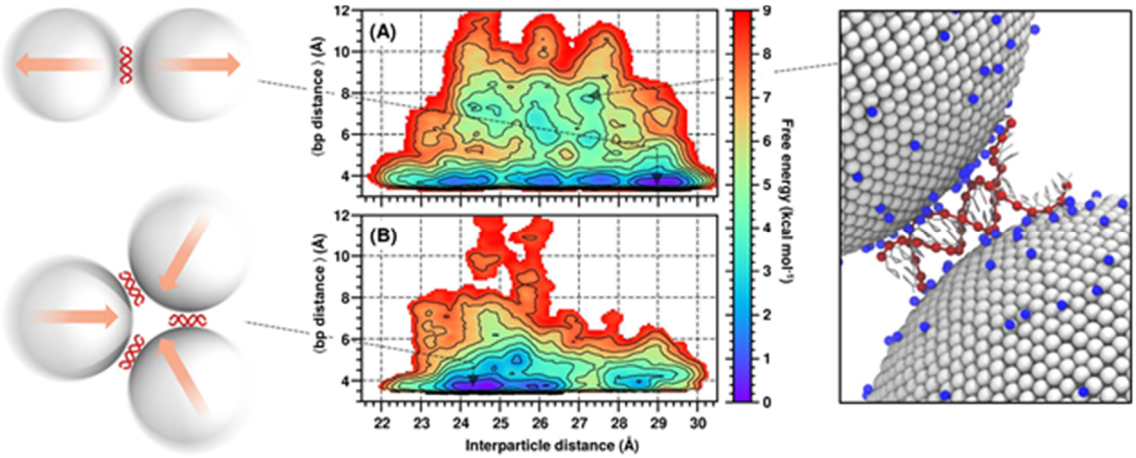

Figure 4. 15. Free energy surfaces computed as a function of the interparticle distance and the average distance between complementary base pairs for 2NP and 3NP model systems (A and B panel, respectively). Iso-lines are plotted with a step of 1 kcal mol^{-1}. Pictorial representations of the mechanical features of the cluster aggregates, and a representative configuration showing partial DNA unzipping extracted from MD-based simulations, are also shown (left and right panels, respectively).

Taken as a whole, the outcome of MD simulations suggests that the different size and geometrical features of DNA-mediated clusters play indeed an important role in determining the structural features of the duplex at the gaps. This provides a new tool for interpreting the experimental trends illustrated in **Figure 4.7** and **4.10**. On these bases, the following can be proposed. Minimal strand separation is fulfilled at intermediate DNA/NP values when cluster aggregate compaction is maximized. However, when DNA concentration is low, molecules extend homogenously over the metallic surface and cluster compaction is improved only by increasing the number of nanoparticle per aggregate. On the other hand, for large DNA/NP ratios, cluster compaction diminishes as a result of the increased separation between nanoparticles imposed by reorientation of the DNA molecules over the silver surfaces.

4.3.5. The role of nanoparticle surface charge

Based on the outcome of the data illustrated in **Figure 4.7**, the DNA/NP ratios associated with minimal duplex perturbation (ca. 14 mg/nmol for ctDNA, 3.2 mg/nmol for $dsDNA_{21}$) were maintained fixed, while monitoring the C+T ring breathing peak position on nanoparticles at decreasing surface charge (**Figure 4.16**). In this case, short and genomic duplexes share the same qualitative behavior, presenting a jump in peak frequency for ζ potential values in the ca. 30-35 mV range. An identical result was observed for the A spectral marker.

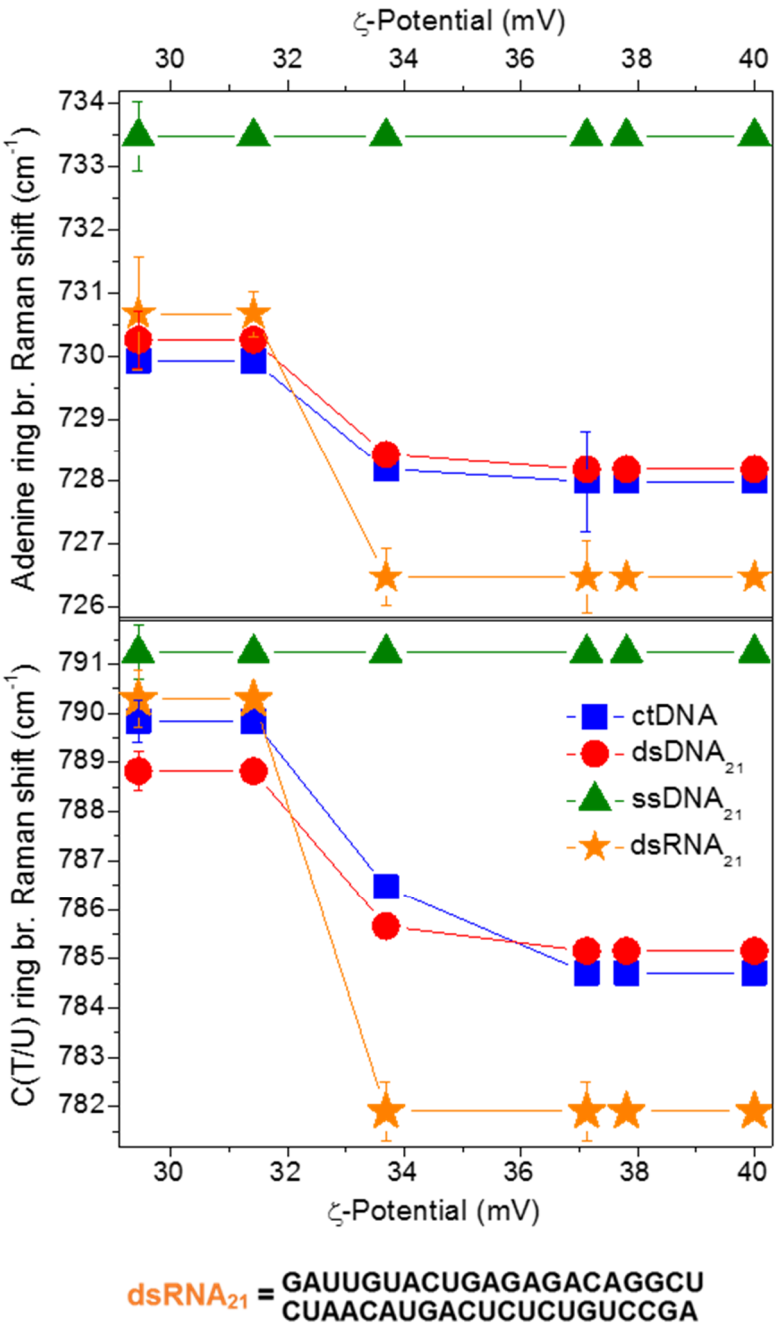

Figure 4. 16. Frequency shifts of adenine and cytosine (+thymine/uracyl) ring breathing bands for SERS spectra of ctDNA, $dsDNA_{21}$, $dsRNA_{21}$ and $ssDNA_{21}$ acquired in AgSp colloids (at fixed DNA(RNA)/NP ratio) and different ζ potential. DNA/NP ratio was kept constant to 14 mg/nmol for ctDNA, 3.2 mg/nmol for $dsDNA_{21}$ and $dsRNA_{21}$, and 1.6 mg/nmol for $ssDNA_{21}$.

The same study was further extended to a 21-bp RNA duplex ($dsRNA_{21}$) which, in addition to nucleobase sequence and composition, differs from dsDNA also by the helix geometry (mainly B-form for $dsDNA_{21}$ and A-form for $dsRNA_{21}$) and the sugar molecular structure.[1] Despite the structural differences, the SERS data indicate that the spectral shift dependency of $dsRNA_{21}$ from the colloidal

surface charge is qualitatively analogue to those of short and long DNA duplexes (**Figure 4.16**). Thus, when the cluster geometry variable, which is strictly correlated to the chain length, is removed by fixing the DNA/NP ratios at the minimal double-helix perturbation, the differences of spectral behavior for short and genomic duplexes are largely levelled out. A possible explanation may be found in the electrostatic nature of the DNA/NP interaction. dsDNA initially adsorbs onto a nanoparticle, then screens its positive charge thereby favoring the subsequent approaching of a second nanoparticle to generate the corresponding interparticle junction. As previously simulated by means of MD methods,[23] the duplex binding onto the first nanoparticle occurs on the nanosecond time scale, where the flexibility of the surface spermine molecules contributes to promoting the optimum interaction with the phosphate groups aligned along the DNA backbone. On the other hand, the second approaching nanoparticle “sees” a duplex whose degrees of freedom are largely reduced due to the interaction with the solid phase. Thus, one can speculate that such second DNA-NP interaction could occur to the detriment of the duplex stability, especially when the spermine surface density is decreased below a critical level (i.e., when the ζ potential is lowered). Under this scenario, no significant differences are expected to be revealed by the SERS signal of duplexes with different lengths, since their SERS spectra largely result from the contribution of chain fragments with similar size (limited by the hot spot volume) and carrying equally spaced phosphate groups on the DNA backbone.

4.4. Conclusions

In summary, the outcomes of the SERS analysis can be summarized as follows. Overall, the results indicate that the interaction of the cationic nanoparticles with double-stranded DNA leads to (at least partial) strand separation of dsDNA population that molecularly mediate the nanoparticle clustering (i.e., DNA molecules at the interparticle junctions). The extent of such structural deformation is highly dependent on (i) the DNA/NP ratio and (ii) the nanoparticle surface charge. The former parameter directly affects the aggregation profile which is, in turn, strictly related to the length of the duplex (whereas base composition did not appear here to play a relevant role). Regardless of the chain length, it was possible to recognize a qualitatively common trend where unzipping of the double helixes is progressively maximized at high and low DNA/NP ratios, for a given ζ potential. The potential correlation between the aggregation features of a DNA-mediated cluster and the tendency of the DNA molecule trapped at the interparticle gap to undergo unzipping was further investigated and confirmed by molecular dynamics in combination with additional SPR analysis. Differently, once fixed the DNA/NP ratio (i.e., the degree of aggregation) to a value corresponding to the minimal duplex perturbation and monitored SERS spectra for different nanoparticle surface charge, a sudden transition from a dominant duplex conformation to mainly separated strands below a critical ζ potential threshold is observed. This transition appears to be largely independent not only from nucleobase composition but also from the chain length and double helical geometry. This chapter provides new fundamental insights into the interaction between nucleic acids and nanoparticles, and how the integrity of the double-helical structure is perturbed by the cooperative binding of nano-objects.

4.5. References

(1) Morla-Folch, J.; Xie, H.-n.; Alvarez-Puebla, R. A.; Guerrini, L. *ACS Nano* **2016**, *10*, 2834.
(2) Pérez, A.; Lankas, F.; Luque, F. J.; Orozco, M. *Nucleic Acids Research* **2008**, *36*, 2379.
(3) Potoyan, D. A.; Savelyev, A.; Papoian, G. A. *Wiley Interdisciplinary Reviews: Computational Molecular Science* **2013**, *3*, 69.
(4) Zeida, A.; Machado, M. R.; Dans, P. D.; Pantano, S. *Physical Review E* **2012**, *86*, 021903.
(5) Dans, P. D.; Zeida, A.; Machado, M. R.; Pantano, S. *Journal of Chemical Theory and Computation* **2010**, *6*, 1711.
(6) Prates Ramalho, J. P.; Gkeka, P.; Sarkisov, L. *Langmuir* **2011**, *27*, 3723.
(7) Gkeka, P.; Sarkisov, L.; Angelikopoulos, P. *The Journal of Physical Chemistry Letters* **2013**, *4*, 1907.
(8) Smith, N.; Campbell, B.; Li, L.; Li, C.; Alexov, E. *BMC Structural Biology* **2012**, *12*, 1.
(9) Van Lehn, R. C.; Alexander-Katz, A. *Soft Matter* **2011**, *7*, 11392.
(10) Barducci, A.; Bussi, G.; Parrinello, M. *Physical Review Letters* **2008**, *100*, 020603.
(11) Branduardi, D.; Bussi, G.; Parrinello, M. *Journal of Chemical Theory and Computation* **2012**, *8*, 2247.
(12) Phillips, J. C.; Braun, R.; Wang, W.; Gumbart, J.; Tajkhorshid, E.; Villa, E.; Chipot, C.; Skeel, R. D.; Kalé, L.; Schulten, K. *Journal of Computational Chemistry* **2005**, *26*, 1781.
(13) Tribello, G. A.; Bonomi, M.; Branduardi, D.; Camilloni, C.; Bussi, G. *Computer Physics Communications* **2014**, *185*, 604.
(14) Onufriev, A.; Bashford, D.; Case, D. A. *The Journal of Physical Chemistry B* **2000**, *104*, 3712.
(15) Onufriev, A.; Bashford, D.; Case, D. A. *Proteins: Structure, Function, and Bioinformatics* **2004**, *55*, 383.
(16) Decherchi, S.; Masetti, M.; Vyalov, I.; Rocchia, W. *European Journal of Medicinal Chemistry* **2015**, *91*, 27.
(17) Pastor, R. W.; Brooks, B. R.; Szabo, A. *Molecular Physics* **1988**, *65*, 1409.
(18) Maier, J.; Traenkle, B.; Rothbauer, U. *Scientific Reports* **2015**, *5*, 13402.
(19) Brown, M. A.; Goel, A.; Abbas, Z. *Angewandte Chemie - International Edition* **2016**, *55*, 3790.
(20) Yguerabide, J.; Yguerabide, E. E. *Anal. Biochem.* **1998**, *262*, 137.
(21) Yguerabide, J.; Yguerabide, E. E. *Anal. Biochem.* **1998**, *262*, 157.
(22) Guerrini, L.; Krpetić, Ž.; van Lierop, D.; Alvarez-Puebla, R. A.; Graham, D. *Angew. Chem.-Int. Edit.* **2015**, *54*, 1144.
(23) Masetti, M.; Xie, H.-n.; Krpetic, Z.; Recanatini, M.; Alvarez-Puebla, R. A.; Guerrini, L. *Journal of the American Chemical Society* **2015**, *137*, 469.
(24) Estevez-Torres, A.; Baigl, D. *Soft Matter* **2011**, *7*, 6746.
(25) Nash, J. A.; Singh, A.; Li, N. K.; Yingling, Y. G. *ACS Nano* **2015**, *9*, 12374.
(26) Zhang, X.; Servos, M. R.; Liu, J. *Langmuir* **2012**, *28*, 3896.
(27) Aroca, R. *Surface-enhanced Vibrational Spectroscopy*; John Wiley & Sons, Chichester, 2006.

(28) Kleinman, S. L.; Sharma, B.; Blaber, M. G.; Henry, A. I.; Valley, N.; Freeman, R. G.; Natan, M. J.; Schatz, G. C.; Van Duyne, R. P. *Journal of the American Chemical Society* **2013**, *135*, 301.
(29) Le Ru, E. C.; Etchegoin, P. G. *Principles of Surface-Enhanced Raman Spectroscopy*, 2009.
(30) Le Ru, E. C.; Etchegoin, P. G.; Meyer, M. *J. Chem. Phys.* **2006**, *125*, 204701.
(31) Bera, S. C.; Sanyal, K.; Senapati, D.; Mishra, P. P. *The Journal of Physical Chemistry B* **2016**, *120*, 4213.
(32) Pfeiffer, C.; Rehbock, C.; Hühn, D.; Carrillo-Carrion, C.; de Aberasturi, D. J.; Merk, V.; Barcikowski, S.; Parak, W. J. *Journal of The Royal Society Interface* **2014**, *11*.
(33) Morla-Folch, J.; Xie, H.-n.; Gisbert-Quilis, P.; Gómez-de Pedro, S.; Pazos-Perez, N.; Alvarez-Puebla, R. A.; Guerrini, L. *Angewandte Chemie International Edition* **2015**, *54*, 13650.
(34) Xu, L.-J.; Lei, Z.-C.; Li, J.; Zong, C.; Yang, C. J.; Ren, B. *Journal of the American Chemical Society* **2015**, *137*, 5149.
(35) Duguid, J. G.; Bloomfield, V. A.; Benevides, J. M.; Thomas, G. J. *Biophysical Journal* **1996**, *71*, 3350.
(36) Movileanu, L.; Benevides, J. M.; Thomas, G. J. *Biopolymers* **2002**, *63*, 181.
(37) Rivera Gil, P.; Hühn, D.; del Mercato, L. L.; Sasse, D.; Parak, W. J. *Pharmacological Research* **2010**, *62*, 115.
(38) Pan, Y.; Neuss, S.; Leifert, A.; Fischler, M.; Wen, F.; Simon, U.; Schmid, G.; Brandau, W.; Jahnen-Dechent, W. *Small* **2007**, *3*, 1941.
(39) Torres-Nunez, A.; Faulds, K.; Graham, D.; Alvarez-Puebla, R. A.; Guerrini, L. *Analyst* **2016**, *141*, 5170.
(40) Torres-Nuñez, A.; Faulds, K.; Graham, D.; Alvarez-Puebla, R. A.; Guerrini, L. *Analyst* **2016**.
(41) Papadopoulou, E.; Bell, S. E. J. *Angew. Chem.-Int. Edit.* **2011**, *50*, 9058.
(42) Wu, C. Y.; Lo, W. Y.; Chiu, C. R.; Yang, T. S. *J. Raman Spectrosc.* **2006**, *37*, 799.
(43) Giannini, V.; Fernandez-Dominguez, A. I.; Heck, S. C.; Maier, S. A. *Chemical Reviews* **2011**, *111*, 3888.
(44) Le Ru, E. C.; Galloway, C.; Etchegoin, P. G. *Physical Chemistry Chemical Physics* **2006**, *8*, 3083.
(45) Guerrini, L.; McKenzie, F.; Wark, A. W.; Faulds, K.; Graham, D. *Chem. Sci.* **2012**, *3*, 2262.
(46) Zinchenko, A. A.; Sakaue, T.; Araki, S.; Yoshikawa, K.; Baigl, D. *The Journal of Physical Chemistry B* **2007**, *111*, 3019.
(47) Zinchenko, A. A.; Yoshikawa, K.; Baigl, D. *Physical Review Letters* **2005**, *95*, 228101.

UNIVERSITAT ROVIRA I VIRGILI
OPTICAL DETECTION AND STRUCTURAL ANALYSIS OF DNA VIA DIRECT SURFACE-ENHANCED RAMAN SCATTERING
Patricia Gisbert Quilis

UNIVERSITAT ROVIRA I VIRGILI
OPTICAL DETECTION AND STRUCTURAL ANALYSIS OF DNA VIA DIRECT SURFACE-ENHANCED RAMAN SCATTERING
Patricia Gisbert Quilis

GENERAL CONCLUSIONS

In the framework of this dissertation, a novel approach based on surface-enhanced Raman scattering (SERS) for the label-free optical detection and structural analysis of nucleic acids was implemented. The method relies on the use of positively-charged silver nanoparticles as plasmonic substrates for SERS analysis of DNA in solution. This strategy was successfully applied for the sensitive detection of clinically relevant point mutations in the *K-Ras* gene, which are routinely screened for diagnostic purposes, especially in colorectal cancer. Along this study, the impact of the cationic nanoparticles on the structural features of the interacting DNA molecules was extensively investigated. In summary:

I. AgSp NPs were implemented as efficient SERS substrates for the amplification of the Raman signal of nucleic acids. DNA adsorption onto the metallic particles takes place via electrostatic interaction between the phosphate groups and the positive charges at the surface of the NPs. This directly leads to the formation of stable clusters in suspension yielding very intense and reproducible SERS spectra obtained under an average SERS regime. The acquired spectra are truly vibrational representations of the composition and conformation of DNA molecules. As a result, detailed structural information can be extracted from the SERS spectrum of DNA by analyzing characteristic and well-defined spectral markers. Also, the protocol for the optimization of the experimental parameters in SERS measurements was described.

II. The optimized direct SERS approach was successfully applied to the detection of oncogenic *K-Ras* point mutations in 141-nt sequences, with single base sensitivity. The sensing strategy exploited the concept of single strand conformation polymorphism (SSCP) where point mutations induce conformational changes in the single-stranded sequences (ssDNAs), which were detected in the SERS spectra and unambiguously classified via chemometric methods (PLS-DA). Further, these results were supported by theoretical simulations. Overall, the findings showed the potential of this technique for sensitive, fast and inexpensive detection of point mutations in long ssDNAs. Importantly, this method not only

overcame the intrinsic limitation of previously reported SERS methods, but also simplified the sensing scheme with respect to SSCP analysis.

III. The intrinsic nature of the SERS method, combined with SPR spectroscopy and theoretical simulations, unlocked the possibility of selectively examine the impact of nanoparticle clustering on different nucleic acid duplexes (dsDNA) over a wide degree of colloidal aggregation and without the need of external intercalating dyes or strand labeling. The results showed that the interaction of AgSp NPs with dsDNA, trapped at the interparticle junctions, can lead to (at least partial) strand separation. The extent of the structural impact was mainly defined by two variables: the DNA/NP ratio and the nanoparticle surface charge. For a given NP charge (characterized by ζ potential) unzipping of the double helixes was maximized at high and low DNA/NP ratios. On the other hand, when the DNA/NP ratio corresponding to the minimal duplex deformation was fixed and the ζ potential varied, it was observed a threshold above which separated strands exist as the dominant conformation. Such change in conformation was found to be independent on chain length, nucleobase composition or duplex structure.

Overall, this dissertation is meant to contribute to the establishment of SERS as a mature technique for the direct analysis and screening of nucleic acids. Accordingly, the research work presented shows the analytical potential of SERS both as sensitive tool for fast and low-cost analyses of nucleic acids, and as a valuable technique for investigating the interaction of nucleic acids and cationic nanoparticles.

UNIVERSITAT ROVIRA I VIRGILI
OPTICAL DETECTION AND STRUCTURAL ANALYSIS OF DNA VIA DIRECT SURFACE-ENHANCED RAMAN SCATTERING
Patricia Gisbert Quilis

UNIVERSITAT ROVIRA I VIRGILI
OPTICAL DETECTION AND STRUCTURAL ANALYSIS OF DNA VIA DIRECT SURFACE-ENHANCED RAMAN SCATTERING
Patricia Gisbert Quilis

APPENDIX I - LIST OF FIGURES

APPENDIX II - LIST OF TABLES

APPENDIX III - LIST OF PUBLICATIONS

Gisbert-Quilis P., Masetti M., Morla-Folch J., Fitzgerald J. M., Pazos-Perez N., Garcia-Rico E., Giannini V., Alvarez-Puebla R.A. Guerrini L. *The Structure of Short and Genomic DNA at the Interparticle Junctions of Cationic Nanoparticles.* **Advanced Materials Interfaces** (**2017**).

Gisbert-Quilis P., Morla-Folch J., Masetti M., Garcia-Rico E., Alvarez-Puebla R.A. and Guerrini L. *Conformational SERS classification of K-Ras point mutations for cancer diagnostics.* **Angewandte Chemie-International Edition** (**2017**).

Mir-Simon B., Morla-Folch J., Gisbert-Quilis P., Pazos-Perez N., Xie H.-n., Bastús N. G., Puntes V., Alvarez-Puebla R. A., Guerrini L.*SERS Efficiencies of Micrometric Polystyrene Beads Coated with Gold and Silver Nanoparticles: The Effect of Nanoparticle Size.* **Journal of Optics** (**2015**).

Morla-Folch, J., Xie, H.-n., Gisbert-Quilis, P., Pedro, S. G.-d., Pazos-Perez, N., Alvarez-Puebla, R. A., and Guerrini, L. *Ultrasensitive Direct Quantification of Nucleobase Modifications in DNA by Surface-Enhanced Raman Scattering: The Case of Cytosine.* **Angewandte Chemie-International Edition** (**2015**).

UNIVERSITAT ROVIRA I VIRGILI
OPTICAL DETECTION AND STRUCTURAL ANALYSIS OF DNA VIA DIRECT SURFACE-ENHANCED RAMAN SCATTERING
Patricia Gisbert Quilis

ACKNOWLEDGEMENTS

Amb aquesta tesi doctoral acabe una etapa, que no sempre ha sigut fàcil. Durant aquests anys, he après molt de totes aquelles persones que m'han acompanyat i per això m'agradaria donar les gràcies a totes elles.

Primer que tot voldria agrair al Prof. Ramón A. Álvarez Puebla i al Dr. Luca Guerrini per la oportunitat de treballar al seu grup i per la seva guia, dedicació i esforç.

Al grup, pels bons moments que hem viscut i per haver compartit amb vosaltres aquesta etapa. A Arnau per fer-nos riure i mantenir sempre la dispensa del l'oficina plena, a Ana per la seva alegria contagiosa, a Manu per les seves bromes i selfies, a Alicia pel seu encant especial, a Judit per ser una super companya dins i fora del laboratori, a Carme per cuidar-nos i animar-nos sempre, a Bernat per transmetre'ns la seva força per seguir endavant, a Sara per ser sempre comprensiva amb nosaltres, a Elena per les seves xarrades i consells, a Nico per les seues valuoses classes sobre plasmònica, a Xiaotong per haver-me acollit a casa seua durant l'aventura xinesa i a Irene per rebre'ns sempre amb un somriure.

Als meus amics i companys de viatge Raquel, Sofie, Jacinta, Jerick i Leo per haver compartit moments molt bons amb vosaltres i pels que ens queden.

A la meua família i en especial a la meua cosina Amanda per escoltar-me i recolzar-me en tot moment.

Als meus avis, Pepito i Maruja, pel seu suport durant aquests anys.

Sens dubte, als meus pares, per haver-me anima't a continuar aprenent i a superar-me cada dia. Encara recorde, mare, els dies que repassàvem les taules de multiplicar abans d'anar a l'escola o les teves classes magistrals de matemàtiques, pare. Gràcies per ensenyar-me que amb esforç, tot és possible.

Al meu germà Nèstor, per ser una de les personetes més especials de la meua vida i que m'ha acompanyat durant tants anys. Sé que encara que els

nostres camins s'hagen separat, els tornarem a unir molt prompte (o més et val gilí, si no t'enviaré al mono per a que et torne a robar el paquet de pelotazos).

A Isabel, perquè no tots els germans són de naixement i per il·luminar cadascun dels meus dies. Com ja saps, *you complete me*.

Finalment i amb molta estima, a Llorenç, per haver estat incondicionalment al meu costat i per animar-me cada dia. Ara comença una nova etapa i espere compartir-la amb tu.

UNIVERSITAT ROVIRA I VIRGILI
OPTICAL DETECTION AND STRUCTURAL ANALYSIS OF DNA VIA DIRECT SURFACE-ENHANCED RAMAN SCATTERING
Patricia Gisbert Quilis

UNIVERSITAT ROVIRA I VIRGILI
OPTICAL DETECTION AND STRUCTURAL ANALYSIS OF DNA VIA DIRECT SURFACE-ENHANCED RAMAN SCATTERING
Patricia Gisbert Quilis